2009

IMMERSED BOUNDARY CONDITIONS METHOD FOR COMPUTATIONAL FLUID DYNAMICS PROBLEMS

Syed Zahid Husain

IMMERSED BOUNDARY CONDITIONS METHOD FOR COMPUTATIONAL FLUID DYNAMICS PROBLEMS

(Spine title: IBC METHOD FOR FLOW PROBLEMS)

(Thesis format: Integrated-Article)

by

SYED ZAHID HUSAIN

Graduate Program
in
Engineering Science
Department of Mechanical and Materials Engineering

A thesis submitted in partial fulfillment
of the requirements for the degree of
Doctor of Philosophy

The School of Graduate and Postdoctoral Studies
The University of Western Ontario
London, Ontario, Canada

ABSTRACT

This dissertation presents implicit spectrally-accurate algorithms based on the concept of immersed boundary conditions (IBC) for solving a range of computational fluid dynamics (CFD) problems where the physical domains involve boundary irregularities. Both fixed and moving irregularities are considered with particular emphasis placed on the two-dimensional moving boundary problems. The physical model problems considered are comprised of the Laplace operator, the biharmonic operator and the Navier-Stokes equations, and thus cover the most commonly encountered types of operators in CFD analyses. The IBC algorithm uses a fixed and regular computational domain with flow domain immersed inside the computational domain. Boundary conditions along the edges of the time-dependent flow domain enter the algorithm in the form of internal constraints. Spectral spatial discretization for two-dimensional problems is based on Fourier expansions in the stream-wise direction and Chebyshev expansions in the normal-to-the-wall direction. Up to fourth-order implicit temporal discretization methods have been implemented. The IBC algorithm is shown to deliver the theoretically predicted accuracy in both time and space.

Construction of the boundary constraints in the IBC algorithm provides degrees of freedom in excess of that required to formulate a closed system of algebraic equations. The 'classical IBC formulation' works by retaining number boundary constraints that are just sufficient to form a closed system of equations. The use of additional boundary constraints leads to the 'over-determined formulation' of the IBC algorithm. Over-determined systems are explored in order to improve the accuracy of the IBC method and to expand its applicability to more extreme geometries. Standard direct over-determined solvers based on evaluation of pseudo-inverses of the complete coefficient matrices have been tested on three model problems, namely, the Laplace equation, the biharmonic equation and the Navier-Stokes equations. In all cases tested the over-determined formulations based on standard solvers were found to improve the accuracy and the range of applicability of the IBC method.

Efficient linear solvers suitable for the spectral implementation of the IBC method have been developed and tested in the context of two-dimensional steady and unsteady Stokes flow in the presence of fixed boundary irregularities. These solvers can work with the classical as well as the over-determined formulations of the method. Significant acceleration of the computations as well as significant reduction of the memory requirements have been accomplished by taking advantage of the structure of the coefficient matrix resulting from the implementation of the IBC algorithm. Performances of the new solvers have been compared with the standard direct solvers and are shown to be of up to two orders of magnitude better. It has been determined that the new methods are by at least an order of magnitude faster than the iterative methods while removing restrictions based on the convergence criteria and thus expanding the severity of the geometries that can be dealt with using the IBC algorithm. The performance of the IBC method combined with the new solvers has been compared with the performance of a method based on the generation of the boundary conforming grids, and is found to be better by at least two orders of magnitude. Application of the new solvers to the unsteady problems also results in performance improvement of up to two orders of magnitude. The specialized solvers applied to the over-determined formulation is shown to be at least two orders of magnitude faster than their standard counterparts while capable of extending the range of applicability of the IBC algorithm by 50%-70% for the Stokes flow problem. The concept of the specialized solvers has been extended to solve two-dimensional moving boundary problems described by the Navier-Stokes equations, where the new solver has been shown to result in a significant acceleration of computations as well as substantial reduction in memory requirements.

The conceptual aspects of extending the IBC algorithm for solving three-dimensional problems have been presented using the vorticity-velocity formulation of the three-dimensional Navier-Stokes equations. Test results on the implementation of the IBC algorithm for three-dimensional problems are discussed in the context of heat diffusion problems in the presence of fixed as well as moving boundaries. The algorithm is shown to be spectrally-accurate in space and capable of delivering theoretically predicted accuracy in time for the different test problems. Given a potentially large size of the resultant linear algebraic system, various methods that take advantage of the special structure of the coefficient matrix have been explored in search for an efficient solver, including two versions of the specialized direct solver as well as serial and parallel iterative solvers. Both versions of the specialized direct solver have been shown to be more computationally efficient than the other solution methods.

Possible applications of the IBC algorithm for analyzing physical problems have also been presented. The advantage of using IBC algorithm is illustrated by considering its application to two physical problems, which are – i) analysis of the effects of distributed roughness on friction factor and ii) analysis of traveling wave instability in wavy channels. These examples clearly show the attractiveness of the IBC algorithm for studying effects of a large array of boundary geometries on the flow field.

Keywords: Computational fluid dynamics (CFD), spectral method, immersed boundary conditions (IBC) method, distributed roughness, moving boundary problem, implicit method, Fourier expansion, Chebyshev polynomial, domain transformation (DT) method, direct numerical simulation (DNS).

CO-AUTHORSHIP

The following dissertation is presented in the integrated-article format. Chapters 2 through 6 are based on manuscripts that have been previously published, or submitted, or finalized for submission. I, Syed Zahid Husain, am the first author of all these manuscripts with Prof. J. M. Floryan as a co-author. The manuscript that forms the basis of Chapter 4 has Dr. J. Szumbarski as an additional co-author.

The formulations of the algorithms, computer programming and computations of results presented in Chapters 2 to 6 were performed by me. Mr. D.C. Del Rey Fernandez is responsible for the formulations of the algorithm, computer programming and computations of results associated with the discussions presented in Section 7.2.2 I have assisted Prof. J. M. Floryan in supervising Mr. Fernandez at the different stages of his Masters research including formulation and implementation of the algorithm along with presentation and discussion on the various aspects of the obtained results. I have also been a major contributor in writing the report, which forms the basis of Section 7.2.2.

ACKNOWLEDGEMENT

I would like to start by expressing my sincere gratitude to my supervisor Prof. J. M. Floryan for the tremendous support and advice I have received from him throughout the tenure of my doctoral research. I will remain indebted to Prof. Floryan for his precious time, patience and encouragement. The completion of this dissertation would not have been possible without his incomparable assistance and invaluable guidance.

I would like to thank the members of my advisory committee, Prof. A. G. Straatman and Prof. C. Zhang, for their valuable suggestions and encouragement.

I would also like to thank all of my colleagues (past and present), Dr. Stefan Krol, Dr. Yan Jiang, Dr. J. Szumbarski, Mathew Fotia, Mohammad Zakir Hossain, Aidin Keikhaee, David César Del Rey Fernandez, German Kalugin, Alireza Mohammadi, Mohammad Fazel Bakhsheshi and Hadi Vafadar Moradi for their friendship, cooperation and helping attitude. I am particularly grateful to Dr. J. Szumbarski, Mohammad Zakir Hossain, Alireza Mohammadi, Aidin Keikhaee and David Fernandez for the insightful scientific discussions I had with them that have been tremendously helpful for me in achieving my research objectives.

Words are not enough to express my gratitude towards my family. Without the unconditional love, sacrifice and support of my wife, Zinat Farah Naz, I would not have been able to accomplish my goals. The encouragements from my parents have always kept me together especially during the difficult times.

The research works presented in this dissertation were financially supported by NSERC of Canada and SHARCNET.

TABLE OF CONTENTS

CHAPTER 1

CHAPTER 2

CHAPTER 3

CHAPTER 4

CHAPTER 5

CHAPTER 6

CHAPTER 7

LIST OF TABLES

LIST OF FIGURES

LIST OF APPENDICES

NOMENCLATURE

COMMON NOMENCLATURE FOR ALL CHAPTERS

α : Wave number of geometric irregularities in the x-direction

ω : Frequency of the elastic standing wave

ξ : The horizontal coordinate in the transformed computational domain for the domain transformation (DT) method

η : The vertical coordinate in the transformed computational domain for the DT method

Γ : Constant of coordinate transformation for the IBC method

θ : Temperature

Ψ : Stream function

Ψ_1 : Modification of stream function in the presence of boundary irregularities

Δt : Size of time-step used in different temporal discretization schemes

A_L, A_U : Coefficients of Fourier expansion describing the lower and upper walls in the computational domain for the IBC method

c : Phase speed of the elastic traveling wave

$(d_L)_k$, $(d_U)_k$: Coefficients of Fourier expansion of the first derivative of Chebyshev polynomial of order k along the lower and upper walls

H_L, H_U : Coefficients of Fourier expansion describing the lower and upper walls in the physical domain

M_M : Number of Fourier modes retained in the discretized boundary constraints for the over-determined formulations of the IBC algorithm

N_M : Number of Fourier modes used to discretize dependent variable in the field equation for the different model problems in the x-direction

N_T : Order of Chebyshev polynomial used to discretize the modal functions in the y-direction

N_A : Number of Fourier modes used to define the boundary irregularities

Q : Volume flux

S : Amplitude of wall corrugations

T_k : Chebyshev polynomial of order k

u_1, v_1, p_1 : Velocity and pressure modifications in the presence of boundary irregularities

u_0, v_0, p_0 : Velocity and pressure components associated with the reference plane Poiseuille flow

$\mathbf{V}$: Total velocity vector

u, v, p : Total velocity and pressure components

$(w_L)_k$, $(w_U)_k$: Coefficients of Fourier expansion of Chebyshev polynomial of order k along the lower and upper walls

x : The horizontal coordinate in the physical domain in the fixed frame of reference

X : The horizontal coordinate in the moving frame of reference

y : The wall-normal coordinate in the physical domain

$\hat{y}$: The wall-normal coordinate in the transformed computational domain for the IBC method

y_L, y_U : Shape of the lower and upper walls in the physical domain

$\hat{y}_L$, $\hat{y}_U$: Shape of the lower and upper walls in the computational domain for the IBC method

Y_L : Upper extremity of the upper wall above y=+1 in the physical domain

Y_U : Lower extremity of the lower wall below y=-1 in the physical domain

NOMENCLATURE SPECIFIC TO CHAPTER 2

$\|\theta_U(X)\|_\infty$: L_∞ norm of error in the enforcement of boundary conditions for the steady problem solved in the moving frame of reference (X,y)

$\|\theta_U(x,t)\|_\infty$: L_∞ norm of error in the enforcement of boundary conditions for the unsteady problems solved in the fixed frame of reference (x,y)

NOMENCLATURE SPECIFIC TO CHAPTER 3

$\|u_{er}(X)\|_{\infty}$, $\|v_{er}(X)\|_{\infty}$: L_{∞} norms of error in the enforcement of u- and v-velocity boundary conditions for the steady problem solved in the moving frame of reference (X,y)

$\|u_{er}(x,t)\|_{\infty}$, $\|v_{er}(x,t)\|_{\infty}$: L_{∞} norms of error in the enforcement of u and v-velocity boundary conditions for the unsteady problems solved in the fixed frame of reference (x,y)

NOMENCLATURE SPECIFIC TO CHAPTER 4

$\|\theta_{er}\|_{\infty}$: L_{∞} norm of error in θ over the complete solution domain as compared against a machine accurate reference solution evaluated using the domain transformation (DT) method

$\|\theta_{er,bc}\|_{\infty}$: L_{∞} norm of error in the enforcement of boundary conditions for θ

$\|u_{er}\|_{\infty}$, $\|v_{er}\|_{\infty}$: L_{∞} norms of error in u- and v-velocities over the complete solution domain as compared against machine accurate reference solution evaluated using the DT method

$\|u_{er,bc}\|_{\infty}$, $\|v_{er,BC}\|_{\infty}$: L_{∞} norms of error in the boundary conditions for the u- and v-velocities

w_t : Weight factor

h : Rank of the over-determined coefficient matrix

NOMENCLATURE SPECIFIC TO CHAPTER 5

$\|u_{er}\|_{\infty}$, $\|v_{er}\|_{\infty}$: L_{∞} norms of error in u- and v-velocities over the complete solution domain as compared against machine accurate reference solution evaluated using the DT method

$\|u_{er,BC}\|_{\infty}$, $\|v_{er,BC}\|_{\infty}$: L_{∞} norms of error in the boundary conditions for the u- and v-velocities

NOMENCLATURE SPECIFIC TO CHAPTER 6

$\left\Vert u_{er}(X)\right\Vert_{\infty}$, $\left\Vert v_{er}(X)\right\Vert_{\infty}$	:	L_{∞} norms of error in u- and v-velocities over the complete solution domain for the steady problems solved in the moving frame of reference as compared against machine accurate reference solution evaluated using the DT method
$\left\Vert u_{er,BC}(X)\right\Vert_{\infty}$, $\left\Vert v_{er,BC}(X)\right\Vert_{\infty}$	:	L_{∞} norms of error in the boundary conditions for the u- and v-velocities for the steady problems solved in the moving frame of reference
$\left\Vert u_{er,BC}(x,t)\right\Vert_{\infty}$, $\left\Vert v_{er,BC}(x,t)\right\Vert_{\infty}$	:	L_{∞} norms of error in the boundary conditions for the u- and v-velocities for the unsteady problems solved in the fixed frame of reference

NOMENCLATURE SPECIFIC TO CHAPTER 7

δ	:	Stream-wise wave number of the disturbance field
μ	:	Span-wise wave number of the disturbance field
$\mathbf{\Omega}$	:	The total vorticity vector
$\mathbf{\Omega}_2$	:	The vorticity vector corresponding to the basic state
$\mathbf{\Omega}_3$	:	The disturbance vorticity vector
σ	:	Complex eigen value in the linear stability equations (7.3.2.11)
σ_i	:	Amplification rate of disturbance
σ_r	:	Frequency of disturbance
f	:	Friction factor
N_D	:	Number of Fourier modes used to define the amplitudes of the disturbance velocity field
u_2, v_2, p_2	:	Velocity and pressure components associated with the basic state
u_3, v_3	:	Disturbance velocity components

ABBREVIATIONS

CFD	:	Computational fluid dynamics

IBC	:	Immersed boundary conditions
DT	:	Domain transformation
DNS	:	Direct numerical simulation
SVD	:	Singular value decomposition

CHAPTER 1

Introduction

1.1. Objective

The dissertation develops efficient, spectrally-accurate, temporally implicit gridless algorithms that can be applied to various heat and fluid flow problems involving either fixed or moving boundary irregularities.

1.2. Motivations

Boundary irregularities are encountered in many practical engineering problems pertinent to flow of heat and fluids and are well known to affect the flow field. In general, boundary irregularities can be classified into two different categories, namely, fixed and moving. A regular two-dimensional physical domain that is devoid of any boundary irregularity assumes the shape of a rectangle when investigated in a Cartesian frame of reference while in a polar frame of reference the regular physical domain takes the form of a circle. Therefore, for three-dimensional problems the shape of the regular physical domain in the Cartesian coordinates would resemble a rectangular box with flat surfaces on all sides and in the three-dimensional cylindrical coordinates would resemble a plain cylinder. Flow problems involving physical domains with stationary irregularities are termed as the 'fixed boundary problems'. On the other hand, flow problems where the form of the boundary irregularities vary as a function of time with respect to the laboratory frame of reference in a known and well prescribed manner, are referred to as the 'moving boundary problems'. Unlike the 'free boundary problems', where the boundaries of the flow domain change shape in response to the evolution of flow, the moving boundary problems allow accurate identification of spatial and temporal locations of the flow boundaries *a priori.*

We are particularly interested in investigating boundary irregularities that have the form of roughness, where the mean heights of the irregularities are very small compared to the characteristic length of the flow domain. The individual roughness elements can have different shapes and may be apart from each other by large enough distance forming isolated roughness elements. Irregularities can also be spread all along the walls of physical domain of interest, which are termed as distributed roughness. Corrugated boundaries, therefore, also belong to the class of distributed roughness. From a physical perspective, our research is focused on the analysis of the effects of distributed roughness.

Among various effects, it is well known that surface roughness exerts crucial influence on heat transfer rate [1], skin friction drag [1, 2] and transition of shear layers from laminar to turbulent states [3, 4]. One of the principal motivations for the research work has been the interest to examine the influence that fixed surface roughness can exert on the hydrodynamic stability of shear layers in channel flows. Such studies allow devising passive flow control strategies in order to accelerate or decelerate the laminar-turbulent transition process through the design of properly structured roughness [5]. In this regard, one first needs to compute the modified mean flow in the presence of stationary roughness by solving the steady Navier-Stokes equations where high spatial accuracy is warranted. The next step is to forecast the behavior of the mean flow when it is subjected to small perturbations using linear stability analysis, which predicts the growth rate of the disturbances. In addition to high accuracy, the computational efficiency of the mean flow solver is a substantial issue as a comprehensive hydrodynamic stability analysis requires investigation of a vast array of geometric shapes. Algorithms that permit simple and convenient modeling of the boundary geometries are tremendously advantageous in such scenarios and, therefore, developing an efficient algorithm has been an important objective for the present research. Finally, in order to study the evolution of instabilities towards the final saturation state a tool needs to be developed to perform direct numerical simulation (DNS) where once again the importance of the efficiency of the DNS solver becomes as crucial as the accuracy it can deliver [6].

Flow problems with moving surface roughness also possess significant importance from physical perspective especially in designing active flow control strategies [5]. Highly accurate and efficient algorithms that are capable of solving such flows can be used as a means to design active flow control systems where the shape of the roughness is adjusted dynamically in response to flow evolution. Besides this, researchers from various other fields have been attracted to efficient algorithms for moving boundary problems. One of the major motivations for the present research has been to develop an algorithm capable of analyzing peristaltic and pulsatile flows that are encountered in the field of biomedical engineering when one is interested in studying flows through the esophagus and vasculatures, respectively. Any algorithm intended to examine such flows require the capabilities of handling flow involving deforming boundaries with high accuracy and also in an efficient manner. This explains our motivation for developing an algorithm that can efficiently handle moving boundary problems and deliver high spatial and temporal accuracy.

1.3. Fixed boundary problems

We shall first focus on flow problems involving boundary irregularities that remain stationary with respect to the laboratory frame of reference. In general, the numerical solution process works by approximating the governing partial differential equations describing the physical flow with a set of algebraic equations through discretization and the presence of boundary irregularities imposes a major challenge for any algorithm employed for discretization. Over the years, researchers have developed numerous algorithms to deal with such challenges. When the system of discretized equations is represented in the matrix form, the corresponding matrix of the coefficients of the unknowns is referred to as the coefficient matrix. In most algorithms, the algebraic equations are derived by discretizing the field equations into a number of finite points or elements or elemental volumes, thereby making the resultant discretization grid-dependent. Methods based on finite-elements, finite-difference and finite-volumes are examples of grid-dependent discretization procedures. On the other hand, there are gridless methods where the discretization is not performed on any particular grid points or elements and generally work by assuming global solutions based on expansion of polynomials. For example, Galerkin-projection-based spectral method discretizes field equations in a gridless manner.

1.3.1. Review of the available algorithms for fixed boundary problems

Most of the conventional algorithms for solving flow problems involving fixed irregularities are based on the generation of boundary conforming grids that uses standard finite-element, finite-volume or finite-difference schemes [1, 7]. Here one of the grid lines coincides with each of the boundaries of the physical domain. These standard methods suffer from a common limitation of lower spatial accuracy mainly attributable to low-order of discretization schemes that are typically used for these methods. Higher absolute accuracy can nevertheless be achieved using very fine grids but results in unreasonable computational overhead while the use of higher-order schemes generally necessitate substantial increase in efforts associated with formulations, grid construction and programming implementations [8]. Moreover, computational efficiencies of all these methods drop sharply when assigned to investigate a large array of boundary geometries particularly due to substantial cost of generating the coefficient matrices for the different boundary shapes.

Some other methods are based either on numerical or analytical mapping of the physical domain. Domain transformation (DT) method relies on analytical mapping of the irregular physical domain into a regular computational domain allowing exact enforcement of flow boundary conditions. DT method coupled with spectral discretization of the transformed spatial coordinates is capable of delivering high spatial accuracy [9, 10, 11]. However, analytical mapping contributes to substantial complication in the transformed field equations resulting in significant cost for generating the coefficient matrix. Therefore, spectral implementation of the DT method is recommendable for solving flow problems with high degree of irregularities only [10, 11].

Domain perturbation (DP) method offers an alternative simple approach for handling boundary irregularities. This method uses a regular computational domain and instead of enforcing the boundary conditions along the edges of the physical domain the method works by transferring the boundary conditions to a certain mean location [10, 11, 12]. However, the applicability of DP method is limited to problems with very small amplitudes of roughness [11]. For flow over a rough leading edge it has been found that the first-order DP method provides reasonable accuracy only for situations where flow modifications induced by the boundary irregularities can be approximated by a linear theory [13].

A novel approach for solving flow problems involving boundary irregularities was proposed by Peskin in 1982 [14]. The method was based on the concept of immersed boundaries. The idea was implemented for studying flow behavior around cardiac valves and is generally referred to as the 'immersed boundary (IB) method'. Similar to the DT and DP methods, the IB method also uses regular computational domain, however, the edges of the computational domain extends beyond the edges of the physical domain. Therefore, the computational and physical boundaries may not necessarily coincide. Unlike the DP method, the physical boundary conditions in the IB method are enforced along the edges of the physical domain that are immersed inside the extended computational domain. Since the first work of Peskin, a number of variants of the immersed boundary methods have been developed by various researchers and are reviewed in [15, 16]. The original IB method as proposed by Peskin in the context of cardiac mechanics problems has later turned into a popular tool for handling problems involving fluid-structure interactions [16]. The physical boundary conditions on the immersed boundaries are imposed using additional forcing and the nature of this forcing is the fundamental distinguishing feature of the different variants of the IB method [15].

The forcing, in general, may be either continuous or discrete [15]. In the continuous forcing approach, the continuous governing equation is first modified by using a source term or forcing function in order to account for the no-penetration and no-slip conditions at the boundaries. The modified governing equation is subsequently discretized on a Cartesian grid which implies that the general formulation involved is independent of discretization technique [15]. In the case of the discrete forcing approach, the governing equation is first discretized and then only the cells adjacent to the immersed boundaries are adjusted to account for the physical boundary conditions. The discretization method, therefore, plays an important role for the discrete forcing approach [15]. The elimination of the cost of generating body conforming grids make the IB methods computationally very efficient as compared to the methods that rely on constructing body conforming grids discussed earlier. However, most of the IB methods are based on the low-order finite-difference, finite-volume or finite-element techniques [15] and as a result suffer from a common issue of low spatial accuracy. Moreover, the very physical concept of local forcing along the immersed boundaries used to enforce the no-slip and no-penetration conditions adds another level of uncertainty in these algorithms. The forcing are capable of affecting the flow physics locally around the boundaries, which although is difficult to quantify may lead to inaccurate representation of local wall shear as well as other derivatives of the flow quantities. Any procedure that even locally changes the flow physics may be unable to predict the second derivative of mean flow with sufficient accuracy. This can lead to significant inaccuracy in the study of stability of shear layers which are strongly affected by the second derivative of the mean flow. Aiming for higher spatial accuracy may lead to even further deterioration of this problem. This particular aspect of uncertainty associated with the IB methods have not been studied thoroughly and requires systematic investigation.

1.3.2. The immersed boundary conditions (IBC) method

One of the common limitations for most of the methods discussed so far is low spatial accuracy resulting from various low-order discretization techniques, which these methods are mostly based upon. Spectral methods are well known to provide the highest accuracy for spatial discretization of the field equations and, therefore, have become the preferred approach particularly for direct numerical simulations [7]. However, most of the standard implementations of the spectral method are restricted to regular geometries, i.e., physical domains involving straight walls. Szumbarski and Floryan [17] developed a novel algorithm for solving two-dimensional steady-state fixed boundary problems that combined the inherent efficiency of the immersed boundary concept with the high accuracy of spectral discretization. This method is referred to as the immersed boundary conditions (IBC) method in the present work. The discretization of the field equation in the stream-wise direction where the flow is assumed to be periodic is implemented using Fourier expansions, which reduces the governing partial differential equation into a set of ordinary differential equations. Discretization in the normal-to-the-wall direction is performed using expansions based on Chebyshev polynomials. Finally, a set of algebraic equations in terms of the unknown coefficients of the Chebyshev polynomials are derived using the method of Galerkin projection [18]. Boundary geometries in the IBC algorithm are assumed to be periodic and are modeled using Fourier expansions. Although it limits the applicability of the algorithm only to boundary shapes that are expressible using Fourier expansions the resultant discretization process is gridless as all possible variations of boundary geometries can be achieved by changing the Fourier coefficients only. Such modeling of the geometries also substantially simplifies programming numerous geometries, which are essentially defined by a set of Fourier coefficients only. Unlike the IB methods discussed in the previous section, the IBC method does not depend on any fictitious forcing to impose the physical boundary conditions, rather transforms the original boundary value problem into an internal value problem. The discretized boundary conditions, therefore, enter the algorithm in the form of internal constraints. However, construction of the boundary constraints in the IBC method provides degrees of freedom in excess of that required to formulate a closed system of algebraic equations. The standard implementation of the IBC method as presented in [17], accommodates the boundary constraints in a Tau like manner [18] resulting in a closed system of equations and is referred to as the 'classical IBC formulation'. The first unsteady implementation of the IBC algorithm was done by

Husain and Floryan [9] in the context of a simpler two-dimensional conductive heat flow problem involving fixed boundaries. The superiority in computational efficiency of the IBC method over the spectral implementation of the DT method is evident from the results presented in [9].

1.4. Moving boundary problems

1.4.1. Review of the available algorithms for moving boundary problems

Researchers have developed a variety of algorithms over the years in order to deal with the moving boundary problems. The different algorithms as a whole can be classified into two categories, Lagrangian and Eulerian [19, 20]. Combinations of Lagrangian and Eulerian schemes, termed as the mixed methods [19], have also been investigated.

Lagrangian methods are well suited for moving boundary problems [19, 20]. The coordinate systems in these methods move along with the fluid, which implies that the individual computational cells always contain the same fluid elements. The so called Lagrangian velocities are functions of time and initial positions of all elements of the fluid body. Lagrangian methods permit sharp identification and simple delineation of the moving boundaries thereby allowing precise enforcement of the boundary conditions. However, Lagrangian methods are not suitable for problems where there is a possibility of significant mesh distortion [19, 20]. For such problems the Lagrangian algorithms suffer from problems of mesh tangling and numerical instabilities related to highly distorted meshes that consequently results in loss of numerical accuracy [19, 20]. Possible remedial measures to deal with mesh distortion and associated problems are reviewed in [19, 20].

An Eulerian algorithm, in general, works with coordinate system that is stationary in a laboratory frame of reference. However, in certain cases the coordinate system for an Eulerian scheme may move in a prescribed manner in order to account for the continuously changing solution domain [19, 20]. Eulerian algorithms can be divided for convenience into three sub-categories, namely, fixed grid, adaptive grid and various mapping methods [19].

In the fixed grid methods, the grid is fixed in the solution domain and the location of the moving boundaries can be tracked using either surface [21] or volume tracking procedures [22]. The algorithms based on surface tracking track the moving boundaries using a series of interpolated curves through a discrete set of points whose motions during the solution process allow precise identification of the boundary locations [22, 23]. The high memory requirements associated with the necessity to store the locations of the points and other relevant information is a major drawback for the surface tracking methods particularly for problems with highly deforming boundaries [20]. The volume tracking algorithms on the other hand work by reconstructing the boundaries using marker quantities whenever necessary and, therefore, do not require storage of the boundary locations. The presence of a convenient marker within a computational cell and its quantity forms the basis of the various boundary reconstruction methodologies. Different versions of volume tracking algorithms exist, e.g., volume of fluid (VOF) [24], marker and cell (MAC) [25] and level set [26, 27] methods. These methods are based on standard spatial discretization schemes with low order of accuracy for the field equations, which are consistent with the diffused locations resulting from the boundary reconstruction processes.

The adaptive grid Eulerian methods for moving boundary problems rely on numerical mappings to adjust the grids at each time step so that two of the grid lines always overlap with the moving boundaries. Very high computational costs attributable to grid reconstruction at each time step act as a major predicament for these methods. For example, around 75% of the total computational cost for the problem discussed in [28] is attributable to the grid construction process alone. The computational costs for these methods are not affected significantly by the choice of spatial discretization techniques. The requirement of high accuracy in solution may lead to numerous challenges as the overall error is contributed by the error in grid generation as well as error from spatial and temporal discretizations of the field equations. Analytical mapping of the irregular physical domain into a rectangular computational domain in the case of DT method can help in improving the accuracy at the cost of increased complexity of the field equations [9, 29]. However, such mappings are available only for a limited class of geometries [19] and reconstruction of the coefficient matrix during each time step can add to the overall computational cost by a substantial margin [9].

On the basis of the discussions on the various algorithms in the present section, it is evident that optimizing the requirements of high accuracy and computational efficiency constitutes the greatest challenge for any algorithm employed for solving moving boundary problems. Immersed boundary (IB) methods, as discussed in Section 1.3.1, are inherently better suited to deal with the variability of geometries of the solution domain. In fact, the concept as first proposed by Peskin [14] was applied to blood flow around the valves of a beating heart. Although the basic underlying concept of the IB methods make them efficient in dealing with moving boundaries, most of the IB methods for the moving boundary problems suffer from similar limitations as has been discussed for the fixed boundary problems, i.e., low spatial accuracy and uncertainties associated with the use of additional forcing to satisfy the boundary conditions.

1.4.2. IBC algorithm as applied to the moving boundary problems

The accuracy of any algorithm applied for solving moving boundary problems is influenced by two dominating factors – i) the precision in representation of the temporal and spatial locations of the boundaries and ii) the error associated with the scheme employed to discretize the field equation. The IBC method relies on spectral discretization of the spatial coordinates of the field equation and allows sharp identification of the locations of time-dependent physical boundaries. The algorithm is conceptually similar to the fixed grid Eulerian methods. As the algorithm works with an extended computational domain, therefore, the physical domain at any instance of time is immersed inside the computational domain. The field equations are required to be discretized only once for the complete simulation and during every time step only the boundary conditions are discretized using the IBC concept to account for the change in boundary locations. This reduces the cost of generating the coefficient matrix significantly as only the part of the matrix corresponding to the boundary conditions are required to be reconstructed at every time step. Special solution methodologies can be developed that take advantage of this characteristic of the IBC algorithm in order to reduce the effective size of the system of equations required to be solved at each time step by a substantial margin without comprising the spectral accuracy in the spatial dimensions.

1.5. Preview of the dissertation

The materials presented in this dissertation are organized in seven chapters. This section is intended to provide a preview of the material presented in the different chapters. Chapters 2 to 4 are derived from manuscripts that have already been published or accepted for publication in various scientific journals. Chapters 5 and 6 are based on manuscripts that have been submitted to scientific journals for publication and are currently under review. The structure of the dissertation follows the integrated-article format and therefore, Chapters 2 to 6 retain the contents of the relevant manuscripts in their entirety without the associated abstracts.

Chapter 1 provides information regarding the objectives of the present research along with the motivating factors. It also briefly discusses the various algorithms available for handling fixed and moving boundary problems along with their respective limitations with the aid of the existing literature. The chapter also introduces the concept of immersed boundary conditions in conjunction with a concise discussion on the basic traits and prospective advantages and limitations of the algorithm in the context of both fixed and moving boundary problems.

Chapter 2 presents the application of the IBC algorithm for moving boundary problems in the context of two-dimensional conductive heat flow. The physical mechanism of diffusion is governed by a linear second order partial differential equation described by the Laplace operator. The model problem, therefore, permits convenient characterization of the fundamental disposition of the IBC algorithm when employed for moving boundary problems. Comparisons of different versions of iterative solvers that take advantage of the unusual structure of coefficient matrix resulting from the implementation of the IBC method are also presented. The computational cost advantage of the IBC method as compared with the spectral implementation of the DT method is demonstrated as well with the aid of [9].

Chapter 3 deals with the extension of the IBC algorithm to two-dimensional Stokes flow involving moving boundaries. Stokes flow when formulated in terms of the stream function is described by the biharmonic operator, which is a fourth-order linear partial differential equation. One of our principal objectives is to employ the IBC algorithm for solving moving boundary problems described by the three-dimensional Navier-Stokes equations. When such a problem is posed in terms of the velocity-vorticity formulation (with elimination of the pressure), the Laplace and the biharmonic operators become the main constituents. Therefore, the Stokes flow problem chosen in Chapter 3 is the natural step in the investigation of the extension of the IBC algorithm from the heat conduction problem towards the full Navier-Stokes problem. Moreover, from a physical perspective most flows in micro-channels fall under the purview of the Stokes limitation and for that matter spectrally-accurate algorithm for handling Stokes flow is going to be very useful tool as well. Effectiveness of various iterative solution strategies that take advantage of the special structure of the coefficient matrix resulting from the implementation of the IBC algorithm are also explored in this chapter.

In Chapter 4, an over-determined formulation of the IBC algorithm (as opposed to the ‘classical formulation’ referred to earlier) is proposed by using additional boundary constraints that result from the discretization of the physical boundary conditions with the use of the IBC algorithm. Use of the additional constraints that leads to over-determined systems are explored in this chapter in order to improve the accuracy of the IBC method and to expand the applicability of the method to more extreme geometries. Possible improvement of accuracy through the use of the over-determined formulation could be problem dependent. Therefore, the formulation has been tested on three model problems, i.e., the Laplace equation, the biharmonic equation and the Navier-Stokes equations; and thus the chapter covers the most commonly encountered types of operators in computational fluid dynamics problems.

Specialized linear solvers suitable for the spectral implementation of the Immersed Boundary Conditions (IBC) method are developed and tested in Chapter 5. For convenience, Stokes flow is considered as the model problem. The efficient specialized solvers have been implemented for both the classical and the over-determined IBC formulations. Performances of the new solvers have been compared with the standard direct solvers and different iterative solvers. The performance of the specialized IBC solvers has also been compared against spectrally-accurate domain transformation (DT) method, which is based on the generation of the boundary conforming grids. Application of the new solvers to the unsteady fixed boundary problems has also been investigated. The purpose of developing the new solvers has been to make three-dimensional calculations using the IBC method practically feasible by reducing the computing costs for the irregular geometries (e.g., channels bounded by corrugated walls) close to the computing costs for the regular geometries (e.g. channels with straight walls).

Chapter 6 presents the extension of the IBC algorithm as applied to simulations of viscous flows with moving boundaries described by the two-dimensional Navier-Stokes equations. Up to fourth-order implicit temporal discretization methods have been implemented. Performances of various linear solvers employed in the solution process have been evaluated and a new class of solver that has its root in the specialized solvers presented in Chapter 5 is proposed and tested.

Finally, Chapter 7 summarizes the various important observations made with regard to the different formulations (classical and over-determined) of IBC algorithm as well as different solvers (direct and iterative) as applied to the different two-dimensional model problems in a summarized form. Possible extension of the IBC algorithm to three-dimensional problems is later laid out in the context three-dimensional velocity-vorticity formulation of the Navier-Stokes equations. The different issues with regard to the implementation of the IBC algorithm for three-dimensional problems are discussed using the test results based on a simpler physical problem that deals with unsteady heat diffusion in the presence of fixed as well as moving boundaries. The results to be presented in this regard are extracted from the report [30]. My colleague D.C. Del Rey Fernandez is responsible for the formulation, programming implementation and computations of the results presented in [30] as a part of his Masters research. I have assisted Prof. Floryan in supervising him throughout the different stages of formulation and implementation of the algorithm along with presentation and discussion on the various aspects of the computed results presented in [30]. I have also been a principal contributor in the writing of the report [30]. Various solvers that take advantage of the special structure of the coefficient matrix including a version of the specialized direct solvers based on the concept presented in Chapter 5 as well as serial and parallel iterative solvers are explored for the three-dimensional problem in search for an efficient solver. Possible applications of the research work associated with the dissertation are also briefly presented in this chapter using two illustrative examples. Results obtained by the IBC method are verified against those available in literature to validate the reliability of the algorithm. Finally, the conclusions on the various aspects of the research associated with this dissertation are presented in a summarized form along with recommendations for future work.

1.6. References

[1] Croce, G. and D'Agaro, P., Numerical simulation of roughness effect on microchannel heat transfer and pressure drop in laminar flow, *J. Phys. D: Appl. Phys.*, vol. 38, pp. 1518-1530 (2005).

[2] McLean, J.W., Computations of turbulent flow over a moving wavy boundary, *Phys. Fluids*, vol. 26, pp. 2065-2073 (1983).

[3] Floryan, J.M., Three-dimensional instabilities of laminar flow in a rough channel and the concept of hydraulically smooth wall, *Eur. J. Mech. B/Fluids*, vol. 26, pp. 305-329 (2007).

[4] Floryan, J.M., Centrifugal instability of Couette flow over a wavy wall, *Phys. Fluids*, vol. 14, pp. 312-322 (2002).

[5] Gad-el-Hak, M., Pollard, A. and Bonnet, J-P., Flow control: Fundamentals and practices, *Springer-Verlag* (1998).

[6] Moin, P. and Mahesh, K., Direct numerical simulations: a tool in turbulence research, *Ann. Rev. Fluid Meh.*, vol. 30, pp. 539-578 (1998).

[7] Yoon, S., Na, S., Wang, Z.J., Bons, J.P. and Shih, T.I-P., Flow and heat transfer over rough surfaces: usefulness of 2-D roughness-resolved simulations, *44th Aero. Sci. Meet. Exhibit*, Reno, Nevada (2006).

[8] Jiang, Y. and Floryan, J.M., Finite-difference 4th-order compact scheme for the direct numerical simulation of instabilities of shear layers, *Int. J. Numer. Meth. Fluids*, vol. 48, pp. 1259-1281 (2005).

[9] Husain, S.Z. and Floryan, J.M., Immersed boundary conditions method for unsteady flow problems described by the Laplace operator, *Int. J. Num. Meth. Fluids*, vol. 56, pp. 1765-1786 (2007).

[10] Angelis, V.De, Lombardi, P. and Banerjee, S., Direct numerical simulation of turbulent flow over a wavy wall, Phys. Fluids, vol. 9, pp. 2429-2442 (1997).

[11] Cabal, A., Szumbarski, J. and Floryan, J.M., Numerical simulation of flows over corrugated walls, Comp. Fluids, vol. 30, pp. 753-776 (2000).

[12] Tsangaris, S. and Potamitis, D., On laminar small Reynolds-number flow over wavy walls, *Acta Mechanica*, vol. 61, pp. 109-115 (1986).

[13] Floryan, J.M. and Dallmann, U., Flow over a leading edge with distributed roughness, *J. Fluid. Mech.*, vol. 216, pp. 629-656 (1990).

[14] Peskin, C.S., The fluid dynamics of heart valves: experimental, theoretical and computational methods, *Annu. Rev. Fluid Mech.,* vol. 14 pp. 235-59 (1982).

[15] Mittal, R. and Iaccarino, G., Immersed boundary methods, *Annu. Rev. Fluid Mech.,* vol. 37 pp. 239-261 (2005).

[16] Peskin, C.S., The immersed boundary method, *Acta Numerica*, 479-517 (2002).

[17] Szumbarski, J. and Floryan, J.M., A direct spectral method for determination of flows over corrugated boundaries, *J. Comp. Phys.*, vol. 153, pp. 378-402 (1999).

[18] Canuto, C., Hussaini, M.Y., Quarteroni, A., and Zang, T.A., Spectral methods in fluid dynamics, *Springer* (1987).

[19] Floryan, J.M. and Rasmussen, H., Numerical analysis of viscous flows with free surfaces, *Appl. Mech. Rev.*, vol. 42, pp. 323-341 (1989).

[20] Navti, S.E., Lewis, R.W. and Taylor, C., Numerical simulation of viscous free surface flows, *Int. J. Num. Meth. Heat & Fluids Flow*, vol. 8, pp. 445-464 (1997).

[21] Scardovelli, R. and Zaleski, S., Direct numerical simulation of free surface and interfacial flow, *Annu Rev. Fluid Mech.*, vol. 31, pp. 567-603 (1999).

[22] Hyman, J.M., Numerical methods for tracking of interfaces, *Physica,* vol. 12D, pp. 396-407 (1984).

[23] Glimm, J., Grove, J.W., Li, X.L., Shyue, K.M., Zeng, Y. and Zhang, Q., Three-dimensional front tracking, *SIAM J. Sci. Computing,* vol. 19, pp. 703-727 (1998).

[24] Hirt, C.W. and Nichols, B.D., Volume of Fluid (VOF) Method for the Dynamics of Free Boundaries, *J.Comp.Phys.*, vol. 39, pp. 201-225 (1981).

[25] Harlow, F.H. and Welch, J.E., Numerical study of large amplitude free surface motions, *Phys.Fluids*, vol. 9, pp. 842-851 (1966).

[26] Osher, S.J. and Sethian, J.A., Fronts propagating with curvature dependent speed: Algorithms based on Hamilton-Jacobi formulations, *J. Comp .Phys.*, vol. 79, pp. 12-49 (1988).

[27] Sethian, J.A. and Smereka, P., Level set methods for fluid interfaces, Annu. *Rev. Fluid Mech.*, vol. 35, pp. 341-372 (2003).

[28] Inculet, I., Floryan, J.M. and Haywood, R., Dynamics of water droplets break-up in electric fields, *IEEE Transactions on Industry Applications*, vol. 28, pp. 1203-1209 (1992).

[29] Hamed, M. and Floryan, J.M., Numerical simulation of unsteady nonisothermal capillary interfaces, *J.Comp.Phys.* vol. 145, pp. 110-140 (1998).

[30] Fernandez, D.C.D.R., Husain, S.Z. and Floryan, J.M., Immersed boundary conditions method for three-dimensional heat diffusion problems, *Expert Systems in Fluid Dynamics Research Laboratory Report ESFD-1/2009*, Department of Mechanical and Materials Engineering, The University of Western Ontario, London, Ontario, N6A 5B9, Canada (2009).

CHAPTER 2

Moving boundary problems described by the Laplace operator[1]

2.1. Introduction

The term 'moving boundary problem' refers to a problem where a boundary of the solution domain changes location during the solution process. The related problem where boundary motion is *a priori* unknown and has to be predicted as a part of the solution process is usually referred to as a 'free boundary problem'. In the present chapter we are interested in finding a spectrally-accurate solution to the first problem that maintains sharp resolution of the location of the boundary.

Moving-boundary algorithms have been reviewed in [1] and can be classified as Eulerian, Lagrangian and mixed. Eulerian algorithms rely on a coordinate system that is stationary in a laboratory frame of reference or moves in a prescribed manner (Galilean transformation). Such algorithms can be divided for convenience into fixed grid methods, adaptive grid methods and various mapping methods.

In the fixed grid methods the grid is fixed in the domain and, since in general, the location of the moving boundary does not overlap with a grid line, a special procedure must be added to identify the location of the moving boundary. This location can be

[1] A version of this chapter has been published as –

Husain, S.Z., and Floryan, J.M., Implicit Spectrally-Accurate Method for Moving Boundary Problems using Immersed Boundary Conditions Concept, *Journal of Computational Physics*, vol. 227(9), pp. 4459-4477 (2008).

tracked using either surface or volume tracking procedures. In the former approach a set of points is introduced to mark location of the boundary which is represented as a set of interpolated curves. These points are moved in a prescribed manner during the solution process [2,6] and provide ability for precise identification of boundary location. In the latter approach the information about the boundary location is not stored but the boundary is reconstructed whenever necessary on the basis of the presence of certain quantity of a convenient marker within computational cell, e.g., MAC - Marker and Cell [3], VOF -Volume of Fluid [4,12] and Level Set [9,13] methods. The reconstruction process leads to a diffused location of the boundary but the overall accuracy can be made consistent with low accuracy discretization schemes for the field equations.

In the adaptive grid methods the computational grid is continuously adapted so that one of the grid lines always overlaps with the moving boundary. This leads to a large computational overhead associated with grid re-generation at each simulation time step. In this sense numerical grid generation combined with finite-difference discretization of the field equations and grid generation for the finite-element discretization are conceptually identical. In certain situations numerical grid generation can be replaced by analytical mappings, but this does not alter the basic concept of such methods. The overall accuracy of tracking of the location of the boundary is determined by the accuracy of numerical implementation of various mapping schemes.

Lagrangian methods are characterized by a coordinate system that moves with the fluid. Each computational cell always contains the same fluid and its tracking requires solution of an initial value problem. These methods are well suited for moving boundary problems as they permit simple delineation of moving boundaries. The two main problems involve mesh tangling and loss of numerical accuracy associated with highly distorted meshes. Possible remedies are discussed in [1]. Mixed Lagrangian-Eulerian methods rely on the combination of concepts described above [1].

The accuracy of the available methods for solving moving boundary problems is dictated by the accuracy of representation of boundary location and by the discretization error of the field equations. Spectral methods provide the lowest error for the field equations but are limited to solution domains with regular geometries. The variability of geometry of the solution domain represents the main challenge for implementation of these methods. One possible implementation can be based on the concept of immersed boundary conditions [11]. This concept has been proposed in [8,10] in the context of simulation of cardiac dynamics but its first spectrally accurate implementation for fixed boundary problems has been given in [11]. Immersed boundary conditions method uses fixed, regular solution domain for the required spectral expansions and the actual physical domain is submerged in the interior of the computational domain. Boundary conditions at the edges of the physical domain are replaced by constraints imposed inside computational domain. The method is analogous to the fixed grid methods discussed above.

This chapter describes extension of the algorithm proposed in [11] to the case of moving boundary problems. The analysis is carried out in the context of diffusion problem. The model problem is described in Section 2.2. The Immersed Boundary Conditions (IBC) method is discussed in Section 2.3. The Domain Transformation (DT) method that is used to demonstrate the efficiency of the IBC method is discussed in Section 2.4. Results of numerical tests are discussed in Section 2.5. Section 2.6 provides a short summary of the main conclusions.

2.2. Model problem

We shall pose the problem of interest in the context of heat conduction. Consider unsteady conductive heat flow in a slot bounded by corrugated walls whose geometry changes as a function of time and is described by the following relations (see Fig. 2.1)

$$y_L(x,t)=-1+\sum_{n=-\infty}^{\infty}H_L^{(n)}(t)e^{in\alpha x}, \qquad y_U(x,t)=1+\sum_{n=-\infty}^{\infty}H_U^{(n)}(t)e^{in\alpha x} \qquad (2.2.1a,b)$$

where $H_L^{(n)} = H_L^{(-n)*}$, $H_U^{(n)} = H_U^{(-n)*}$ and star denotes complex conjugate. Such problems are of interest in the case of nano-channels and nano-switches where the effects of surface roughness could be significant [7]. The slot is periodic with wavelength $\lambda=2\pi/\alpha$ and extends to ±∞ in the x-direction. The dimensionless field equation describing heat flow has the form

$$\partial^2\theta / \partial x^2 + \partial^2\theta / \partial y^2 = \partial\theta / \partial t. \qquad (2.2.2)$$

where θ denotes temperature. This equation needs to be supplemented by suitable initial and boundary conditions, which are taken to be in the form

$$\theta(x,y,t=0) = \theta, \quad y_L(x,0)=y_{Li}(x), \quad y_U(x,0)=y_{Ui}(x), \qquad (2.2.3a\text{-}c)$$

$$\theta(x, y_L(x,t), t) = \theta_L(x,t), \quad \theta(x, y_U(x,t), t) = \theta_U(x,t) \qquad (2.2.4a,b)$$

where θ_i, y_{Li}, y_{Ui}, θ_L, θ_U are considered to be known.

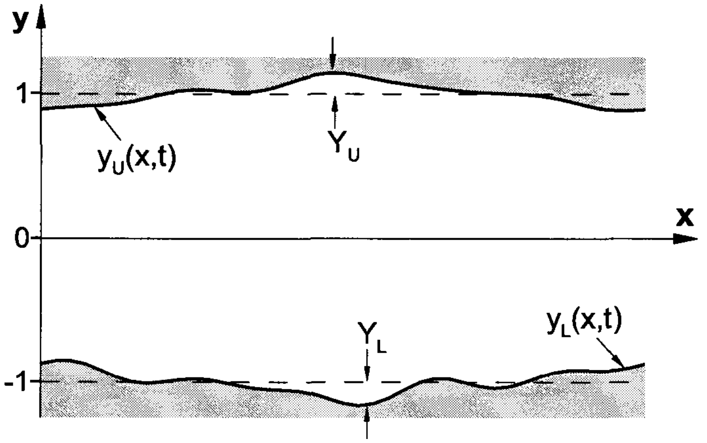

Figure 2.1. *Sketch of the instantaneous form of the domain of interest in the physical plane.*

The time variations of the temperature field result from the variations of the temperature along the edges of the physical domain as well as from the deformation of the domain. The main difficulty in finding a solution to (2.2.2)-(2.2.4) is associated with the variations of the geometry of the physical domain, which leads to the moving boundary problem. We shall discuss two solution methods suitable for this problem, i.e., a method based on the concept of immersed boundary conditions (IBC) and a method based on the concept of domain transformation (DT). The latter method will be used to illustrate advantages of the IBC method. We shall begin our discussion with the former method.

2.3. The immersed boundary conditions (IBC) method

We are interested in the determination of the solution of (2.2.2)-(2.2.4) with spectral accuracy. We shall use Fourier expansions in the x-direction and expansions in terms of Chebyshev polynomials in the y-direction. Standard definition of Chebyshev polynomials uses the domain (-1,1), however the physical domain is confined between ($1+Y_U$) and ($-1-Y_L$) where Y_U and Y_L denote the locations of extremities of the domain of interest during time interval of interest (see Fig. 2.1). The first step in the solution process involves a mapping from the physical (x,y) coordinates to the computational $(x, \hat{y})$ coordinates in the form

$$\hat{y}=2\frac{y-(1+Y_U)}{1+Y_U-(-1-Y_L)}+1 \tag{2.3.1}$$

where $\hat{y}\in\langle -1,1\rangle$. The governing equation takes the form

$$\partial^2\theta/\partial x^2+\Gamma^2\,\partial^2\theta/\partial\hat{y}^2\ =\partial\theta/\partial t \tag{2.3.2}$$

where $\Gamma=2/(2+Y_U+Y_L)$ is a constant. Locations of the corrugated boundaries in the $(x, \hat{y})$ plane are given as

$$\hat{y}_L(x,t)=\sum_{n=\ \infty}^{\infty}A_L^{(n)}(t)e^{in\alpha x}\,, \qquad \hat{y}_U(x,t)=\sum_{n=\ \infty}^{\infty}A_U^{(n)}(t)\,e^{in\alpha x}\,, \tag{2.3.3a,b}$$

where $A_L^{(0)}(t)=1+\Gamma\left[-2-Y_U+H_L^{(0)}(t)\right]$, $A_L^{(n)}(t)=\Gamma H_L^{(n)}(t)$ for $n\neq 0$, $A_U^{(0)}(t)=1+\Gamma\left[-Y_U+H_U^{(0)}(t)\right]$, $A_U^{(n)}(t)=\Gamma H_U^{(n)}(t)$ for $n\neq 0$. The boundary conditions at the transformed boundaries become

$$\theta(x,\hat{y}_L(x,t),t)=\theta_L(x,t), \qquad \theta(x,\hat{y}_U(x,t),t)=\theta_U(x,t). \tag{2.3.4a,b}$$

The solution can be represented in the form of Fourier expansion

$$\theta(x,\hat{y},t)=\sum_{n=-\infty}^{\infty}\Phi^{(n)}(\hat{y},t)e^{in\alpha x}\approx\sum_{n=-N_M}^{N_M}\Phi^{(n)}(\hat{y},t)e^{in\alpha x} \tag{2.3.5}$$

where $\Phi^{(n)}(\hat{y},t)=\Phi^{(-n)*}(\hat{y},t)$ and star denotes complex conjugate. Substitution of (2.3.5) into the field equation and separation of Fourier components lead to an uncoupled system of parabolic partial differential equations for $\Phi^{(n)}$, $n\in\langle 0,N_M\rangle$, of the type

$$\partial\Phi^{(n)}/\partial t=\left(\Gamma^2 D^2-n^2\alpha^2\right)\Phi^{(n)} \tag{2.3.6}$$

where D=d/d$\hat{y}$. Two types of temporal discretizations are used. The two-step implicit method results in the following relations

$$\left[\Gamma^2D^2-\left(n^2\alpha^2+1.5\Delta t^{-1}\right)\right]\Phi_{\tau+1}^{(n)}=-2\Delta t^{-1}\Phi_{\tau}^{(n)}+0.5\Delta t^{-1}\Phi_{\tau-1}^{(n)}, \quad n\in\langle 0,N_M\rangle \tag{2.3.7a}$$

while similar relations resulting from the one-step, self-starting implicit method is given by

$$\left[\Gamma^2D^2-\left(n^2\alpha^2+\Delta t^{-1}\right)\right]\Phi_{\tau+1}^{(n)}=-\Delta t^{-1}\Phi_{\tau}^{(n)}, \quad n\in\langle 0,N_M\rangle. \tag{2.3.7b}$$

In the above the subscript τ denotes the time step and Δt stands for the (constant) length of the time step. Relation (2.3.7a) has the form of an inhomogeneous ordinary differential equation for $\Phi^{(n)}_{\tau+1}$. The following discussion will be carried out in the context of the two-step method, while the relevant relations for the one-step method can be readily deduced. The unknown function $\Phi^{(n)}_{\tau+1}$ can be represented in terms of expansions based on Chebyshev polynomials in the form

$$\Phi^{(n)}_{\tau+1}(\hat{y}) = \sum_{k=0}^{\infty} G^{(n)}_{k,\tau+1} T_k(\hat{y}) \approx \sum_{k=0}^{N_T} G^{(n)}_{k,\tau+1} T_k(\hat{y}) \qquad (2.3.8)$$

where T_k denotes the Chebyshev polynomial of k^{th} order and $G^{(n)}_{k,\tau+1}$ are the unknown coefficients of the expansion. Substitution of (2.3.8) into (2.3.7a) gives

$$\left[\Gamma^2 D^2 - \left(n^2\alpha^2 + 1.5\Delta t^{-1}\right)\right] \sum_{k=0}^{\infty} G^{(n)}_{k,\tau+1} T_k = -2\Delta t^{-1} \sum_{k=0}^{\infty} G^{(n)}_{k,\tau} T_k + 0.5\Delta t^{-1} \sum_{k=0}^{\infty} G^{(n)}_{k,\tau-1} T_k \qquad (2.3.9)$$

We use Galerkin procedure [14-16] to develop equations for the unknowns $G^{(n)}_{k,\tau+1}$, i.e., we multiply both sides of (2.3.9) by $T_j(\hat{y})$ and integrate with the weight function $\hat{\omega} = 1/\sqrt{1-\hat{y}^2}$ to get

$$\begin{aligned} \sum_{k=0}^{N_T} \left[\left\langle T_j, D^2 T_k \right\rangle - \left(n^2\alpha^2 + 1.5\Delta t^{-1}\right)\left\langle T_j, T_k \right\rangle\right] G^{(n)}_{k,\tau+1} &= -2\Delta t^{-1} \sum_{k=0}^{N_T} \left\langle T_j, T_k \right\rangle G^{(n)}_{k,\tau} \\ &+ 0.5\Delta t^{-1} \sum_{k=0}^{N_T} \left\langle T_j, T_k \right\rangle G^{(n)}_{k,\tau-1} \quad , \qquad j \in \left\langle 0, N_T \right\rangle \end{aligned} \qquad (2.3.10)$$

where the inner product is defined as $\left\langle f_j(\hat{y}), g_k(\hat{y}) \right\rangle = \int_{-1}^{1} f_j(\hat{y}) g_k(\hat{y}) \hat{\omega}(\hat{y}) d\hat{y}$. Evaluation of inner products can be significantly simplified by taking advantage of the well known orthogonality properties of the Chebyshev polynomials [14-16]. Equation (2.3.10) leads to N_T-1 decoupled algebraic equations for each Fourier mode; two additional equations required in order to close the system need to be derived from the boundary conditions and these conditions provide coupling between different Fourier modes [5, 11].

The boundary conditions are to be enforced along the lines $\hat{y}_L(x,\tau+1)$ and $\hat{y}_U(x,\tau+1)$ while the solution domain remains fixed at $\hat{y} \in \langle -1,1 \rangle$. To explain the immersed boundary conditions method in general, at time $\tau+1$ we evaluate the unknown $\theta_f(x,\tau+1) \equiv \theta(x,f(x,\tau+1),\tau+1)$ along an arbitrary time dependent line that at time $t=\tau+1$ occupies position $y=f(x,\tau+1)$, such that f is a periodic function with period $\lambda=2\pi/\alpha$ and $|f(x,\tau+1)|\leq 1$. The function $f(x,\tau+1)$ can be expressed without losing generality as

$$f(x,\tau+1) = \sum_{n=-\infty}^{\infty} P_{\tau+1}^{(n)} e^{in\alpha x} \approx \sum_{n=-N_A}^{N_A} P_{\tau+1}^{(n)} e^{in\alpha x} \tag{2.3.11}$$

where one in practice deals with a finite number of terms N_A . The unknown $\theta_f(x,\tau+1)$ is periodic in x with the same period λ and thus can be expressed in terms of Fourier series as

$$\theta_f(x,\tau+1) \equiv \theta\,(x,f(x,\tau+1),\tau+1) = \sum_{n=-N_\theta}^{N_\theta} \varphi_{\tau+1}^{(n)} e^{in\alpha x} \tag{2.3.12}$$

where $N_\theta=N_T N_A+N_M$. Since the flow representation is limited to N_M+1 modes, we will be able to enforce constraints only on the first (N_M+1) terms in (2.3.12). The same unknown can be expressed using the discretized form of the solution, i.e.,

$$\theta_f(x,\tau+1) = \sum_{n=-N_M}^{N_M} \Phi^{(n)}(f(x,\tau+1),\tau+1)e^{in\alpha x} = \sum_{n=-N_M}^{N_M} \sum_{k=0}^{N_T} G_{k,\tau+1}^{(n)} T_k(f(x,\tau+1))e^{in\alpha x} \tag{2.3.13}$$

Since $T_k(f(x,\tau+1))$ is periodic in x, it can be expressed in terms of Fourier expansion as follows

$$T_k(f(x,\tau+1)) = \sum_{m=-N_s}^{N_s} w_{k,\tau+1}^{(m)} e^{im\alpha x} , \tag{2.3.14}$$

where $\max(N_S)=N_T*N_A$. The expansion coefficients in (2.3.14) can be evaluated with the help of the recurrence relation for Chebyshev polynomials in the form $T_{k+1}(\hat{y}) = 2\hat{y}T_k(\hat{y}) - T_{k-1}(\hat{y})$ that leads to the following recurrence relation

$$w_{k+1,\tau+1}^{(m)} = 2 \sum_{n=-\infty}^{\infty} P_{\tau+1}^{(n)} w_{k,\tau+1}^{(m-n)} - w_{k-1,\tau+1}^{(m)} \tag{2.3.15}$$

whose evaluation begins at k=0 and results in

$$w_{0,\tau+1}^{(0)} = 1, \; w_{0,\tau+1}^{(m)} = 0 \; \text{for} \, |m| \geq 1; \qquad w_{1,\tau+1}^{(m)} = P_{\tau+1}^{(m)} \; \text{for} \, |m| \geq 0 . \tag{2.3.16}$$

Substitution of (2.3.14) into (2.3.13) gives

$$\begin{aligned} \theta_f(x,\tau+1) &= \sum_{n=-N_M}^{N_M} \sum_{k=0}^{N_T} \sum_{m=-N_s}^{N_s} G_{k,\tau+1}^{(n)} w_{k,\tau+1}^{(m)} e^{i(n+m)\alpha x} \\ &= \sum_{n=-N_\theta}^{N_\theta} \sum_{m=-N_M}^{N_M} \sum_{k=0}^{N_T} G_{k,\tau+1}^{(m)} w_{k,\tau+1}^{(n-m)} e^{in\alpha x} \end{aligned} \tag{2.3.17}$$

and comparison of (2.3.12) with (2.3.17) gives

$$\varphi_{\tau+1}^{(n)} = \sum_{m=-N_M}^{N_M} \sum_{k=0}^{N_T} G_{k,\tau+1}^{(m)} w_{k,\tau+1}^{(n-m)} . \tag{2.3.18}$$

Equation (2.3.18) can be used to express boundary conditions along the lines $\hat{y}_L(x,\tau+1)$ and $\hat{y}_U(x,\tau+1)$. In the case of our model problem these boundary conditions take the following form

$$\sum_{m=-N_M}^{N_M} \sum_{k=0}^{N_T} G_{k,\tau+1}^{(m)} \left(w_L\right)_{k,\tau+1}^{(n-m)} = \Phi_{L,\tau+1}^{(n)},$$

$$\sum_{m=-N_M}^{N_M} \sum_{k=0}^{N_T} G_{k,\tau+1}^{(m)} \left(w_U\right)_{k,\tau+1}^{(n-m)} = \Phi_{U,\tau+1}^{(n)} \qquad (2.3.19a,b)$$

where $\theta_L(x,\tau+1) = \sum\limits_{n=-N_M}^{N_M} \Phi_{L,\tau+1}^{(n)} e^{in\alpha x}$, $\theta_U(x,\tau+1) = \sum\limits_{n=-N_M}^{N_M} \Phi_{U,\tau+1}^{(n)} e^{in\alpha x}$ and (2.3.19a,b) corresponds to the lower and upper walls, respectively. Equations (2.3.10) and (2.3.19) form a complete set of algebraic equations for the unknown coefficients $G_{k,\tau+1}^{(n)}$, k = 0,….,N_T, n=0,….,N_M. A direct solution of this system moves simulations by one time step forward and the resulting algorithm will be referred to as the direct algorithm.

In the case of time steps of constant length, the coefficients of the discretized Eqs (2.3.10) do not depend on time and thus this part of the coefficient matrix need to be constructed only once at the beginning of the solution process. The matrix entries corresponding to the boundary conditions (2.3.19) need to be reconstructed at every step of the simulations process; the reader should note that this is where the information about the motion of the boundaries enters into considerations.

The matrix of coefficients can be very large when a large number of Fourier modes are required and this motivates the search for an efficient solution method. Before solution is to be carried out the matrix is reduced to a real form by taking advantage of the complex conjugate properties $\Phi^{(n)}(\hat{y},t) = \Phi^{(-n)*}(\hat{y},t)$ (see Eq. 2.3.5) resulting in a structure shown in Fig. 2.2 where the horizontal lines show the coupling effect of boundary conditions (2.3.19) and the blocks of coefficients in the upper triangular form resulting from the discretization of the differential equation (2.3.6) form a band along the diagonal. Such structure suggests the use of an iterative solution algorithm based on the decoupling of Fourier modes. The unknowns corresponding to a Fourier mode of interest in equation (2.3.19) at the current time step can be expressed in terms of the remaining Fourier modes using their values from the previous time step (or from the previous iteration). The solution process begins with mode 0, proceeds to the next mode using the most recent information available and continues until the last mode N_M is reached, and then it is repeated until a convergence criterion is satisfied. In this way, the solution of the complete system of size $(N_T+1)*(2N_M+1)$ is replaced by a repetitive solution of systems of (N_T+1) equations for each Fourier mode. The rate of convergence is generally very good; it decreases with an increase of the current amplitude and the wave number characterizing wall geometry. We shall refer to the iterative algorithm as the "decoupled algorithm" and discuss performance of its various variants in Section 2.5. We wish to stress at this moment that the use of the decoupled algorithm significantly reduces memory requirements as one needs to work with many small matrices instead of one very large matrix as well as it opens the possibility for parallelization of the computations. This issue becomes significant in the case of three-dimensional problems and large number of Fourier modes and Chebyshev polynomials.

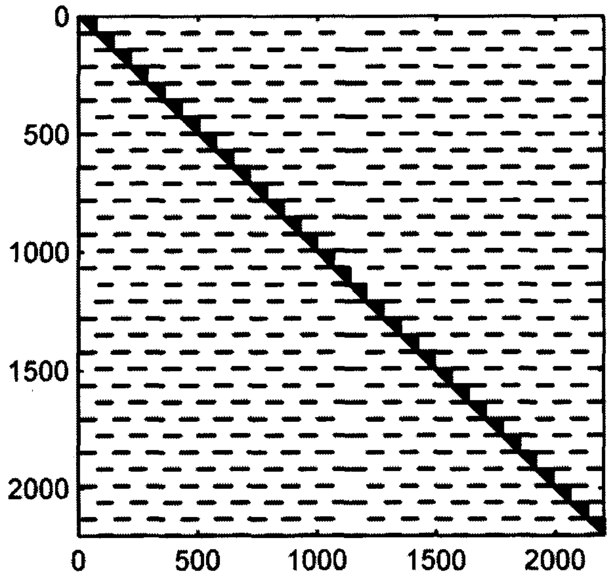

Figure 2.2. *Structure of the coefficient matrix resulting from the implementation of the Immersed Boundary Condition Method for N_M=15 and N_T=70 and the test problem (2.5.7)-(2.5.8). Only non-zero elements are marked.*

2.4. The domain transformation (DT) method

A very popular approach in dealing with moving boundary problems involves adjusting grid so that one of the grid lines always overlaps with the instantaneous location of the boundary [1]. The adjustments may have many forms, extending from analytical mappings to numerical coordinate generation. The adjustments in the shape of elements in the finite element method can also be viewed as a form of mapping. In order to judge the efficiency of the IBC method as compared to all other mapping-type methods, we selected a simple method that relies on analytical mapping. The current shape of the slot in the physical domain (x,y) is mapped into a straight slot in the computational domain (ξ,η) with $\eta \in <-1,1>$ using mapping in the form

$$\xi = x, \qquad \eta = 2\frac{\left(y - y_U(x,t)\right)}{y_U(x,t) - y_L(x,t)} + 1 \qquad (2.4.1)$$

After mapping Eq. (2.2.2) takes the form

$$\frac{\partial^2\theta}{\partial\eta^2} + W_1(\xi,\eta,t)\frac{\partial\theta}{\partial\eta} + W_2(\xi,\eta,t)\frac{\partial^2\theta}{\partial\xi\partial\eta} + W_3(\xi,\eta,t)\frac{\partial^2\theta}{\partial\xi^2} = W_3(\xi,\eta,t)\frac{\partial\theta}{\partial t} \qquad (2.4.2)$$

where $W_1(\xi,\eta,t) = (\eta_{xx} - \eta_t)/(\eta_x^2 + \eta_y^2)$, $W_2(\xi,\eta,t) = 2\eta_x/(\eta_x^2 + \eta_y^2)$ and $W_3(\xi,\eta,t) = 1/(\eta_x^2 + \eta_y^2)$. Expressions for η_t, η_x, η_{xx} and η_y are given below

$$\eta_t = [(y_L)_t(\eta - 1) - (y_U)_t(\eta + 1)]/(y_U - y_L), \quad \eta_x = [(y_L)_\xi(\eta - 1) - (y_U)_\xi(\eta + 1)]/(y_U - y_L),$$

$$\eta_{xx} = \frac{\eta(y_U - y_L)[(y_L)_\xi - (y_U)_\xi][(y_L)_{\xi\xi} - (y_U)_{\xi\xi}] + 2y_L(y_U)_{\xi\xi} - 2y_U(y_L)_{\xi\xi}}{(y_U - y_L)^2} + \frac{-2\eta[(y_U)_\xi - (y_L)_\xi]^2 + 2[(y_U)_\xi^2 - (y_L)_\xi^2]}{(y_U - y_L)^2} \quad \text{and}$$

$$\eta_y = \frac{2}{y_U - y_L},$$

where subscripts ξ, t denote derivative d/dξ, d/dt, respectively.

Solution of (2.4.2) is represented in terms of Fourier expansion as

$$\theta(\xi,\eta,t) = \sum_{n=-\infty}^{\infty} \Psi^{(n)}(\eta,t)e^{in\alpha\xi} \approx \sum_{n=-N_M}^{N_M} \Psi^{(n)}(\eta,t)e^{in\alpha\xi} \tag{2.4.3}$$

where $\Psi^{(n)} = \Psi^{(-n)*}$ and the known coefficients W_1, W_2 and W_3 at each time $t=\tau$ are replaced by their Fourier expansions

$$W_1(\xi,\eta,\tau) = \sum_{m=-2N_M}^{2N_M} w_{1,\tau}^{(m)}(\eta)e^{im\alpha\xi}, \quad W_2(\xi,\eta,\tau) = \sum_{m=-2N_M}^{2N_M} w_{2,\tau}^{(m)}(\eta)e^{im\alpha\xi},$$

$$W_3(\xi,\eta,\tau) = \sum_{m=-2N_M}^{2N_M} w_{3,\tau}^{(m)}(\eta)e^{im\alpha\xi}. \tag{2.4.4}$$

Substitution of (2.4.3) and (2.4.4) into (2.4.2), separation of Fourier components and the use of a two step implicit method for the temporal discretization leads to

$$\begin{aligned} D^2\Psi_{\tau+1}^{(n)} + \sum_{s=-N_M}^{N_M}\left[w_{1,\tau+1}^{(n-s)} + is\alpha w_{2,\tau+1}^{(n-s)}\right]D\Psi_{\tau+1}^{(s)} - \sum_{s=-N_M}^{N_M}\left[(s\alpha)^2 + 1.5\Delta t^{-1}\right]w_{3,\tau+1}^{(n-s)}\Psi_{\tau+1}^{(s)} \\ = -2\Delta t^{-1}\sum_{s=-N_M}^{N_M} w_{3,\tau}^{(n-s)}\Psi_{\tau}^{(s)} + 0.5\Delta t^{-1}\sum_{s=-N_M}^{N_M} w_{3,\tau-1}^{(n-s)}\Psi_{\tau-1}^{(s)}, \qquad n \in \langle 0, N_M \rangle \end{aligned} \tag{2.4.5a}$$

where D=d/dη. A similar expression for the one step implicit method has the form

$$D^2\Psi_{\tau+1}^{(n)} + \sum_{s=-N_M}^{N_M}\left[w_{1,\tau+1}^{(n-s)} + is\alpha w_{2,\tau+1}^{(n-s)}\right]D\Psi_{\tau+1}^{(s)} - \sum_{s=-N_M}^{N_M}\left[(s\alpha)^2 + \Delta t^{-1}\right]w_{3,\tau+1}^{(n-s)}\Psi_{\tau+1}^{(s)}$$
$$= -\Delta t^{-1}\sum_{s=-N_M}^{N_M} w_{3,\tau}^{(n-s)}\Psi_{\tau}^{(s)} \quad , \qquad n \in \langle 0, N_M \rangle \ . \tag{2.4.5b}$$

The reader may note that all equations (2.4.5a,b) are coupled together through the known variable coefficients. The unknown $\Psi_{\tau+1}^{(n)}(\eta)$ can be expressed with spectral accuracy using the Chebyshev expansion in the form

$$\Psi_{\tau+1}^{(n)}(\eta) = \sum_{k=0}^{\infty} F_{k,\tau+1}^{(n)}\, T_k(\eta) \ \approx \sum_{k=0}^{N_T} F_{k,\tau+1}^{(n)}\, T_k(\eta) \ . \tag{2.4.6}$$

Use of the Galerkin procedure described in Section 2.3 leads to N_T-1 algebraic equations for $F_{k,\tau+1}^{(n)}$ for each Fourier mode. The remaining closing conditions come from the boundary conditions.

The treatment of boundary conditions follows standard procedures. The boundary conditions have the form

$$\theta(\xi, \eta = -1, t) = \theta_L(\xi, t) = \sum_{n=-N_M}^{N_M} \Psi_L^{(n)}(t) e^{in\alpha\xi} ,$$

$$\theta(\xi, \eta = 1, t) = \theta_U(\xi, t) = \sum_{n=-N_M}^{N_M} \Psi_U^{(n)}(t) e^{in\alpha\xi} \tag{2.4.7a,b}$$

Use of (2.4.3) leads to the boundary conditions for each Fourier mode in the form

$$\Psi^{(n)}(-1, t) = \Psi_L^{(n)}(t), \quad \Psi^{(n)}(1, t) = \Psi_U^{(n)}(t) . \tag{2.4.8a,b}$$

Introduction of Chebyshev expansion (2.4.6) leads to the required closing conditions in the form

$$\sum_{k=0}^{N_T}(-1)^k F^{(n)}_{k,\tau+1} = \Psi^{(n)}_{L,\tau+1} \quad , \quad \sum_{k=0}^{N_T} F^{(n)}_{k,\tau+1} = \Psi^{(n)}_{U,\tau+1} \tag{2.4.9a,b}$$

The above process leads to a system of equations with a full matrix of coefficients. Solution of this system moves simulations by one time step forward and this approach has been referred to in the previous section as the direct algorithm. As the matrix is full, no special iterative algorithm can be proposed. All entries corresponding to differential equations (2.4.5a) need to be reconstructed at the each time step while entries corresponding to boundary conditions remain essentially unchanged, which is opposite to what had to be done in the case of the IBC method. This observation suggests that the IBC method could be significantly faster when the cost of construction of the coefficient matrix is significant. This issue will be discussed in the next section.

2.5. Testing of the algorithms

We shall discuss performance of the algorithms in the context of two convenient test problems involving movements of boundaries, i.e., movements of the upper wall corresponding (i) to an elastic traveling wave and (ii) to a elastic standing wave.

2.5.1. Elastic traveling wave

Consider an elastic wave traveling along the upper wall with the lower wall being flat. The shape of the resulting slot can be described as

$$y_U(x,t) = 1+S\cos[\alpha(x-ct)], \qquad y_L=-1. \tag{2.5.1}$$

where c denotes the phase speed, α denotes the wave number and S stands for the amplitude of the wave. Time variations of the shape of the slot are illustrated in Fig. 2.3.

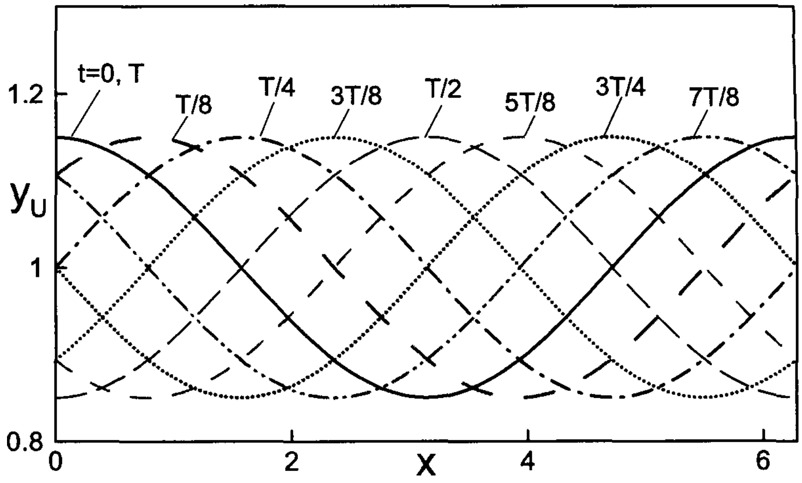

Figure 2.3. *Shape of the upper wall deformed by elastic traveling wave described by Eq.(2.5.1) with the amplitude S=0.15, the wave number α=1.0 and the phase speed c=π at t=0, T/8, T/4, 3T/8, T/2, 5T/8, 3T/4, 7T/8 and T, where T denotes one time period.*

We wish to determine variations of the temperature in the interior of the slot while keeping the temperature of the upper wall at $\theta_U=0$ and at the lower wall at $\theta_L=1$. Use of the Galilean transformation

$$X=x-ct \qquad (2.5.2)$$

transforms the unsteady moving boundary problem into a steady fixed boundary problem with a sinusoidal upper wall. The full problem in the moving frame of reference (X,y) has the form

$$\partial^2\theta/\partial X^2 + c\,\partial\theta/\partial X + \partial^2\theta/\partial y^2 = 0 \qquad (2.5.3)$$

with boundary conditions in the form

$$\theta(X,-1)=1, \qquad \theta(y_U(X))=0 \text{ where } y_U=1+S\cos(\alpha X). \tag{2.5.4}$$

Problem (2.5.3)-(2.5.4) is solved using IBC method and its performance can be judged by determining the error of enforcement of boundary conditions at the upper wall as a function of the amplitude and the wave number of the wave. For convenience, we use the L_∞ norm for θ evaluated at the upper wall defined as

$$\|\theta_U(X)\|_\infty = \sup_{0\le X\le 2\pi/\alpha} |\theta(X, y_U(X))| \tag{2.5.5}$$

as a quantitative measure of the error. This norm is very strict and thus provides an unambiguous means to judge the accuracy of enforcement of boundary conditions. Dependence of boundary error as a function of geometric parameters for a fixed number of Fourier modes N_M is illustrated in Figs 2.4 and 2.5. The reader may note in judging these results that S=2 corresponds to a situation when the lowest extreme of the upper wall touches the lower wall. The available results suggest that the error is at machine accuracy level if α and S are below certain critical values. Once these values are reached, the error begins to increase rapidly in a fairly universal manner. This critical values of α and S can be increased by increasing the number of Fourier modes N_M used in the calculation, but the qualitative character of the error increase remains unchanged.

Distribution of temperature along the upper wall $\theta_U(X)$ over a single spatial period is displayed in Fig. 2.6. The expected value is zero, however the actual value is different and its magnitude illustrates the error in the enforcement of boundary conditions. This error is oscillatory in X with the maximum occurring around X=0 and λ, i.e., around the upper extreme of the deformed wall. The same problem has been solved directly in the fixed coordinate system as a moving boundary problem and the error variations as a function of time are illustrated in Fig. 2.7. It can be seen that the magnitude and pattern of distribution of the error remain the same as a function of time, however, the pattern shifts in the direction of the positive x-axis with the phase speed of the wave, i.e., its maximum follows the movement of the upper extreme of the wall.

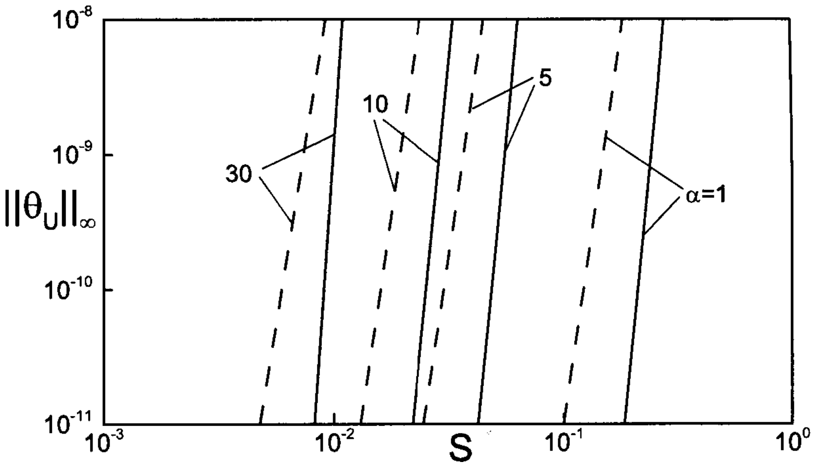

Figure 2.4. *The* $\|\theta_U(X,t)\|_\infty$ *norm (see Eq. 2.5.5) evaluated using the IBC method as a function of the wave amplitude S for selected values of the wave number α for the model problem (2.5.3)-(2.5.4) with c=π. The dashed and solid lines represent results obtained with the* N_M *= 10, 15 Fourier modes, respectively. The reader may note that S=2 corresponds to the trough of the wave reaching the bottom wall.* N_T*=70 Chebyshev polynomials were used in the calculations.*

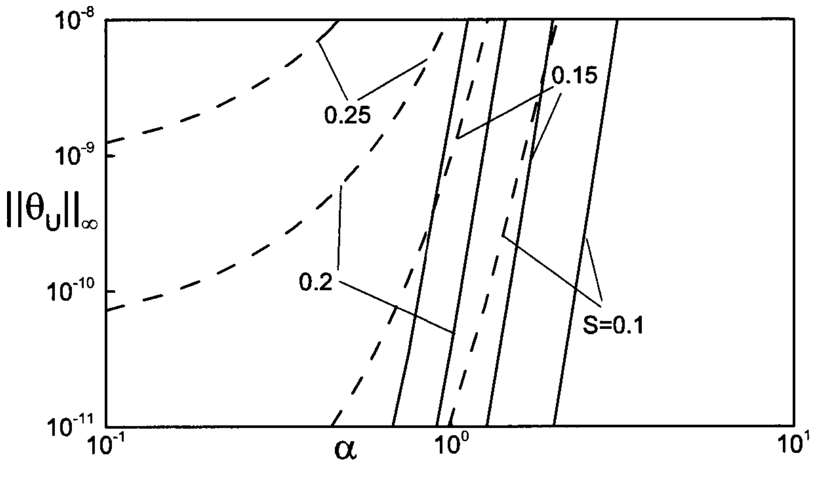

Figure 2.5. *The* $\|\theta_U(X,t)\|_\infty$ *norm (see Eq. 2.5.5) evaluated using the IBC method as a function of the wave number α for selected values of the wave amplitude S for the model problem (2.5.3)-(2.5.4) for c=π. The dashed and solid lines represent results obtained with the* N_M *= 10, 15 Fourier modes, respectively. The reader may note that S=2 corresponds to the trough of the wave reaching the bottom wall.* N_T*=70 Chebyshev polynomials were used in the calculations.*

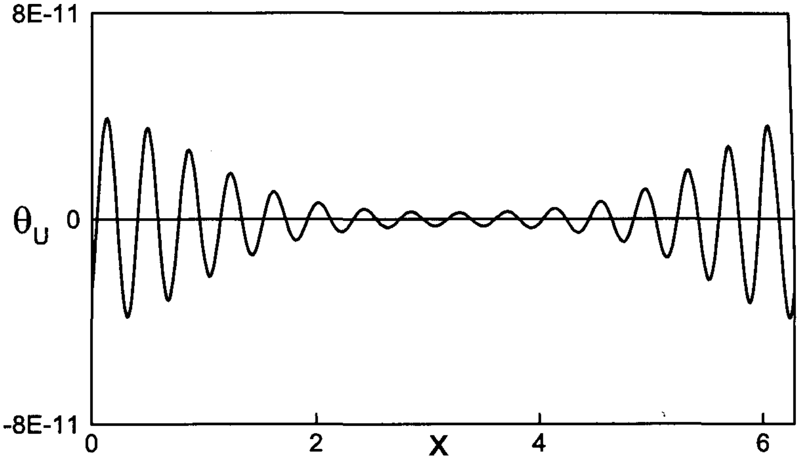

Figure 2.6. *Distribution of temperature at the upper wall θ_U for the model problem (2.5.3)-(2.5.4) with the phase speed $c=\pi$, the amplitude $S=0.2$ and the wave number $\alpha=1$. The presented results were obtained using the IBC method with $N_M=15$ Fourier modes and $N_T=70$ Chebyshev polynomials.*

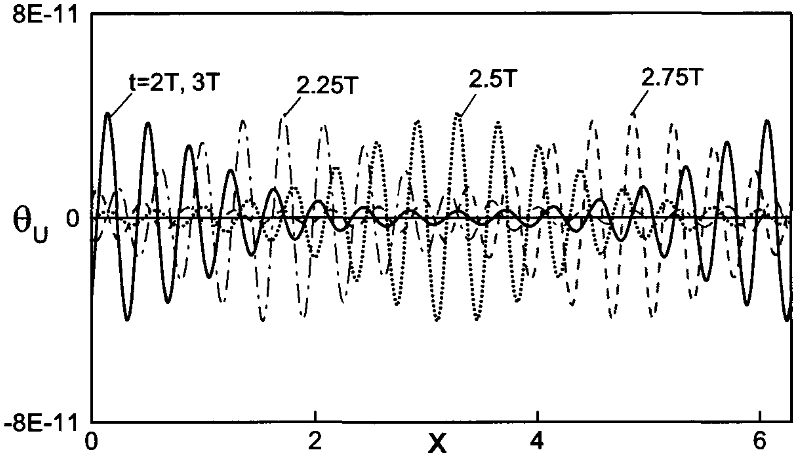

Figure 2.7. *Distribution of temperature at the upper wall θ_U at t = 2T, 2.25T, 2.5T, 2.75T and 3T, where T stand for one time period, for the model problem (2.5.3)-(2.5.4) with $S=0.2$, $\alpha=1.0$ and $c=\pi$. The presented results were obtained through a direct solution of the moving boundary problem in the fixed coordinates system (x,y) using the IBC method with $N_M=15$ Fourier modes and $N_T=70$ Chebyshev polynomials. Solution corresponding to the fixed boundary problem in the moving frame of reference was used as the initial condition. Presented results correspond to the 3^{rd} period after initiations of the calculations.*

Figure 2.8 illustrates variations of the temperature at a few test points as a function of time over five time periods determined using direct solution of (2.5.3)-(2.5.4) in the fixed frame of reference, i.e., solving it as a moving boundary problem. It can be seen that the algorithm faithfully reproduces the oscillatory character of temperature variations and the phase shift between different spatial locations. Figure 2.9 illustrates spatial distribution of the heat flux at the upper wall for the same problem as a function of time over one time period. Changes in the variations of the spatial distributions of the heat flux as a function of time demonstrate a correct phase shift. Figure 2.10 illustrates variations of the maximum error in the evaluation of the temperature as a function of the temporal step size Δt. The character of these variations demonstrates that the algorithm delivers the first- and second-order accuracy for time simulations, as theoretically predicted. Solution of the fixed boundary problem in the moving frame of reference was used as the initial condition for the solution of the moving boundary problem.

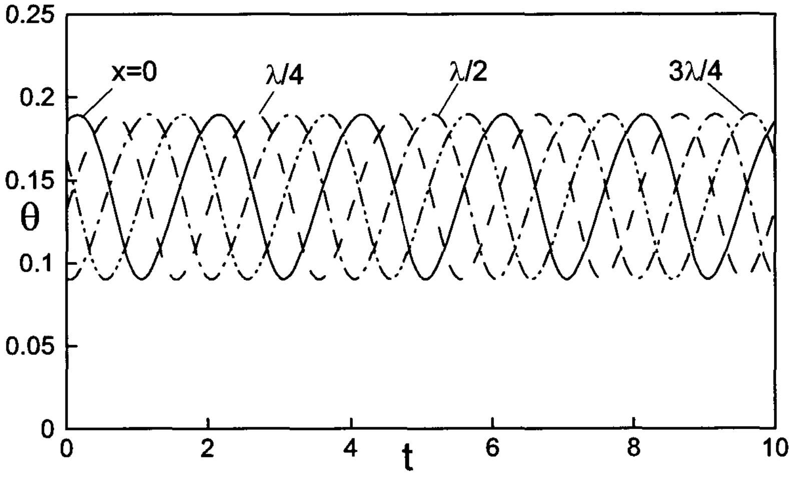

Figure 2.8. *Variations of the temperature θ at points (x,y) = (0, 0.7), (λ/4, 0.7), (λ/2, 0.7), (3λ/4, 0.7) for the model problem (2.5.3)-(2.5.4) with the amplitude S=0.15, the wave number α=1.0 and the phase speed c=π solved directly as a moving boundary problem in the fixed reference frame for five time periods. Solution of the corresponding fixed boundary problem in the moving frame of reference was used as the initial condition.* N_M*=15 Fourier modes and* N_T*=70 Chebyshev polynomials were used in the computations.*

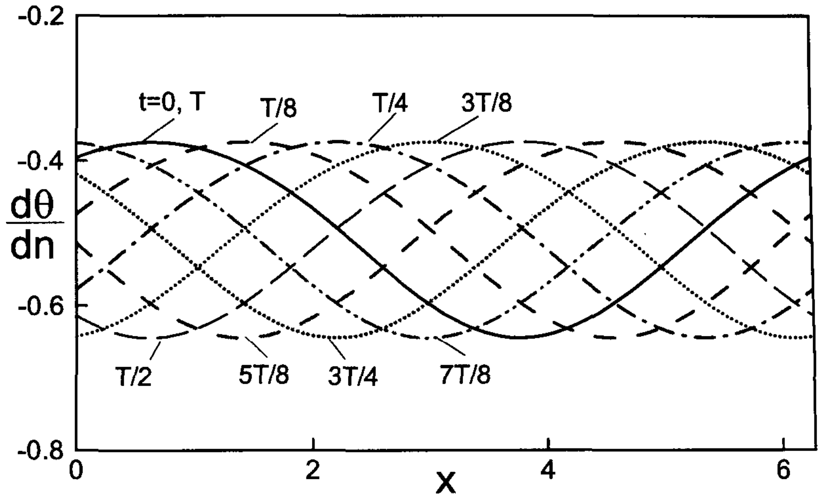

Figure 2.9. *Variations of heat flux distribution at the upper wall at times t=0, T/8, T/4, 3T/8, T/2, 5T/8, 3T/4, 7T/8 and T, where T stand for one time period. Other conditions as in Fig. 2.8.*

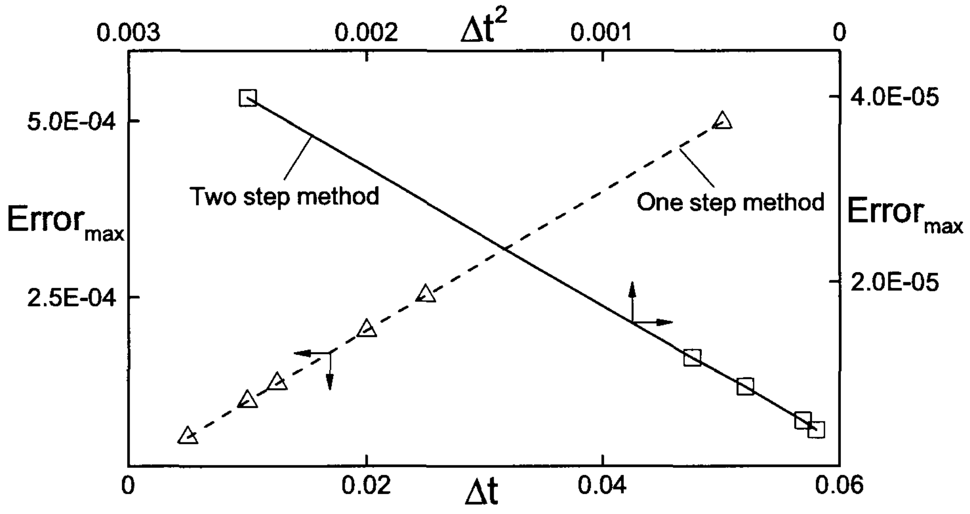

Figure 2.10. *Variations of the maximum error as a function of the step size Δt used in the temporal discretization in the case of the model problem (2.5.3)-(2.5.4) with the amplitude S=0.05, the wave number α=1.0 and the phase speed c=π. Error is defined as the difference between the results obtained through the direct solution of the moving boundary problem in the fixed frame of reference and the corresponding fixed boundary problem in the moving frame of reference at a time corresponding to t=1.0. N_M=10 Fourier modes and N_T=60 Chebyshev polynomials were used in the computations.*

2.5.2. Elastic standing wave

Consider elastic standing wave at the upper wall with the lower wall being flat. The shape of the slot can be described as

$$y_U(x,t) = 1+S\sin(\alpha x)\cos(\omega t), \qquad y_L=-1, \qquad (2.5.6)$$

where α denotes the wave number, S stands for the amplitude and ω denotes the frequency of the wave. Time variations of the shape of the slot are illustrated in Fig. 2.11.

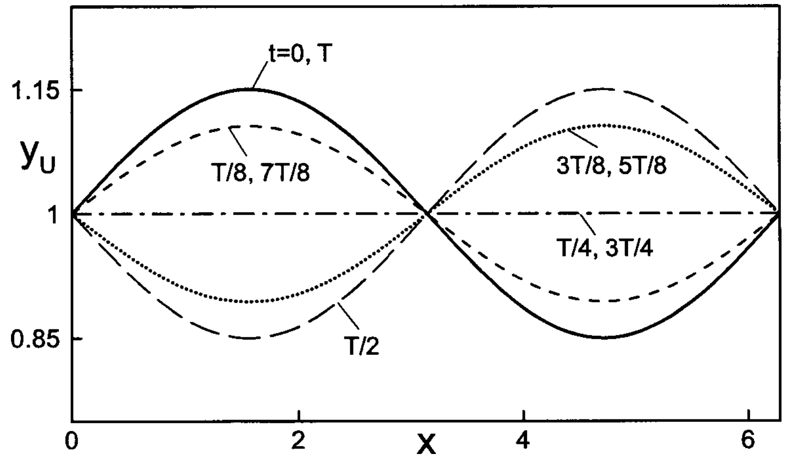

Figure 2.11. *Shape of the upper wall deformed by elastic standing wave described by Eq.(2.5.6) with the wave number α=1.0, the amplitude S=0.15 and the frequency ω=π at times t=0, T/8, T/4, 3T/8, T/2, 5T/8, 3T/4, 7T/8 and T, where T denotes one time period.*

We wish to determine variations of the temperature in the interior of the slot while keeping the temperature of the upper wall at θ_U=0 and at the lower wall at θ_L=1. The full test problem has the form

$$-\partial\theta/\partial t+\partial^2\theta/\partial x^2+\partial^2\theta/\partial y^2=0 \qquad (2.5.7)$$

with boundary conditions in the form

$$\theta(x,-1,t)=1, \qquad \theta(x, y_U(x,t), t)=0 \text{ where } y_U=1+S\sin(\alpha x)\cos(\omega t). \tag{2.5.8}$$

For convenience, we use the L_∞ norm for θ evaluated at the upper wall defined as

$$\left\|\theta_U(x,t)\right\|_\infty = \sup_{0\le X\le 2\pi/\alpha} \left|\theta(x, y_U(x,t), t)\right| \tag{2.5.9}$$

as a quantitative measure of the error.

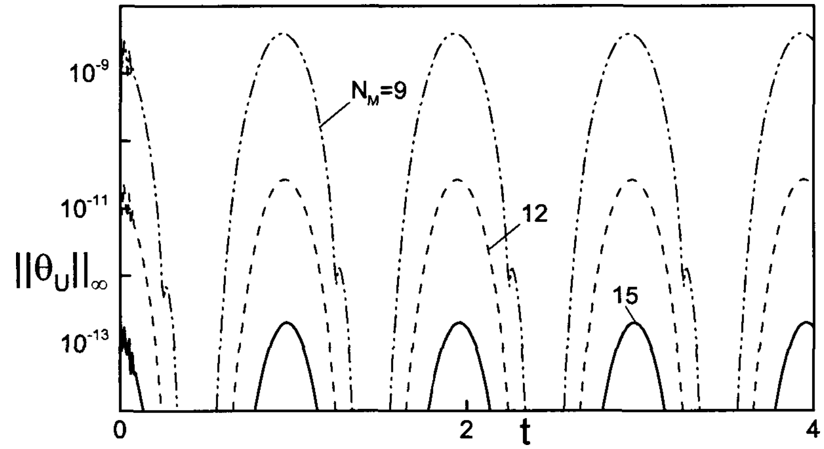

Figure 2.12. Variation of the $\left\|\theta_U(x,t)\right\|_\infty$ *norm as a function of time over two time periods for the model problem (2.5.7)-(2.5.8).* N_T*=70 Chebyshev polynomials were used and the solid, dash and dotted lines corresponds to* N_M*=15, 12, 9 Fourier modes. Solution of the fixed boundary problem for the geometry described by (2.5.8) with t=0 was used as an initial conditions. All other conditions are as in Fig. 2.11.*

Figure 2.12 illustrates variations of the above norm over two time periods with the initial conditions corresponding to the solution of a fixed boundary problem with the shape of the boundaries described by (2.5.8) at t=0. It can be seen that the error changes periodically in time with the frequency equal to double of the frequency of the standing wave. The maximum of the error occurs at times when the slot opening reaches maximum. The location of the maximum error follows location of the maximum slot opening as illustrated in Fig. 2.13. The character of the error remains unchanged as a function of time which points to the robustness of the algorithm. The magnitude of the error can be reduced by increasing the number of Fourier modes used in the calculations but its qualitative features remain the same, as illustrated in Fig. 2.12.

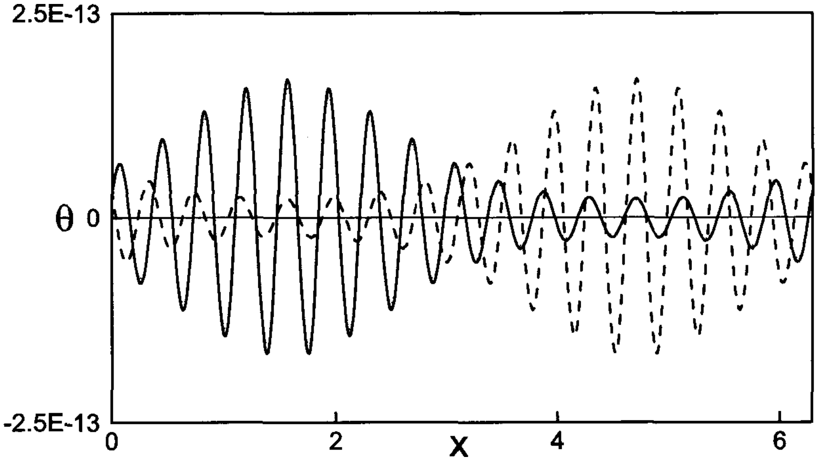

Figure 2.13. *Distribution of temperature of the upper wall θ_U after three (solid line) and three and half time periods (dashed line) for the model problem (2.5.7)-(2.5.8) evaluated using the IBC method with N_M=15 Fourier modes and N_T=70 Chebyshev polynomials. Solution of a fixed boundary problem corresponding to geometry described by Eq.(2.5.8) with t=0 was used as the initial condition. All other conditions are as in Fig. 2.11.*

The IBC algorithm enforces zero conditions for only the first N_M Fourier modes. Behavior of the remaining available Fourier modes (for $N_M+1 < n < N_\theta$) provides an illustration of the error behavior and this is illustrated in Fig. 2.14. The first N_M Fourier modes are indeed zero and the maximum error is associated with the first neglected mode. As the magnitude of the error is related to the size of the slot opening, this error is expected to be the same every half time period and this is indeed the case, as shown in Fig. 2.14. The same figure displays error associated with solving the same problem using different sizes of the "computational box" and thus using different forms of Fourier expansions. It can be seen that the error is associated with different (but easily predicted) terms of the Fourier expansions and its magnitude does not change. It has been observed that the algorithm does not permit spurious error transfer between different Fourier modes and does not generate any spurious spatial oscillations.

The accuracy of determination of temperature θ in the interior of the slot is dominated by the error associated with the temporal discretization, as the spatial discretization has spectral character and thus is typically much more accurate. Results shown in Fig. 2.15 demonstrate that the algorithm does deliver the first- and second-order temporal accuracy, as theoretically predicted.

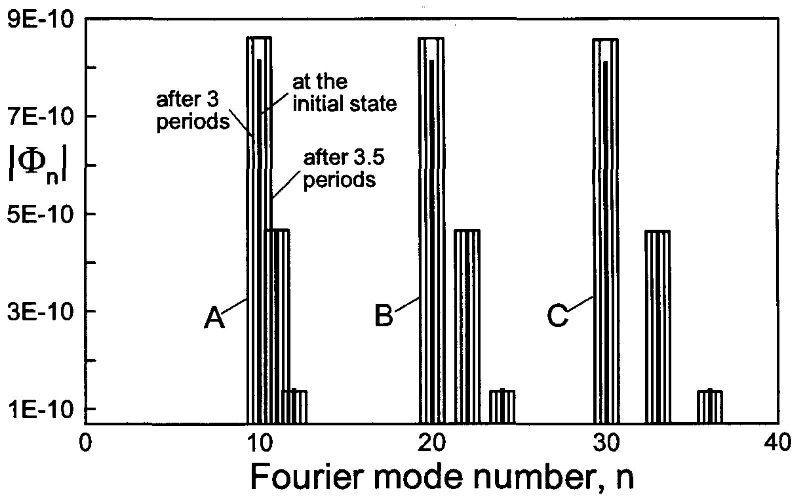

Figure 2.14. *Fourier spectra of temperature distribution at the upper wall θ_U for the model problem (2.5.7)-(2.5.8) with the amplitude S=0.15, the frequency $\omega=\pi$ and the wavelength of the standing wave $\lambda=2\pi$. The initial conditions correspond to the solution of a fixed boundary problem for the geometry given by (2.5.8) with t=0. Three different forms of Fourier expansions were considered, i.e., case A: $\alpha=1.0$, $N_M=9$; case B: $\alpha=0.5$, $N_M=18$ and case C: $\alpha=1/3$, $N_M=27$. $N_T=70$ Chebyshev polynomials used in all cases.*

Figure 2.16 illustrates time variations of the temperature in the interior of the slot. It can be seen that these variations have strictly periodic character, as expected. The instantaneous isotherms inside a slot deformed by an elastic wave with a more complex shape are illustrated in Fig. 2.17. The variations of the heat flux at the upper wall for the same slot are illustrated in Fig. 2.18. These results illustrate the ability of the algorithm to deal with complex movements of the boundaries that require the use of several Fourier modes.

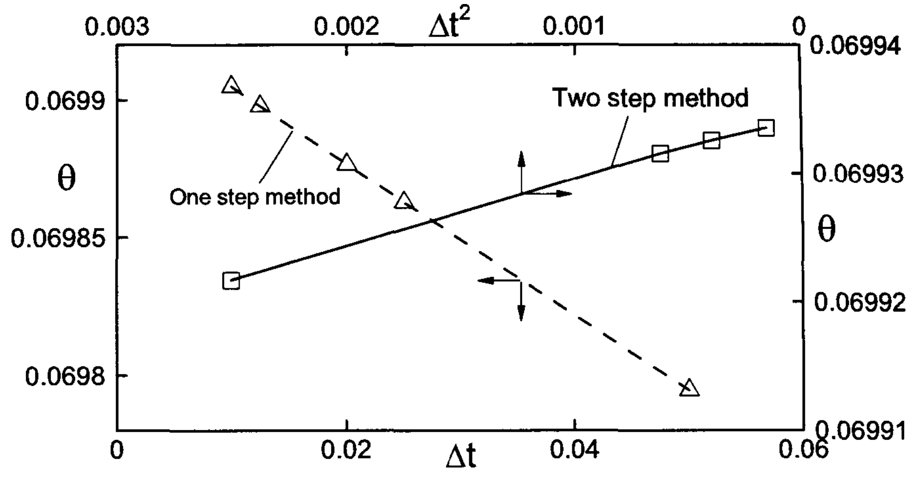

Figure 2.15. Variations of temperature θ as a function of the step size Δt at a test point (2.x,y)=(3π/2, 0.7) for the model problem (2.5.7)-(2.5.8) with S=0.05, α=1 and ω=π at a time t=T+1.0 where T denotes time period computed with N_M=10 and N_T=60 . The initial conditions correspond to the solution of a fixed boundary problem for the geometry given by (2.5.8) with t=0.

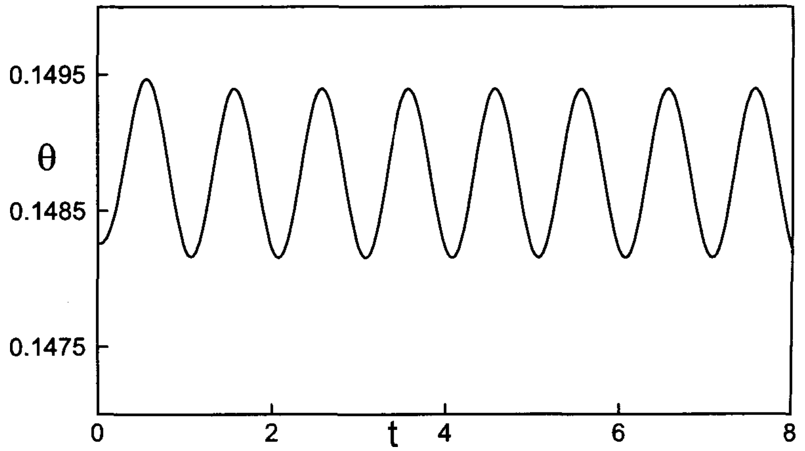

Figure 2.16. The evolution of θ at a test point (x,y)=(0,0.7) during the first four time periods for the model problem (2.5.7)-(2.5.8) with the wave properties described in Fig. 2.11 computed with N_M=10 and N_T=60. The initial conditions correspond to the solution of a fixed boundary problem for the geometry given by (2.5.8) with t=0.

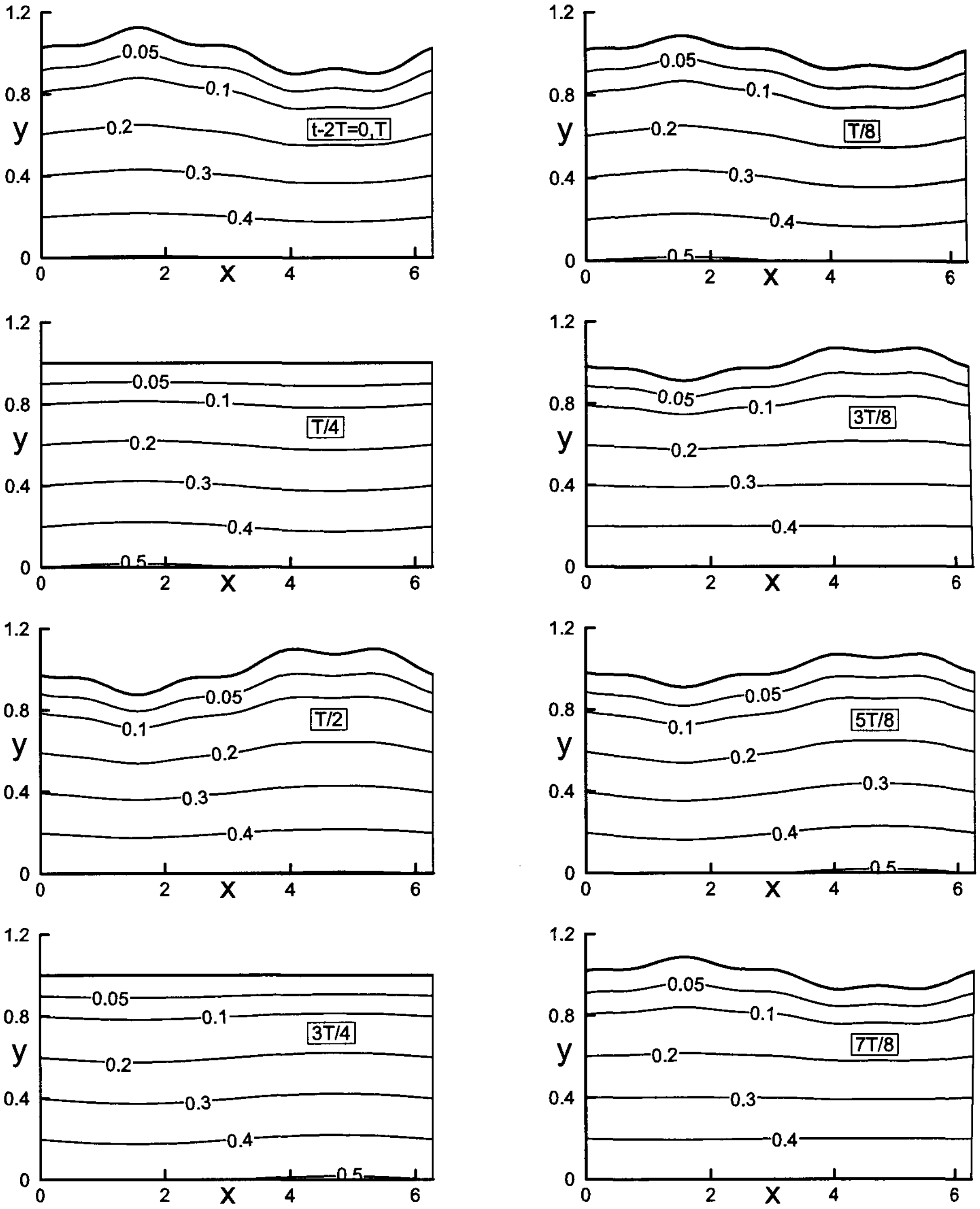

Figure 2.17. *Instantaneous isotherms in the upper part of a slot bounded by $y_L(x,t) = -1$, $y_U(x,t) = 1+(-0.05ie^{ix} + 0.0125e^{4ix} +CC)\cos(\omega t)$ for $\omega=\pi$ using $N_M=15$ and $N_T=70$ evaluated after two time periods at times t-2T=0, T/8, T/4, 3T/8, T/2, 5T/8, 3T/4, 7T/8 and T, where T stands for one time period and CC is the abbreviation for complex conjugate. The initial conditions correspond to the solution of a fixed boundary problem in a slot with geometry given by the above equation with t=0.*

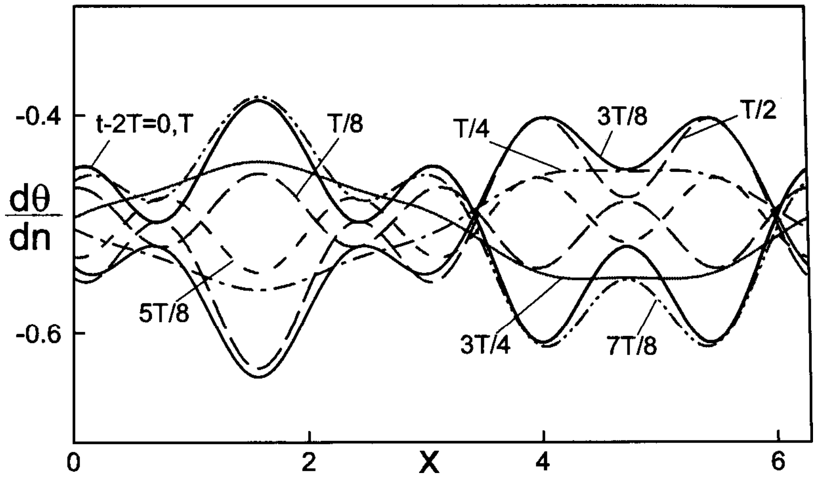

Figure 2.18. *Variations of heat flux distribution at the upper wall in a slot with the flat lower wall $y_L(x,t)$ = -1 and a elastic standing wave in the form $y_U(x,t)$ = 1+(-0.5Sie$^{i\alpha x}$ + 0.125Se$^{4i\alpha x}$ +CC) cos(ωt) with S=0.1, α=1.0 and ω=π at the upper wall at times t-2T=0, T/8, T/4, 3T/8, T/2, 5T/8, 3T/4, 7T/8 and T, where T stands for one time period and CC is the abbreviation for complex conjugate. The initial conditions correspond to the solution of a fixed boundary problem for the geometry corresponding to the shape of the slot at time t=0. The results were determined using N_M=15 Fourier modes and N_T=70 Chebyshev polynomials.*

2.5.3. Efficiency of the algorithm

Efficiency of the algorithm is dictated by the cost of construction of the matrix of coefficients and solution of the resulting system of linear equations. Both actions have to be repeated at each step of the time-dependent solution process. All tests referred to in the discussion below had been carried out in the MATLAB computing environment using the same hardware.

Structure of the matrix in the case of IBC method has been discussed in Section 2.3. Entries corresponding to the field equations need to be computed only once at the very beginning of the computations as they remain unchanged. Entries corresponding to the boundary conditions need to be re-computed at each time step as they change due to the movement of the boundaries. In contrary, all entries need to be recomputed at each time step in the DT method. In addition, the cost of a single construction of the coefficient matrix is significantly higher in the case of the DT method due to the presence of numerous and complex coefficients in the equations. The relative advantage of the IBC method is illustrated by noting that in the case of the model problem (2.5.7)-(2.5.8) with N_M=15 Fourier modes and N_T=70 Chebyshev polynomials it took 592 seconds to construct a complete matrix in the case of DT method but only about 8 seconds in the IBC method. The latter is significantly reduced at the next time step, while the former has to be entirely repeated, which adds to the relative advantage of the IBC method. For this reason the development of the DT method has not been pursued.

Table 2.1. *Time requirements for the direct and various iterative/decoupled schemes for the IBC algorithm for the model problem (5.7)-(5.8) with $S=0.1$, $\alpha=1.0$, $\omega=\pi$ and $N_T=70$. Computations have been carried out using two-step implicit method with $\Delta t=0.01$.*

Number of Fourier modes, N_M	Time required for 100 time steps (in seconds)			
	Direct algorithm	Decoupled algorithm		
		Version A	Version B	Version C
10	299.9	34.8	32.9	29.2
15	880.7	86.6	84.3	83.2

Once constructed, the solution of the system of linear equations can be carried out using standard methods resulting in a direct algorithm, as discussed in Section 2.3. Since the coefficient matrix in the DT method is full, no savings associated with special features of the matrix can be expected. Matrix in the case of IBC method has a special structure and this provides opportunity to use iterative algorithm. The performance of different iterative/decoupled schemes is illustrated in Table 2.1 and compared with the direct algorithm. Since the overall accuracy of the time-dependent solution is determined by the error of the temporal discretization, the convergence criterion for the decoupled algorithms in these tests had been set at 10^{-5} in order to make it comparable with the error in time. The performance of the decoupled algorithm can be improved by taking advantage of the information available at the previous time step and re-arranging the iteration strategy. Three different strategies have been tested. Version A has been described in Section 2.3, version B uses extrapolated values of the modal functions during the first iteration and continues iterations until convergence criteria are met and version C uses only extrapolated values of the modal functions and eliminates iterations. In all cases the method remains second-order accurate as the extrapolation provides second-order accuracy in time. The results (see Table 2.1) show significant savings resulting from the use of iterative/decoupled algorithms as compared with the direct algorithm. The distinction between different iterative algorithms and their limitations are illustrated in Table 2.2. The cost of the direct algorithm remains the same regardless of the magnitude of amplitude S of the standing wave. The cost of version A of the iterative algorithm increases as the amplitude S increase and, for sufficiently high value of S the algorithm diverges. Versions B and C behave in a similar manner but diverge for smaller values of S. The relative performances of different versions of the iterative algorithm are very similar, and they all require less computer time as compared with the direct algorithm by an order of magnitude. The direct algorithm however provides access to much larger amplitudes of boundary motions.

Table 2.2. *Time requirement for the direct and various iterative/decoupled schemes for the IBC algorithm for the model problem (5.7)-(5.8) with $\alpha=1.0$, $\omega=\pi$, $N_M=15$ and $N_T=70$ for various level of wave amplitude. All other conditions are same as Table 2.1.*

Wave amplitude, S	Time required for 100 time steps (in seconds)			
	Direct algorithm	Decoupled algorithm		
		Version A	Version B	Version C
0.05	880.0	84.6	83.2	83.1
0.10	880.7	86.6	84.3	83.2
0.15	879.7	94.4	88.4	*
0.20	880.2	104.4	110.3	*
0.25	880.2	156.9	*	*
0.30	880.3	*	*	*
0.35	880.5	*	*	*

* *indicates failure for the decoupled algorithm to satisfy the required convergence criteria*

2.6. Conclusions

We have developed a fully-implicit, spectrally-accurate algorithm for moving boundary problems using immersed boundary conditions concept. Computations are carried out using a fixed computational domain where the field equations are discretized using a combination of Fourier and Chebyshev expansions. Boundary of the physical domain moves through the computational domain and its location is tracked using the concept of immersed boundary conditions, i.e., the boundary conditions are replaced by constraints that enforce physical conditions along lines internal to the solution domain. The algorithm provides sharp resolution of the location of the moving boundary similar to the case of algorithms based on mapping methods where one of the coordinate lines overlap with the moving boundary. The computational cost of the algorithm is significantly smaller as compared with the mapping-based algorithms because the part of the coefficient matrix that corresponds to the field equations needs to be constructed only once and only entries corresponding to boundary conditions need to be recomputed at each time step. The coefficient matrix has special structure that provides opportunities for the use of much more efficient iterative solution methods. These methods can reduce the overall computational cost by an order of magnitude as compared to the direct method, however, they limit the ability of the algorithm to handle large-amplitude motions of the boundaries. Such algorithms remain of interest nevertheless as they can be easily parallelized and require less memory.

2.7. References

[1] Floryan, J.M. and Rasmussen, H., Numerical analysis of viscous flows with free surfaces, *Appl. Mech. Rev.*, vol. 42, pp. 323-341 (1989).

[2] Glimm, J., Grove, J.W., Li, X.L., Shyue, K.M., Zeng, Y. and Zhang, Q., Three-Dimensional Front Tracking, *SIAM J. Sci. Computing,* vol. 19, pp. 703-727 (1998).

[3] Harlow, F.H. and Welch, J.E., Numerical Study of Large Amplitude Free Surface Motions, *Phys.Fluids*, vol. 9, pp. 842-851 (1966).

[4] Hirt, C.W. and Nichols, B.D., Volume of Fluid (VOF) Method for the Dynamics of Free Boundaries, *J.Comp.Phys.*, vol. 39, pp. 201-225 (1981).

[5] Husain, S.Z. and Floryan, J.M., Immersed boundary conditions method for unsteady flow problems described by the Laplace operator, *Int. J. Num. Meth. Fluids*, vol. 56, pp. 1765-1786 (2007).

[6] Hyman, J.M., Numerical Methods for Tracking of Interfaces, *Physica,* vol. 12D, pp. 396-407 (1984).

[7] Kogut, L., The Influence of Surface Topography on the Electromechanical Characteristics of Parallel-Plate Capacitors, *J. Micromech. Microeng.*, vol. 15, pp. 1068-1075 (2005).

[8] Mittal, R. and Iaccarino, G., Immersed boundary methods, *Annu. Rev. Fluid Mech.,* vol. 37 pp. 239-261 (2005).

[9] Osher, S.J. and Sethian, J.A., Fronts Propagating with Curvature Dependent Speed: Algorithms Based on Hamilton-Jacobi Formulations, *J. Comp .Phys.*, vol. 79, pp. 12-49 (1988).

[10] Peskin, C.S., The fluid dynamics of heart valves: experimental, theoretical and computational methods, *Annu. Rev. Fluid Mech.,* vol. 14 pp. 235-59 (1982).

[11] Szumbarski, J. and Floryan, J.M., A direct spectral method for determination of flows over corrugated boundaries, *J. Comp. Phys.*, vol. 153, pp. 378-402 (1999).

[12] Scardovelli, R. and Zaleski, S., Direct Numerical Simulation of Free Surface and Interfacial Flow, *Annu Rev. Fluid Mech.*, vol. 31, pp. 567-603 (1999).

[13] Osher, S.J. and Sethian, J.A., Fronts Propagating with Curvature Dependent Speed: Algorithms Based on Hamilton-Jacobi Formulations, *J. Comp .Phys.*, vol. 79, pp. 12-49 (1988).

[14] Canuto, C., Hussaini, M.Y., Quarteroni, A., and Zang, T.A., Spectral methods in fluid dynamics, *Springer* (1987).

[15] Peyret, R., Spectral methods for incompressible viscous flow, *Springer* (2002).

[16] Boyd, J.P., Chebyshev and Fourier spectral methods, *Dover Publishers* (2001).

CHAPTER 3

Moving boundary problems described by the biharmonic operator[1]

3.1. Introduction

The first step in the most common approach used for simulations of flows in complex geometries involves numerical modeling of geometry of the flow domain. A model of the domain is constructed using grid generator and flow boundary conditions are imposed on the edges of this domain, i.e., the flow domain overlaps with the computational domain. This process, which is frequently referred to as pre-processing, could consume majority of time required for preparation of the simulation. The flow boundary conditions are enforced exactly and one is concerned with various errors associated with spatial and temporal discretization of the field equations. Complications occur when geometry of the flow domain changes as a function of time, e.g., when one deals with the moving boundary problems. In the present work we are interested in finding a spectrally-accurate and computationally efficient solution to such problem while maintaining a sharp resolution of the location of the moving boundary.

Techniques developed for handling of the moving boundary problems have been reviewed in [1] with updates given in [2]. Such techniques can be classified as Eulerian, Lagrangian and mixed. Eulerian algorithms, which are of interest in the present work, rely on a coordinate system that is either stationary in a laboratory frame of reference or moves in a prescribed manner (i.e., describable by the Galilean transformation). These

[1] A version of this chapter has been published as –

Husain, S.Z., and Floryan, J.M., Gridless spectral algorithm for Stokes flow with moving boundaries, *Computer Methods in Applied Mechanics and Engineering*, vol. 198, pp. 245-259 (2008).

algorithms can be divided for convenience into fixed grid methods, adaptive grid methods and various mapping methods.

The adaptive grid methods adjust the grid at each time step so that one of the grid lines follows the moving boundary. The adjustment is done numerically through appropriate mappings. The process is conceptually identical regardless of whether one uses numerical grid generation combined with finite-difference discretization of the field equations or a grid generation scheme for the finite-element discretization of the same equations. These methods have high computational overhead as the grid needs to be reconstructed at each time step followed by solution of the field equations. In the case of the problem discussed in [3] and solved using finite volume discretization, the cost of grid construction reached the level of about 75% of the total cost of the computation. The boundary conditions are imposed exactly and thus the overall error includes contributions from the grid generation and the spatial and temporal discretizations of the field equations. Numerous problems occur when one is interested in high accuracy as this requires both high accuracy in grid generation and high accuracy discretization.

One can reduce the cost of computations and improve accuracy by using analytical transformations that map the irregular flow domain into a regular computational domain at the cost of increased complexity of the field equations (see [4] for an example). Such mappings are available for a limited class of geometries [1].

In the fixed grid methods the boundary of the flow domain is allowed to move through a fixed grid and this eliminates the high computational cost of grid re-adjustment. Various methods for modeling of movements of boundaries based either on the surface or volume tracking procedures are discussed in [1,5]. In the former approach a set of points is introduced to mark location of the boundary which is represented as a set of interpolated curves. These points are moved in a prescribed manner during the solution process [5,6] and provide ability for precise identification of boundary location. In the latter approach the information about the boundary location is not stored but the boundary is reconstructed whenever necessary on the basis of the presence of certain quantity of a convenient marker within computational cell, e.g., MAC - Marker and Cell [7], VOF - Volume of Fluid [2, 8] and Level Set [9, 10] methods. The reconstruction process leads to a diffused location of the boundary but the overall accuracy can be made consistent with the low accuracy discretization schemes used for the field equations.

Lagrangian methods are characterized by a coordinate system that moves with the fluid. Each computational cell always contains the same fluid and its tracking requires solution of an initial value problem. These methods are well suited for moving boundary problems as they permit simple delineation of moving boundaries. The two main problems involve mesh tangling and loss of numerical accuracy associated with highly distorted meshes. Possible remedies are discussed in [1]. Mixed Lagrangian-Eulerian methods rely on the combination of concepts described above [1].

The available methods have low order accuracy and thus one is interested in the development of techniques that could overcome this limitation. The overall error is affected by the accuracy of representation of boundary location and by the accuracy associated with spatial discretization of the field equations. Spectral methods provide lowest error for the field equations but are limited to solution domains with regular geometries. The variability and complexity of geometry of the flow domain represents the main challenge for implementation of these methods, however, the use of the concept of immersed boundary conditions provides a way to combine both, i.e., the fixed, regular solution domain with a complex, time dependent flow domain [11]. The immersed boundary conditions concept has been proposed in [12] in the context of simulation of cardiac dynamics. Boundary conditions at the edges of the physical domain are replaced by constraints imposed inside the computational domain but these constraints have been constructed using physical arguments through introduction of forcing functions that reproduce the effect of the boundary [13]. In this sense the method is analogous to the fixed grid methods discussed above. The first spectrally accurate implementation for fixed boundary problems has been given in [11] with the constraints constructed in a formal manner by imposing conditions for elimination of certain terms in the spectral expansions representing flow boundary conditions. This implementation is limited to geometries that can be represented by Fourier expansions but results in a gridless algorithm as all possible variations of boundary geometries are described in terms of the Fourier coefficients only. The programming effort associated with modeling of changes of geometry has been essentially removed as the only information required for specifying the new geometry is reduced to a set of Fourier coefficients provided as input to the code. This implementation has been extended to hydrodynamics stability problems [14] and applied successfully in the analysis of the effect of surface roughness [15].

This chapter is focused on the development of spectrally-accurate algorithms suitable for solution of time-dependent flow problems, including moving boundary problems. Such algorithms are of interest in the development of active flow control and management techniques using micro-electro-mechanical devices. As our interest is in flows through micro/nano channels, we focus our attention on the small Reynolds number limit, i.e., Stokes flow. Simpler problems, i.e., unsteady conduction problems in a corrugated channels have been considered earlier in [16, 17] without encountering numerical instabilities. The model problem for the present work is described in Section 3.2. Spatial and temporal discretizations are discussed in Section 3.3. Results of numerical tests are discussed in Section 3.4. Section 3.5 provides a short summary of the main conclusions.

3.2. Model problem

The model problem consists of an unsteady Stokes flow in a channel bounded by corrugated walls with geometry of the corrugation changing as a function of time (see Fig. 3.1). These geometries as well as motions of the walls are described by the following relations

$$y_L(x,t) = -1 + \sum_{n=-\infty}^{n=+\infty} H_L^{(n)}(t)\, e^{in\alpha x}, \qquad y_U(x,t) = 1 + \sum_{n=-\infty}^{n=+\infty} H_U^{(n)}(t) e^{in\alpha x} \qquad (3.2.1a,b)$$

where $H_L^{(n)} = H_L^{(-n)*}$ and $H_U^{(n)} = H_U^{(-n)*}$ are known and stars denote complex conjugates. The channel geometry is periodic in x with wavelength λ=2π/α and extends to ±∞ in the x-direction.

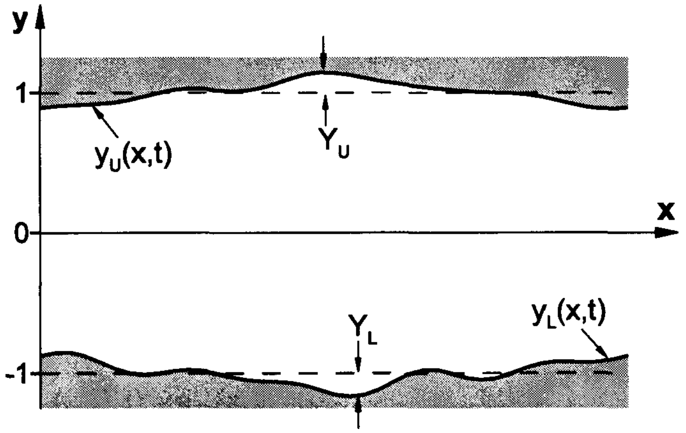

Figure 3.1. *Sketch of the instantaneous form of the flow domain.*

The dimensionless field equation has the form

$$\frac{\partial}{\partial t}\left(\nabla^2\Psi\right)=\nabla^2\left(\nabla^2\Psi\right). \qquad (3.2.2a)$$

where Ψ denotes the stream function, which is defined as

$$u(x,y,t) = u_0(y) + u_1(x,y,t) = d\Psi_0/dy + \partial\Psi/\partial y = \partial\Psi_T/\partial y, \qquad (3.2.2b)$$

$$v(x,y,t) = v_1(x,y,t) = -\partial\Psi/\partial x = -\partial\Psi_T/\partial x \qquad (3.2.2c)$$

and $\nabla^2 = \partial^2/\partial x^2 + \partial^2/\partial y^2$. Here u(x,y,t) and v(x,y,t) denote the total velocities in x- and y-directions, respectively, $u_1(x,y,t)$ and $v_1(x,y,t)$ denote velocity modifications due to the presence of boundary motion, the Poiseuille flow $u_0(y)=1-y^2$ is taken as the reference flow, $\Psi_0=-y^3/3+y+2/3$ denotes the stream function of this flow and Ψ_T stand for the stream function of the complete flow (total stream function). The problem formulation needs to be supplemented with suitable initial conditions, which are taken to be in the form

$$u(x,y,0) = u_i(x,y),\ \ v(x,y,0) = v_i(x,y),\ \ y_L(x,0)=y_{Li}(x),\ \ y_U(x,0)=y_{Ui}(x), \qquad (3.2.3a\text{-}d)$$

where $u_i(x,y)$, $v_i(x,y)$, $y_{Li}(x)$, $y_{Ui}(x)$ are considered to be known, and boundary conditions at the solid walls, which are taken to be in the form

$$u_0(y_L(x,t)) + u_1(x, y_L(x,t), t) = u_L(x,t) = 0, \qquad (3.2.4a)$$

$$u_0(y_U(x,t)) + u_1(x, y_U(x,t), t) = u_U(x,t) = 0, \qquad (3.2.4b)$$

$$v_1(x, y_L(x,t), t) = v_L(x,t) = dy_L/dt = \sum_{n=-\infty}^{n=+\infty} \frac{dH_L^{(n)}}{dt} e^{in\alpha x}, \qquad (3.2.4c)$$

$$v_1(x, y_U(x,t), t) = v_U(x,t) = dy_U/dt = \sum_{n=-\infty}^{n=+\infty} \frac{dH_U^{(n)}}{dt} e^{in\alpha x}. \qquad (3.2.4d)$$

3.3. Discretization method

We are interested in the determination of solution of (3.2.2)-(3.2.4) with spectral accuracy. The main difficulty associated with the implementation of spectral discretization arises due to the irregularity and time-dependence of the solution domain. In order to overcome this problem, we select fixed rectangular computational domain extending over one period in the x-direction and extending sufficiently far in the y-direction so that the flow domain remains always immersed inside the computational domain during the time interval of interest. If we denote the locations of extremities in the shape of the walls as Y_U and Y_L, the y-extent of the computational domain is set as (-1-Y_L,1+Y_U) without loss of generality.

The spatial discretization is based on the use of Fourier expansions in the x-direction due to periodicity of the geometry, and on expansions in terms of Chebyshev polynomials in the y-direction. We shall use standard definition of the Chebyshev polynomials and thus the y-extent of the computational domain needs to be mapped onto (-1,1) (see Fig. 3.1) before calculations can proceed. The required mapping has the form

$$\hat{y} = [y - (1 + Y_U)]\,\Gamma + 1 \tag{3.3.1}$$

where $\hat{y} \in \langle -1, 1 \rangle$, $\Gamma = 2/(2+Y_U+Y_L)$ is a constant and the governing equation transforms into

$$\frac{\partial}{\partial t}\left[\frac{\partial^2}{\partial x^2} + \Gamma^2 \frac{\partial^2}{\partial \hat{y}^2}\right]\Psi = \left[\frac{\partial^4}{\partial x^4} + 2\Gamma^2 \frac{\partial^2}{\partial x^2 \partial \hat{y}^2} + \Gamma^4 \frac{\partial^4}{\partial \hat{y}^4}\right]\Psi . \tag{3.3.2}$$

Locations of the walls in the $(x, \hat{y})$ plane are given as

$$\hat{y}_L(x,t) = \sum_{n=-\infty}^{n=+\infty} A_L^{(n)}(t) e^{in\alpha x}, \qquad \hat{y}_U(x,t) = \sum_{n=-\infty}^{n=+\infty} A_U^{(n)}(t) e^{in\alpha x}, \tag{3.3.3a,b}$$

where $A_L^{(0)}(t) = 1 + \Gamma\left[-2 - Y_U + H_L^{(0)}(t)\right]$, $A_L^{(n)}(t) = \Gamma H_L^{(n)}(t)$ for $n \neq 0$, $A_U^{(0)}(t) = 1 + \Gamma\left[-Y_U + H_U^{(0)}(t)\right]$, $A_U^{(n)}(t) = \Gamma H_U^{(n)}(t)$ for $n \neq 0$. The boundary conditions at the transformed boundaries become

$$u_0(\hat{y}_L(x,t)) + u_1(x, \hat{y}_L(x,t), t) = 0 , \tag{3.3.4a}$$

$$u_0(\hat{y}_U(x,t)) + u_1(x, \hat{y}_U(x,t), t) = 0 , \tag{3.3.4b}$$

$$v_1(x,\hat{y}_L(x,t),t)=v_L(x,t)=\Gamma^{-1}\,d\hat{y}_L/dt=\Gamma^{-1}\sum_{n=-\infty}^{n=+\infty}\frac{dA_L^{(n)}}{dt}e^{in\alpha x}\ , \tag{3.3.4c}$$

$$v_1(x,\hat{y}_U(x,t),t)=v_U(x,t)=\Gamma^{-1}\,d\hat{y}_U/dt=\Gamma^{-1}\sum_{n=-\infty}^{n=+\infty}\frac{dA_U^{(n)}}{dt}e^{in\alpha x} \tag{3.3.4d}$$

The solution can be represented in the form of Fourier expansion

$$\Psi(x,\hat{y},t)=\sum_{n=-\infty}^{n=+\infty}\Phi^{(n)}(\hat{y},t)e^{in\alpha x}\approx\sum_{n=-N_M}^{n=+N_M}\Phi^{(n)}(\hat{y},t)e^{in\alpha x} \tag{3.3.5}$$

where $\Phi^{(n)}(\hat{y},t)=\Phi^{(-n)^*}(\hat{y},t)$ and star denotes complex conjugate. Substitution of (3.3.5) into the field equation (3.3.2) and separation of Fourier components lead to an uncoupled system of partial differential equations for $\Phi^{(n)}$, $n\in\langle 0,N_M\rangle$, of the type

$$\frac{\partial}{\partial t}\left[\Gamma^2D^2-(n\alpha)^2\right]\Phi^{(n)}=\left[\Gamma^4D^4-2\Gamma^2(n\alpha)^2D^2+(n\alpha)^4\right]\Phi^{(n)} \tag{3.3.6}$$

where D=d/d$\hat{y}$. Two types of temporal discretizations have been used. The two-step implicit method results in the following relations

$$\begin{aligned}&\left[\Gamma^4D^4+\left(-2n^2\alpha^2\Gamma^2-1.5\Gamma^2\Delta t^{-1}\right)D^2+\left(n^4\alpha^4+1.5n^2\alpha^2\Delta t^{-1}\right)\right]\Phi^{(n)}_{\tau+1}=\\&-2\Delta t^{-1}\left[\Gamma^2D^2-(n\alpha)^2\right]\Phi^{(n)}_{\tau}+0.5\Delta t^{-1}\left[\Gamma^2D^2-(n\alpha)^2\right]\Phi^{(n)}_{\tau-1},\quad n\in\langle 0,N_M\rangle\end{aligned} \tag{3.3.7a}$$

while similar relations resulting from the one-step, self-starting implicit method is

$$\begin{aligned}&\left[\Gamma^4D^4+\left(-2(n\alpha)^2\Gamma^2-0.5\Gamma^2\Delta t^{-1}\right)D^2+\left((n\alpha)^4+0.5(n\alpha)^2\Delta t^{-1}\right)\right]\Phi^{(n)}_{\tau+1}=\\&\qquad-0.5\Delta t^{-1}\left[\Gamma^2D^2-(n\alpha)^2\right]\Phi^{(n)}_{\tau},\qquad n\in\langle 0,N_M\rangle\end{aligned}\ . \tag{3.3.7b}$$

In the above, the subscript τ labels the time step and Δt stands for the (constant) length of the time step. Relation (3.3.7a) has the form of an inhomogeneous ordinary differential equation for $\Phi^{(n)}_{\tau+1}$. The following discussion will be carried out in the context of the two-step method, while the relevant relations for the one-step method can be readily deduced.

The unknown function $\Phi^{(n)}_{\tau+1}$ can be represented in terms of expansions based on Chebyshev polynomials in the form

$$\Phi^{(n)}_{\tau+1}(\hat{y}) = \sum_{k=0}^{k=\infty} G^{(n)}_{k,\tau+1} T_k(\hat{y}) \approx \sum_{k=0}^{k=N_T} G^{(n)}_{k,\tau+1} T_k(\hat{y}) \tag{3.3.8}$$

where T_k denotes the Chebyshev polynomial of k^{th} order and $G^{(n)}_{k,\tau+1}$ denotes the unknown coefficients of the expansion. Substitution of (3.3.8) into (3.3.7a) gives

$$\begin{aligned}&\left[\Gamma^4 D^4 + \left(-2n^2\alpha^2\Gamma^2 - 1.5\Gamma^2\Delta t^{-1}\right) D^2 + \left(n^4\alpha^4 + 1.5n^2\alpha^2\Delta t^{-1}\right)\right] \sum_{k=0}^{k=N_T} G^{(n)}_{k,\tau+1} T_k = \\ &-2\Delta t^{-1}\left[\Gamma^2 D^2 - (n\alpha)^2\right] \sum_{k=0}^{k=N_T} G^{(n)}_{k,\tau} T_k + 0.5\Delta t^{-1}\left[\Gamma^2 D^2 - (n\alpha)^2\right] \sum_{k=0}^{k=N_T} G^{(n)}_{k,\tau-1} T_k\,.\end{aligned} \tag{3.3.9}$$

Galerkin procedure is used to develop algebraic equations for the unknowns $G^{(n)}_{k,\tau+1}$, i.e., we multiply both sides of (3.3.9) by $T_j(\hat{y})$ and integrate with the weight function $\hat{\omega} = 1/\sqrt{1-\hat{y}^2}$ to get

$$\begin{aligned}&\sum_{k=0}^{k=N_T} \left[\Gamma^4\left\langle T_j, D^4 T_k\right\rangle + \left(-2n^2\alpha^2\Gamma^2 - 1.5\Gamma^2\Delta t^{-1}\right)\left\langle T_j, D^2 T_k\right\rangle + \left(n^4\alpha^4 + 1.5n^2\alpha^2\Delta t^{-1}\right)\left\langle T_j, T_k\right\rangle\right] G^{(n)}_{k,\tau+1} \\ &\quad = \sum_{k=0}^{k=N_T} \left[\Gamma^2\left\langle T_j, D^2 T_k\right\rangle - (n\alpha)^2\left\langle T_j, T_k\right\rangle\right] \left[-2\Delta t^{-1} G^{(n)}_{k,\tau} + 0.5\Delta t^{-1} G^{(n)}_{k,\tau-1}\right] \qquad j \in \left\langle 0, N_T - 4\right\rangle\end{aligned} \tag{3.3.10}$$

where the inner product is defined as $\left\langle f_j(\hat{y}), g_k(\hat{y})\right\rangle = \int_{-1}^{1} f_j(\hat{y}) g_k(\hat{y}) \hat{\omega}(\hat{y}) d\hat{y}$. Equation (3.3.10) leads to N_T-3 decoupled algebraic equations for each Fourier mode. Four additional equations required in order to close the system need to be derived from the boundary conditions and these conditions provide coupling between different Fourier modes.

The boundary conditions are to be enforced along the lines $\hat{y}_L(x,\tau+1)$ and $\hat{y}_U(x,\tau+1)$ that are inside the computational domain while the solution domain remains fixed at $\hat{y} \in \langle -1,1 \rangle$. This can be accomplished using the concept of immersed boundary conditions. We begin description of the implementation of boundary conditions by noting that at time τ+1 one needs to evaluate velocity components $u_f(x,\tau+1) \equiv u(x, f(x,\tau+1),\tau+1)$ and $v_f(x,\tau+1) \equiv v(x, f(x,\tau+1),\tau+1)$ along an arbitrary time dependent line l that at time t = τ+1 occupies position $\hat{y} = f(x,\tau+1)$, such that f is a periodic function with period $\lambda = 2\pi/\alpha$ and $|f(x,\tau+1)| \leq 1$. The function $f(x,\tau+1)$ can be expressed without loss of generality as

$$f(x,\tau+1) = \sum_{n=-\infty}^{n=-\infty} P_{\tau+1}^{(n)} e^{in\alpha x} \approx \sum_{n=-N_A}^{n=+N_A} P_{\tau+1}^{(n)} e^{in\alpha x} \qquad (3.3.11)$$

where in the calculations the shape of the wall is approximated by the finite number of terms N_A . The velocity components $u_f(x,\tau+1)$ and $v_f(x,\tau+1)$ are periodic in x with the same period λ and thus can be expressed in terms of Fourier series as

$$u_f(x,\tau+1) \equiv u(x, f(x,\tau+1),\tau+1) = \sum_{n=-N_\theta}^{n=+N_\theta} U_{\tau+1}^{(n)} e^{in\alpha x},$$

$$v_f(x,\tau+1) \equiv v(x, f(x,\tau+1),\tau+1) = \sum_{n=-N_\theta}^{n=+N_\theta} V_{\tau+1}^{(n)} e^{in\alpha x} . \qquad (3.3.12a,b)$$

It will become obvious from the follow up discussion that the summation extends to $N_\theta=N_TN_A+N_M$. When $f(x,\tau+1)$ overlaps with the position of the wall, u_l and v_l are known and the coefficients in the above expansions can be determined. Since the flow representation used in the computations is limited to N_M+1 modes (see Eq. 3.3.5), only on the first (N_M+1) terms in (3.3.12) can be accounted for. We shall now discuss the method used to enforce these conditions.

Velocity components u_l and v_l can be evaluated along the wall at time $\tau+1$ using the discretized form of the solution, i.e.,

$$\begin{aligned} u_l(x,\tau+1) &= u_0(f(x,\tau+1)) + \Gamma \sum_{n=-N_M}^{n=+N_M} D\Phi^{(n)}(f(x,\tau+1),\tau+1)e^{in\alpha x} \\ &= u_0(f(x,\tau+1)) + \Gamma \sum_{n=-N_M}^{n=+N_M} \sum_{k=0}^{k=N_T} G^{(n)}_{k,\tau+1} DT_k(f(x,\tau+1))\, e^{in\alpha x} \ , \end{aligned} \tag{3.3.13a}$$

$$\begin{aligned} v_l(x,\tau+1) &= -\sum_{n=-N_M}^{n=+N_M} i\,n\,\alpha\,\Phi^{(n)}(f(x,\tau+1),\tau+1)\, e^{in\alpha x} \\ &= -\sum_{n=-N_M}^{n=+N_M} \sum_{k=0}^{k=N_T} i\,n\,\alpha\, G^{(n)}_{k,\tau+1} T_k(f(x,\tau+1))\, e^{in\alpha x} \ . \end{aligned} \tag{3.3.13b}$$

Chebyshev polynomials and their derivatives evaluated at the wall, i.e., $T_k(f(x,\tau+1))$ and $DT_k(f(x,\tau+1))$, are periodic functions of x and thus can be expressed in terms of Fourier expansion as follows

$$T_k(f(x,\tau+1)) = \sum_{m=-N_s}^{m=+N_s} w^{(m)}_{k,\tau+1} e^{im\alpha x} \ , \quad DT_k(f(x,\tau+1)) = \sum_{m=-N_s}^{m=+N_s} d^{(m)}_{k,\tau+1} e^{im\alpha x} \tag{3.3.14a,b}$$

Where $\max(N_s)=N_TN_A$ and the method for evaluation of coefficients $w^{(m)}_{k,\tau+1}$ and $d^{(m)}_{k,\tau+1}$ is explained in Appendix A. Substitution of (3.3.14) into (3.3.13) gives

$$u_1(x,\tau+1) = \sum_{n=-N_F}^{n=+N_F} F^{(n)}(\tau+1)e^{in\alpha x} + \Gamma \sum_{n=-N_\theta}^{n=+N_\theta} \sum_{m=-N_M}^{m=+N_M} \sum_{k=0}^{k=N_T} G^{(m)}_{k,\tau+1} d^{(n-m)}_{k,\tau+1} e^{in\alpha x} \quad , \tag{3.3.15a}$$

$$v_1(x,\tau+1) = -\sum_{n=-N_\theta}^{n=+N_\theta} \sum_{m=-N_M}^{m=+N_M} \sum_{k=0}^{k=N_T} i\, m\, \alpha\, G^{(m)}_{k,\tau+1} w^{(n-m)}_{k,\tau+1}\, e^{in\alpha x}$$

where

$$u_0(f(x,\tau+1)) = \sum_{n=-N_F}^{n=+N_F} F^{(n)}(\tau+1)e^{in\alpha x} \text{ where } N_F < N_M . \tag{3.3.16}$$

Comparison of (3.3.12) with (3.3.15) gives

$$U^{(n)}_{\tau+1} = F^{(n)}(\tau+1) + \Gamma \sum_{m=-N_M}^{m=+N_M} \sum_{k=0}^{k=N_T} G^{(m)}_{k,\tau+1} d^{(n-m)}_{k,\tau+1} \quad , \quad V^{(n)}_{\tau+1} = -\sum_{m=-N_M}^{m=+N_M} \sum_{k=0}^{k=N_T} i\, m\, \alpha\, G^{(m)}_{k,\tau+1} d^{(n-m)}_{k,\tau+1} \tag{3.3.17a,b}$$

The reader may note that $V^{(0)}_{\tau+1}$ is not independent but results from specification of $U^{(n)}_{\tau+1}$ (see Appendix B). Equations (3.3.17) can be used to express boundary conditions along the lower and upper walls, i.e., for at $\hat{y}_L(x,\tau+1)$ and $\hat{y}_U(x,\tau+1)$. In the case of our model problem the boundary conditions along the lower wall take following form

$$\sum_{m=-N_M}^{m=+N_M} \sum_{k=0}^{k=N_T} G^{(m)}_{k,\tau+1} (d_L)^{(n-m)}_{k,\tau+1} = -\Gamma^{-1} F_L^{\ (n)}(\tau+1), \qquad |n| \geq 0 \tag{3.3.18a}$$

$$\sum_{m=-N_M}^{m=+N_M} \sum_{k=0}^{k=N_T} i\, m\, \alpha\, G^{(m)}_{k,\tau+1} (w_L)^{(n-m)}_{k,\tau+1} = -\Gamma^{-1} \left(\frac{dA_L^{(n)}}{dt} \right)_{\tau+1} \quad , \qquad |n| \geq 1 \tag{3.3.18b}$$

and are enforced for $|n|\leq N_m$. Relations obtained for $|n|>N_m$ can be used as a measure of error in the enforcement of flow boundary conditions. Similar boundary conditions can be written for the upper wall by replacing subscript L with subscript U.

The above problem specification is incomplete due to the shortage of boundary conditions for the mode zero in Eq.(3.3.18b). While these conditions can be selected arbitrarily, we shall focus our attention on the fixed mass flow rate case, i.e., we shall require that the net mass flow rate in the x-direction is maintained constant during motion of the walls.

Volume flux Q along the channel can be evaluated by integrating the x-velocity component across the channel, i.e.,

$$Q(x,\tau+1)=\int_{\hat{y}_L}^{\hat{y}_U}\left(\frac{\partial\Psi_T}{\partial\hat{y}}\right)_{\tau+1}d\hat{y}=\Psi_T(x,\hat{y}_U(x,\tau+1),\tau+1)-\Psi_T(x,\hat{y}_L(x,\tau+1),\tau+1)\,. \quad (3.3.19)$$

The volume flux represents an x-periodic function that can be written in the form of a Fourier expansion

$$Q(x,\tau+1)=\sum_{n=-N_M}^{n=+N_M}Q^{(n)}(\tau+1)e^{in\alpha x} \quad (3.3.20)$$

where the zero term, i.e., $Q^{(0)}$, represents the net mass flux along the channel. Evaluation of this flux requires knowledge of Ψ_T at both walls. The evaluation process is very similar for both walls and thus we shall limit description to the lower wall only.

Values of Ψ_T at the lower wall can be evaluated by considering velocities of material points located on the line *l* overlapping with this wall. These velocities are known and can be expressed as

$$u_l(x,\tau+1)=0\,, \tag{3.3.21a}$$

$$v_l(x,\tau+1)=\frac{d\hat{y}_L(x,\tau+1)}{dt}\frac{dy}{d\hat{y}}=\Gamma^{-1}\sum_{n=-N_A,\,n\neq0}^{k=+N_A}\left(\frac{dA_L^{(n)}}{dt}\right)_{\tau+1}e^{in\alpha x}\,. \tag{3.3.21b}$$

The Fourier expansion on the right hand side of (3.3.21b) does not contain mode zero as the mean position of the wall is assumed to be independent of time. The rate of change of Ψ_T along the wall can be written as

$$\frac{d\Psi_T}{dx}(x,\hat{y}_L(x,\tau+1))=\frac{\partial\Psi_T}{\partial x}(x,\hat{y}_L(x,\tau+1))+\Gamma\frac{\partial\Psi_T}{\partial\hat{y}}(x,\hat{y}_L(x,\tau+1))\frac{d\hat{y}_L}{dx}\,. \tag{3.3.22}$$

The first and second terms of the right hand side are replaced with (3.3.21b) and (3.3.21a), respectively, and the resulting expression is integrated in x resulting in

$$\Psi_T(x,\hat{y}_L(x,\tau+1))=-\sum_{n=-N_A,\,n\neq0}^{n=+N_A}(in\alpha\Gamma)^{-1}\left(\frac{dA_L^{(n)}}{dt}\right)_{\tau+1}e^{in\alpha x}+C_L(\tau+1) \tag{3.3.23}$$

where C_L is an arbitrary function of time. An analogous expression written for the upper wall introduces another arbitrary function of time, i.e., C_U. Substitution of (3.3.23) and an equivalent relation for the upper wall into Eq.(3.3.19) and extraction of mode zero results in

$$C_U(\tau+1)=Q^{(0)}(\tau+1)+C_L(\tau+1)\,. \tag{3.3.24}$$

The value of $Q^{(0)}(\tau+1)$ is assumed in this analysis to be known and independent of time, and equal to the flow rate of the reference flow, i.e., $Q^{(0)}=\frac{4}{3}$.

One of the functions C_U and C_L can be selected arbitrarily and the other one follows from (3.3.24). In the description given below the latter one has been selected arbitrarily by introducing condition $\Psi_T=0$ at a conveniently selected point x_0 at the lower wall resulting in

$$C_L(\tau+1)=\Gamma^{-1}\sum_{n=-N_A,n\neq 0}^{n=+N_A}(in\alpha)^{-1}\left(\frac{dA_L^{(n)}}{dt}\right)_{\tau+1}e^{in\alpha x_0}. \tag{3.3.25}$$

The computationally useful form of (3.3.24)-(3.3.25) requires introduction of Ψ as this is the unknown in our problem formulation (see Eq. 3.2.2; $\Psi=\Psi_T-\Psi_0$). Values of Ψ_0 evaluated along the lower wall represent a known function of t and x, periodic in x, that can be expressed as

$$\Psi_0(\hat{y}_L(x,\tau+1))=\sum_{n=-N_M}^{n=+N_M}\left(\Theta_L^{(n)}\right)_{\tau+1}e^{in\alpha x} \tag{3.3.26}$$

with a similar expression for the upper wall. Values of Ψ along the lower wall can be computed from (3.3.19), (3.3.23-3.3.26) as

$$\begin{aligned}\Psi(x,\hat{y}_L(x,\tau+1),\tau+1)=&-\sum_{n=-N_M,n\neq 0}^{n=+N_M}(in\alpha\Gamma)^{-1}\left(\frac{dA_L^{(n)}}{dt}\right)_{\tau+1}e^{in\alpha x}-\\&\sum_{n=-N_M}^{n=+N_M}\left(\Theta_L\right)_{\tau+1}^{(n)}e^{in\alpha x}+\sum_{n=-N_M,n\neq 0}^{n=+N_M}(in\alpha\Gamma)^{-1}\left(\frac{dA_L^{(n)}}{dt}\right)_{\tau+1}e^{in\alpha x_0}.\end{aligned} \tag{3.3.27a}$$

and for the upper wall as

$$\begin{aligned}\Psi(x,\hat{y}_U(x,\tau+1),\tau+1)=&-\sum_{n=-N_M,n\neq 0}^{n=+N_M}(in\alpha\Gamma)^{-1}\left(\frac{dA_U^{(n)}}{dt}\right)_{\tau+1}e^{in\alpha x}\\&-\sum_{n=-N_M}^{n=+N_M}\left(\Theta_U\right)_{\tau+1}^{(n)}e^{in\alpha x}+\sum_{n=-N_M,n\neq 0}^{n=+N_M}(in\alpha\Gamma)^{-1}\left(\frac{dA_L^{(n)}}{dt}\right)_{\tau+1}e^{in\alpha x_0}+Q^{(0)}\end{aligned} \tag{3.3.27b}$$

Stream function Ψ at the lower wall can be expressed in terms of the Fourier expansion (3.3.5) and the Chebyshev expansion (3.3.8) in the form

$$\Psi(x, \hat{y}_L(x, \tau+1), \tau+1) = \sum_{n=-N_M}^{n=+N_M} \Phi_L^{(n)}(\hat{y}_L(x, \tau+1)) e^{in\alpha x} \tag{3.3.28}$$

where

$$\Phi_L^{(n)}(\hat{y}(x, \tau+1)) = \sum_{m=-N_M}^{m=+N_M} \sum_{k=0}^{k=N_T} G_{k,\tau+1}^{(m)} \left(w_{k,\tau+1}^{(n-m)} \right)_L . \tag{3.3.29}$$

Substitution of (3.3.28)-(3.3.29) and similar expressions for the upper wall into (3.3.27) results in the form of the closing conditions useful for numerical implementation, i.e.,

$$\sum_{m=-N_M}^{m=+N_M} \sum_{k=0}^{k=N_T} G_{k,\tau+1}^{(m)} \left(w_{k,\tau+1}^{(m)^*} \right)_L = -\Theta_L^{(0)} + \sum_{n=-N_M, n\neq 0}^{n=+N_M} (in\alpha\Gamma)^{-1} \left(\frac{dA_L^{(n)}}{dt} \right)_{\tau+1} e^{in\alpha x_0} , \tag{3.3.30a}$$

$$\sum_{m=-N_M}^{m=+N_M} \sum_{k=0}^{k=N_T} G_{k,\tau+1}^{(m)} \left(w_{k,\tau+1}^{(m)^*} \right)_U = -\Theta_U^{(0)} + \sum_{n=-N_M, n\neq 0}^{n=+N_M} (in\alpha\Gamma)^{-1} \left(\frac{dA_L^{(0)}}{dt} \right)_{\tau+1} e^{in\alpha x_0} + Q^{(0)} . \tag{3.3.30b}$$

Equations (3.3.10), (3.3.18) and (3.3.30) form a complete set of algebraic equations for the unknown coefficients $G_{k,\tau+1}^{(n)}$, $k = 0,\ldots,N_T$, $n=0,\ldots,N_M$. A solution of this system of equations moves calculations forward by one time step. Various methods of solutions will be discussed in the next section. Once the stream function has been determined, the velocity components can be computed from the definition of Ψ (see Eq. 3.2.2) while evaluation of pressure is discussed in Appendix C.

An alternative formulation frequently found in the literature [18] uses a constant pressure gradient constraint rather than the fixed mass flux constraint and the corresponding boundary conditions are discussed in Appendix D.

3.4. Testing of the algorithm

We shall discuss the performance of the algorithm in the context of two convenient test problems involving movements of boundaries, i.e., movements of the lower wall corresponding (i) to a traveling elastic wave and (ii) to a standing elastic wave.

3.4.1. Traveling elastic wave

3.4.1.1. Test problem

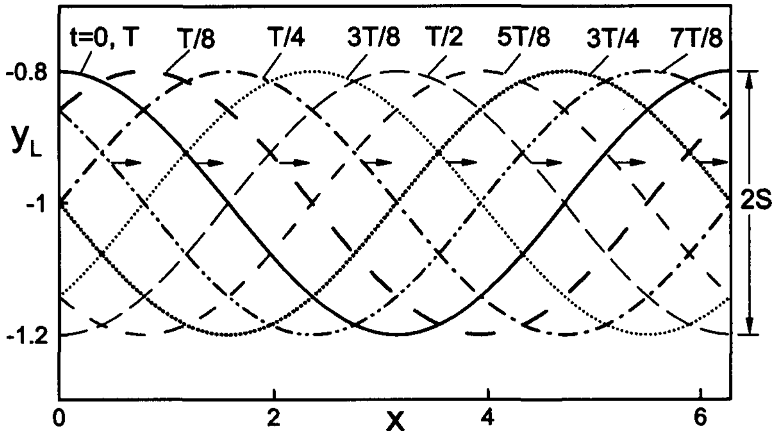

Figure 3.2. Shape of the lower wall deformed by elastic traveling wave described by Eq.(3.4.1b) with the amplitude S=0.2, the wave number α=1.0 and the phase speed c=π at t=0, T/8, T/4, 3T/8, T/2, 5T/8, 3T/4 and 7T/8, where T denotes one time period.

Consider an elastic wave traveling along the lower wall with the upper wall being flat. The shape of the resulting channel can be described as

$$y_L(x,t) = -1 + \sum_{n=-N_m,\, n\neq 0}^{n=+N_M} H_L^{(n)}\, e^{in\alpha(x-ct)}, \qquad y_U(x,t) = 1 \tag{3.4.1a}$$

and, in the simplest case of a sinusoidal wave, the shape of the lower wall becomes

$$y_L(x,t) = -1 + S\cos[\alpha(x - ct)] = -1 + (0.5 S e^{i\alpha(x-ct)} + CC) \qquad (3.4.1b)$$

where c denotes the phase speed, α denotes the wave number and S stands for the amplitude of the wave. Variations of the location of the lower wall as a function of time are illustrated for this particular case in Fig. 3.2.

Use of the Galilean transformation

$$X=x-ct \qquad (3.4.2)$$

transforms the time-dependent moving boundary problem into a time-independent fixed boundary problem. The full problem in the moving frame of reference (X,y) takes the form

$$c\left[\frac{\partial^3}{\partial X^3} + \frac{\partial^3}{\partial X \partial y^2}\right]\Psi + \left[\frac{\partial^4}{\partial X^4} + 2\frac{\partial^2}{\partial X^2 \partial y^2} + \frac{\partial^4}{\partial y^4}\right]\Psi = 0 \qquad (3.4.3)$$

with boundary conditions in the form

$$u(X,+1) = 0,\ v(X,+1) = 0,\ u(X, y_L(X)) = 0,\quad v(y_L(X)) = -c \sum_{n=-N_M, n\neq 0}^{n=+N_M} i n \alpha H_L^{(n)} e^{in\alpha x}\ . \qquad (3.4.4)$$

Elastic wave propagation problem represents a good test problem as it can be solved as a steady fixed-boundary problem in the moving reference frame and an unsteady moving-boundary problem in the fixed reference frame, and both solutions can be compared. The former one, i.e., (3.4.3)-(3.4.4), provides testing opportunity for the analysis of accuracy of spatial discretization and, especially, accuracy of enforcement of boundary conditions, and the latter one provides opportunity for testing of accuracy of temporal discretization. The former problem is solved using the steady version of the method discussed in the previous section.

3.4.1.2. Solution in the moving frame of reference

Problem (3.4.3)-(3.4.4) represents steady fixed boundary problem. As the first step, we wish to demonstrate the spectral accuracy of the spatial discretization used in the present work. While this discretization is fairly standard, one needs to pay special attention to the zone around the moving wall where the concept of immersed boundary conditions is used to impose flow boundary conditions due to possible problems associated with the formation of boundary layers in the distribution of modal functions. The Chebyshev expansions (3.3.8) with coefficients calculated using Galerkin procedure (3.3.10) are guaranteed to be spectrally accurate with the increasing number of terms N_T. In most cases sixty Chebyshev polynomials provide machine accuracy. When $\alpha \to \infty$ (corrugation with shorter wavelength) and higher Fourier modes begin to play a role, one needs to increase the number of Chebyshev polynomials in order to resolve wall boundary layers. These layers become extremely thin for larger values of α and for higher Fourier modes (see Fig. 3.3). Modal functions change very rapidly inside these layers while they are nearly zero in the rest of the domain. Typically one needs to use $N_T \approx 80$ for $\alpha=20$ and $N_T \approx 160$ for $\alpha=50$ in order to provide the required resolution.

The second aspect of spectral accuracy involves convergence of the truncated Fourier series (3.3.5) describing x-variations of the unknown. In all tests dealing with this issue the number of Chebyshev polynomials N_T was kept sufficiently large in order to reduce the associated error to machine accuracy. Chebyshev norm defined as

$$\left\|D\Phi^{(n)}\right\|_{\hat{\omega}} = \sqrt{\Gamma^2 \int_{-1}^{1} D\Phi^{(n)}(\hat{y},t) D\Phi^{(n)*}(\hat{y},t)\hat{\omega}(\hat{y})d\hat{y}} \quad , \quad \hat{\omega} = 1/\sqrt{1-\hat{y}^2} \tag{3.4.5}$$

had been adopted as a measure of the “magnitude” of the derivative of the modal function $\Phi^{(n)}$. Results displayed in Fig. 3.4 demonstrate that this norm decreases as a function of the mode number n with the rate of decrease very rapidly reaching the (asymptotic) exponential form.

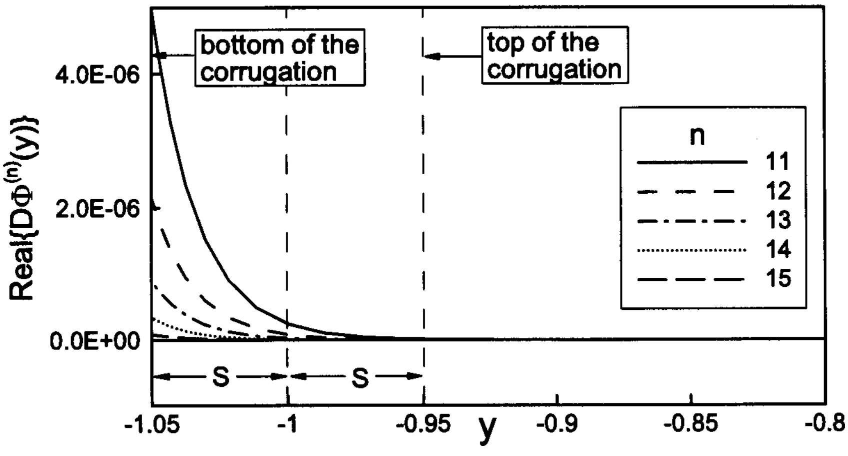

Figure 3.3. Distribution of the real part of $D\Phi^{(n)}$ as a function of y for the higher modes (n>10) in the vicinity of the lower wall for the model problem (3.4.3)-(3.4.4) for α=5 and S=0.05. N_M=15 Fourier modes and N_T=80 Chebyshev polynomials used in the computations.

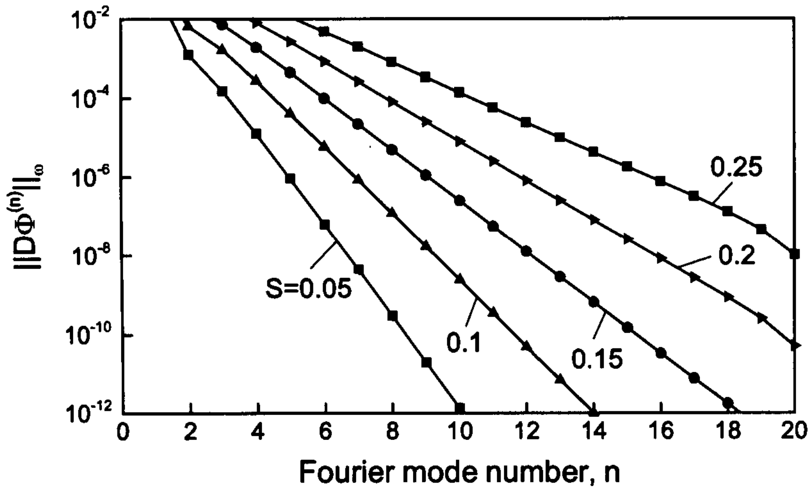

Figure 3.4. Variations of the Chebyshev norm of $D\Phi^{(n)}$ (see Eq. 3.4.5) as a function of the Fourier mode number n for the model problem (3.4.3)-(3.4.4) for different wave amplitudes S for α=1.0. N_M=20 Fourier modes and N_T=60 Chebyshev polynomials used in the computations.

Error in the enforcement of flow boundary conditions is of special interest. For convenience, we adopt the L_∞ norm for u- and v-velocity components evaluated at the lower wall as quantitative measures of this error. These norms are defined as

$$\left\|u_{er}(X)\right\|_{\infty} = \sup_{0\le X\le 2\pi/\alpha} \left|u_{er}(X)\right| , \quad \left\|v_{er}(X)\right\|_{\infty} = \sup_{0\le X\le 2\pi/\alpha} \left|v_{er}(X)\right| \tag{3.4.6a}$$

where

$$u_{er}(X) = u(X, y_L(X)) , \quad v_{er}(X) = v(X, y_L(X)) - v_L(X) \tag{3.4.6b}$$

and their distributions as functions of S and α are illustrated in Figs 3.5-3.6. The reader may note in judging these results that S=2 corresponds to a situation when the upper most point of the lower wall comes into contact with the upper wall.

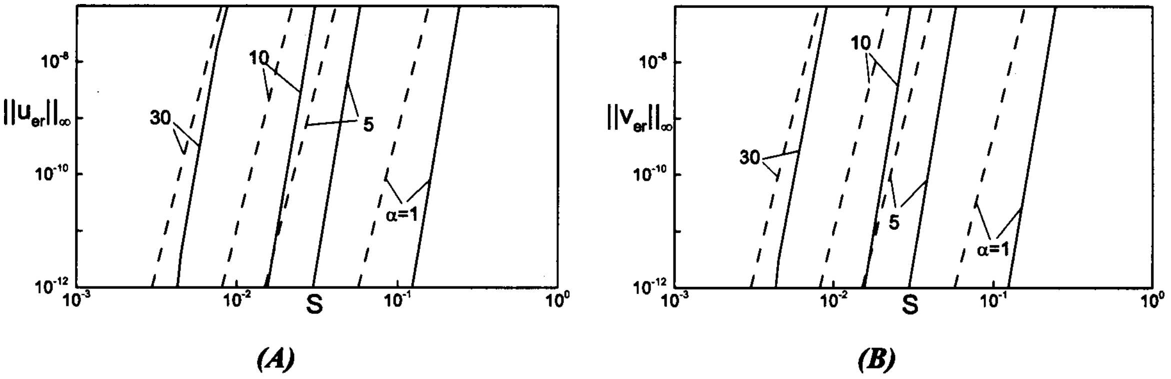

Figure 3.5. *Variations of the $\left\|u_{er}(X)\right\|_{\infty}$ (Fig. 3.5A) and $\left\|v_{er}(X)\right\|_{\infty}$ (Fig. 3.5B) norms (see Eq. 3.4.6a) as a function of the wave amplitude S for selected values of the wave number α for the model problem (3.4.3)-(3.4.4) with the phase speed $c=\pi$. The dashed and solid lines correspond to results obtained with the N_M = 10, 15 Fourier modes, respectively. The reader may note that S=2 corresponds to peak of the wave reaching the top wall. N_T=60 Chebyshev polynomials were used in the calculations.*

The available results suggest that the error is at machine accuracy level if α and S are below certain critical values. Once these values are reached, the error begins to increase rapidly in a fairly universal manner. The critical values of α and S can be increased by increasing the number of Fourier modes N_M used in the calculation, but the qualitative character of the error increment remains unchanged. The location of the maximum error overlaps with the location of the lowest point in the lower wall, as illustrated by distribution of error along the lower boundary displayed in Fig. 3.7.

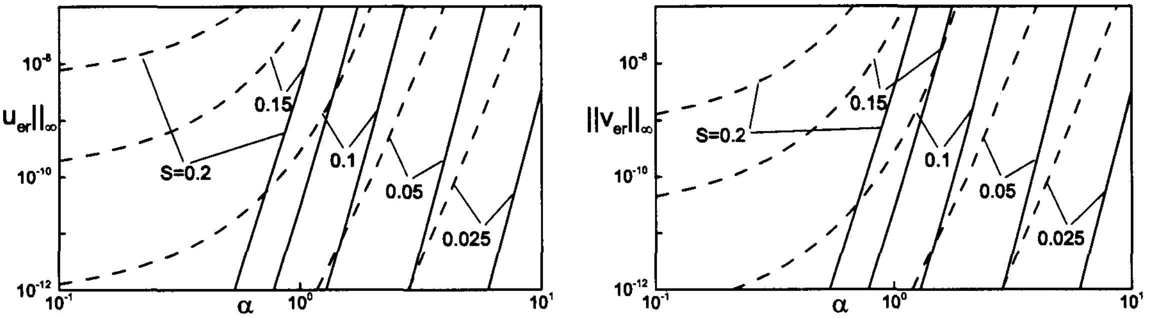

(A)

(B)

Figure 3.6. *Variations of the $\|u_{er}(X)\|_\infty$ (Fig. 3.6A) and $\|v_{er}(X)\|_\infty$ (Fig. 3.6B) norms (see Eq. 3.4.6a) as a function of the wave number α for selected values of the wave amplitude S for the model problem (3.4.3)-(3.4.4) for the phase speed $c=\pi$. Other parameters as in Fig. 3.5.*

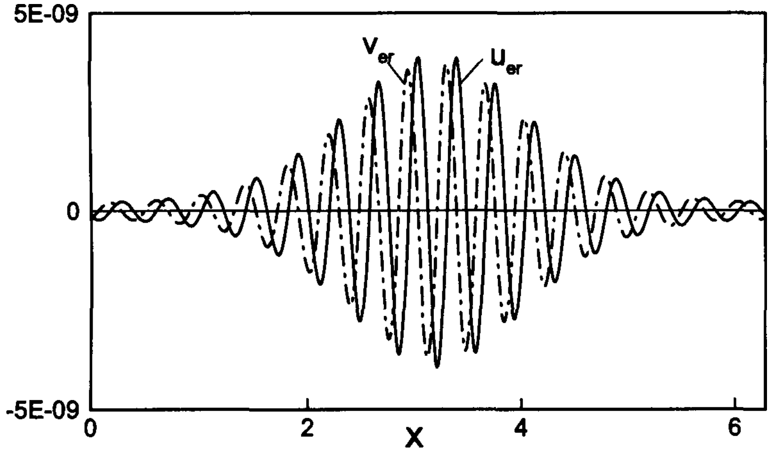

Figure 3.7. *Distribution of error u_{er} and v_{er} (see Eq. 3.4.6b) in the enforcement of flow boundary conditions at the lower wall for the model problem (3.4.3)-(3.4.4) with the $c=\pi$, $S=0.2$ and $\alpha=1$. The presented results were obtained with $N_M=15$ and $N_T=60$.*

3.4.1.3. Solution in the fixed frame of reference

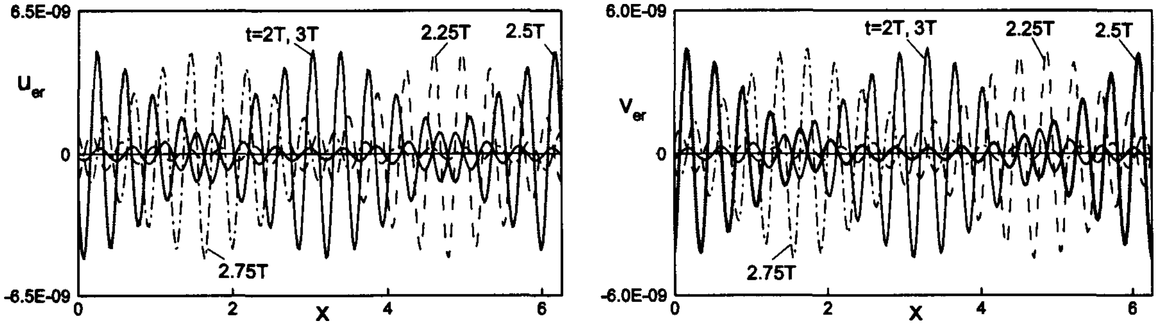

(A) *(B)*

Figure 3.8. *Distribution of error in the enforcement of flow boundary condition u_{er} (Fig. 3.8A) and v_{er} (Fig. 3.8B) for the u- and v-velocity components (see Eq. 3.4.6b), respectively, at the lower wall at t = 2T, 2.25T, 2.5T, 2.75T and 3T, where T stand for one time period, for the model problem (3.4.3)-(3.4.4) with the amplitude S=0.2, the wave number α=1.0 and the phase speed $c=\pi$. The presented results were obtained through a direct solution of the moving boundary problem in the fixed coordinates system with N_M=15 Fourier modes and N_T=60 Chebyshev polynomials. Solution corresponding to the fixed boundary problem in the moving frame of reference (3.4.3)-(3.4.4) was used as the initial condition.*

The problem discussed in the previous section becomes a moving boundary problem when expressed in a fixed reference frame. We use solution obtained in the moving frame of reference as an initial condition and track evolution of the flow as a function of time. The time history of the error of enforcement of boundary conditions is illustrated in Fig. 3.8. It can be seen that the maximum error is similar to that found in the case of solution obtained in the moving frame of reference, location of this error follows location of the maximum opening of the slot as it moves in the x-direction, and the magnitude of this error remains approximately constant when several waves pass through the computational box.

Variations of the velocity components in selected test points are displayed in Fig. 3.9. The results shown in the figure demonstrate (i) the periodic variations in time with the expected period and (ii) the phase differences between different x-locations that match phase differences determined using solution in the moving frame of reference. Distribution of shear stress at the moving boundary displayed in Fig. 3.10 demonstrates that the expected periodicity and phase shifts have been reproduced. Results of the temporal grid convergence studies displayed in Fig. 3.11 demonstrate that the one-step and two-steps algorithms reproduce the expected first- and second-order accuracy in time, respectively.

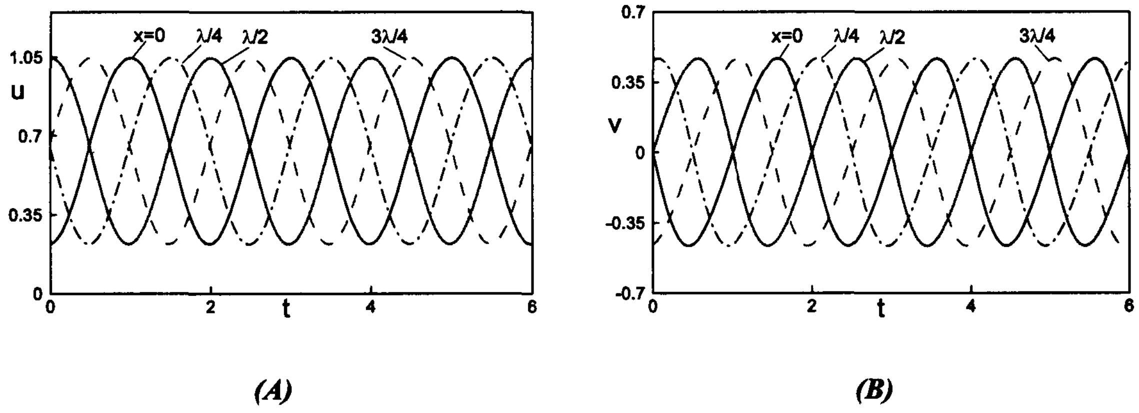

Figure 3.9. *Variations of the u-velocity (Fig. 3.9A) and v-velocity (Fig. 3.9B) components for three time periods at points (x,y) = (0, -0.6), (λ/4, -0.6), (λ/2, -0.6), (3λ/4, -0.6), λ=2π/α, for the model problem (3.4.3)-(3.4.4) solved directly as a moving boundary problem in the fixed reference frame. Solution corresponding to the fixed boundary problem in the moving frame of reference (3.4.3)-(3.4.4) was used as the initial condition.* N_M*=15 Fourier modes and* N_T*=60 Chebyshev polynomials were used in the computations. Other conditions as in Fig. 3.2.*

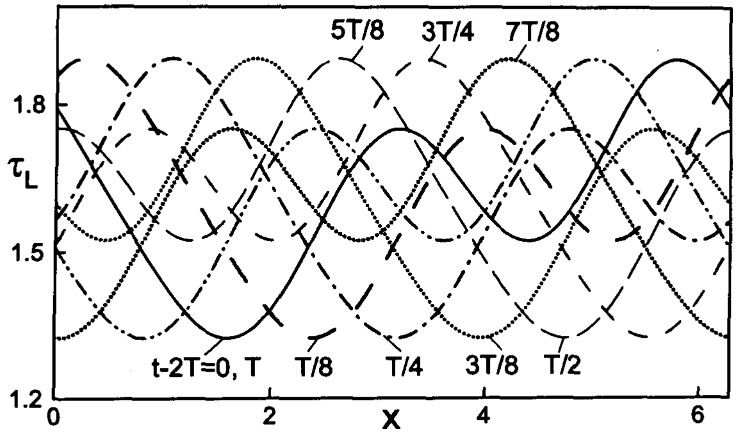

***Figure 3.10.** Distribution of the wall shear stress at different time levels after two time periods for the model problem (3.4.3)-(3.4.4). Other parameters are as in Figs 3.2 and 3.9.*

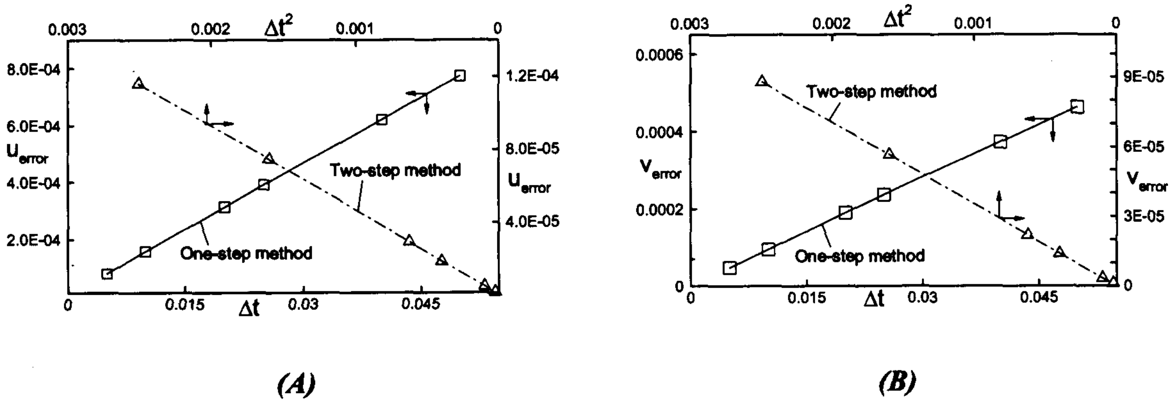

***Figure 3.11.** Variations of error in the u- (Fig. 3.11A) and v- (Fig. 3.11B) velocity components as a function of the step size Δt used in the temporal discretization in the case of the model problem (3.4.3)-(3.4.4) with the amplitude S=0.1, the wave number α=1.0 and the phase speed c=π. The error is defined as the maximum of the absolute value of the difference between the results obtained through the direct solution of the moving boundary problem in the fixed frame of reference and the corresponding fixed boundary problem in the moving frame of reference at a time corresponding to t=1.0. N_M=10 Fourier modes and N_T=60 Chebyshev polynomials were used in the computations. Solution of the model problem (3.4.3)-(3.4.4) in the moving frame of reference is taken as the initial condition for the direct solution method.*

3.4.2. Standing elastic wave

3.4.2.1. Test problem

Consider standing elastic wave at the lower wall with the upper wall being flat. The shape of the resulting channel can be described as

$$y_L(x,t) = -1 + \sum_{n=-N_M, n\neq 0}^{n=+N_M} H_L^{(n)}(t)\, e^{in\alpha x}, \qquad y_U(x,t) = 1 \tag{3.4.7}$$

and, in the simplest case of a sinusoidal wave, the shape of the lower wall becomes

$$y_L(x,t) = -1 + S\cos(\omega t)\cos(\alpha x) = -1 + (0.5\, S\cos(\omega t)\, e^{i\alpha x} + CC) \tag{3.4.8}$$

where α denotes the wave number, S stands for the amplitude and ω denotes the frequency of the wave. Variations of the location of the lower wall as a function of time are illustrated for this particular case in Fig. 3.12.

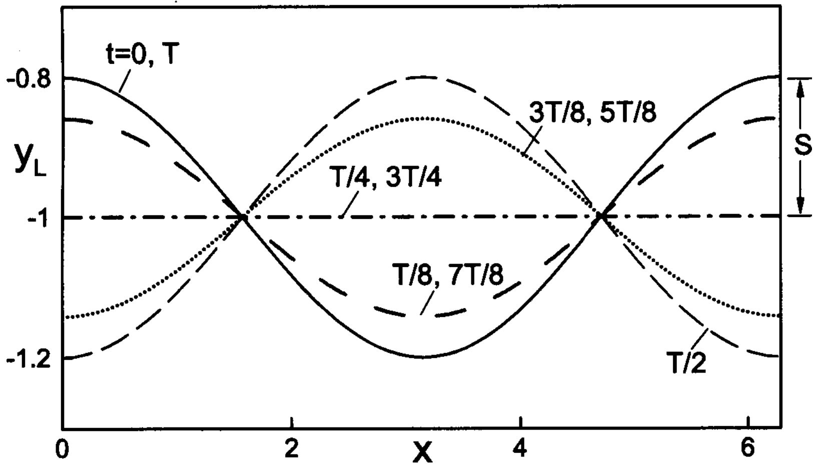

Figure 3.12. Shape of the lower wall modified by elastic standing wave with the wave number α=1.0, the amplitude S=0.2 and the frequency ω=π at times t=0, T/8, T/4, 3T/8, T/2, 5T/8, 3T/4, 7T/8 and T, where T denotes one time period.

The full test problem has the form

$$\frac{\partial}{\partial t}\left[\frac{\partial^2}{\partial x^2}+\frac{\partial^2}{\partial y^2}\right]\Psi=\left[\frac{\partial^4}{\partial x^4}+\frac{\partial^2}{\partial x^2 \partial y^2}+\frac{\partial^4}{\partial y^4}\right]\Psi \qquad (3.4.9)$$

with boundary conditions in the form

$$u(x,+1,t)=0\,,\quad v(x,+1,t)=0\,,$$

$$u(x,y_L(x),t)=0,\quad v(x,y_L(x,t),t)=\sum_{n=-N_M,n\neq 0}^{n=+N_M}\frac{d}{dt}\left(H_L^{(n)}(t)\right)e^{in\alpha x} \qquad (3.4.10)$$

For convenience, we use the L_∞ norm as a quantitative measure of error associated with the enforcement of velocity boundary conditions at the lower wall, i.e.,

$$\left\|u_{er}(x,t)\right\|_\infty=\sup_{0\leq X\leq 2\pi/\alpha}\left|u_{er}(x,t)\right|\ ,\quad \left\|v_{er}(x,t)\right\|_\infty=\sup_{0\leq X\leq 2\pi/\alpha}\left|v_{er}(x,t)\right| \qquad (3.4.11a)$$

where

$$u_{er}(x,t)=u(x,y_L(x,t),t)\ ,\quad v_{er}(x,t)=v(x,y_L(x,t),t)\text{-}v_L(x,t)). \qquad (3.4.11b)$$

3.4.2.2. Solution of the test problem

Figure 3.13 illustrates distribution of error in the enforcement of boundary conditions at the lower wall. It can be seen that the magnitude of the error changes periodically in time with frequency equal to double the frequency of the standing wave. Variations in the magnitude of the error can be correlated with variations of the shape of the wall, i.e., the maximum of error occurs at times when the channel opening is the largest. The magnitude of error can be reduced by increasing the number of Fourier modes used in the calculations but the qualitative behaviour of error with time remains unchanged.

The spatial distribution of error is illustrated in Fig. 3.14 after 3 and 3.5 cycles of the wave motion. It can be seen that the maximum of error shifts to location corresponding to the maximum opening of the channel. The Fourier spectra of the error shown in Fig. 3.15 demonstrate that the N_M number of Fourier modes have been eliminated according to the construction of the immersed boundary conditions algorithm described in Section 3.3. The largest error is associated with the first Fourier mode omitted in the enforcement of boundary conditions. The error associated with the higher omitted Fourier modes rapidly decays as the mode number increases.

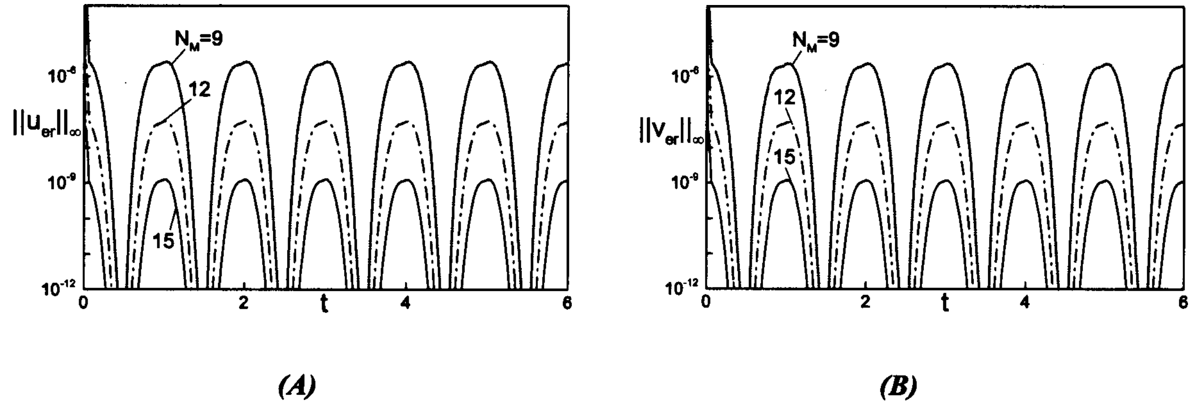

Figure 3.13. *Variations of the $\|u_{er}(x,t)\|_\infty$ (Fig. 3.13A) and $\|v_{er}(x,t)\|_\infty$ (Fig. 3.13B) norms (see Eq. 3.4.11a) as a function of time over three time periods for the moving boundary problem defined by (3.4.8)-(3.4.10) for α=1, S=0.2 and ω=π (shape of the wall is illustrated in Fig. 3.12) computed using N_T=60 and different values of N_M. The initial conditions used correspond to shape of the wall given by Eq. (3.4.8) at time t=0 and zero flow modifications. It can be seen that the initial transient dies out and the time-periodic flow response begins to dominate after 1-2 periods.*

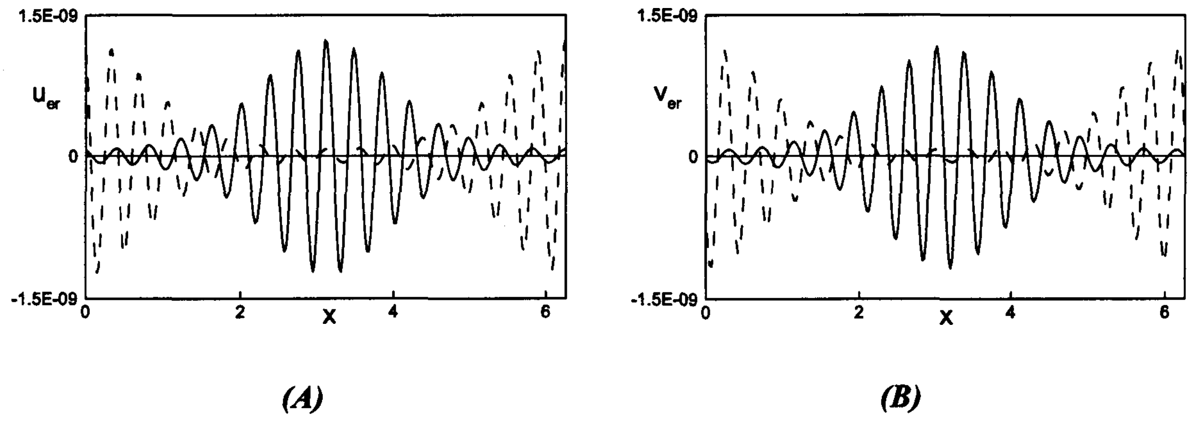

Figure 3.14. *Distribution of the error u_{er} (Fig. 3.14A) and v_{er} (Fig. 3.14B) in the u- and v-velocity components (see Eq. 3.4.11b) at the lower wall after three (solid line) and three and half time periods (dashed line) for the model problem (3.4.8)-(3.4.10) evaluated with N_M=15 Fourier modes. All other conditions are as in Figure 3.13.*

Figure 3.15 also displays results of tests carried out in order to check if the method produces any spurious spatial oscillations. Three cases were considered, i.e., in case (A) the wave was represented by the principal Fourier mode and the calculations had been carried out with N_M=9 Fourier modes, in case (B) the wave was represented by the second Fourier mode (the principal mode has the wave number α=0.5), and in case (C) the wave was represented by the third Fourier mode (the principal mode has the wave number α=1/3). In order to have fully equivalent representations, the number of Fourier modes used in cases (B) and (C) were N_M=18 and N_M=27, respectively. The selected representations admitted subharmonics of the 1/2 type in case (B) and 1/3 type in case (C). The Fourier spectra shown in Fig. 3.15 demonstrate the equivalency of the results in all three cases. No subharmonics had been produced during the solution process and the modes expected to produce zero contributions in cases (B) and (C) behaved as expected.

Results of temporal grid convergence studies are displayed in Fig. 3.16 and demonstrate that the one-step and two-steps algorithms reproduce the expected first- and second-order accuracy in time, respectively. Variations of velocity components at a test point displayed in Fig. 3.17 demonstrate the expected periodic variations in time.

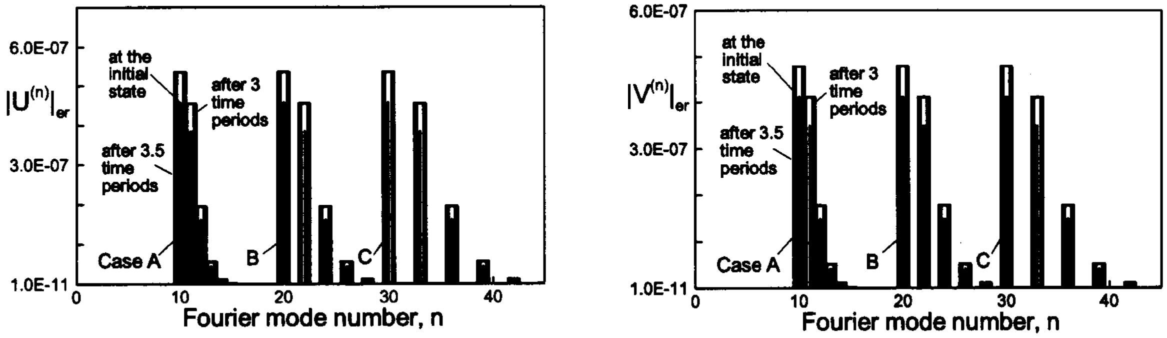

(A) ***(B)***

Figure 3.15. *Fourier spectra of error distributions u_{er} and v_{er} (see Eq. 3.4.11b) in the u- (Fig. 3.15A) and v- (Fig. 3.15B) velocity components at the lower wall for the model problem (4.8)-(4.10). Three different forms of Fourier expansions were considered, i.e., case A: α=1.0, N_M=9 ; case B: α=0.5, N_M=18 and case C: α=1/3, N_M=27. N_T=60 Chebyshev polynomials used in all cases. All other conditions as in Fig. 3.13.*

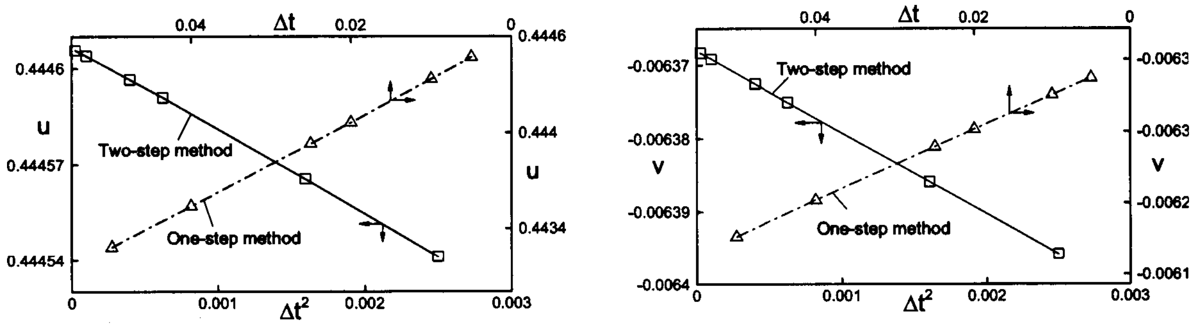

(A) ***(B)***

Figure 3.16. *Variations of the u- (Fig. 3.16A) and v- (Fig. 3.16B) velocity components as a function of the step size Δt used in the temporal discretization at a test point (x,y)=(π/2, -0.75) in the case of the model problem (3.4.8)-(3.4.10) with the amplitude S=0.1, the wave number α=1.0 and the frequency ω=π at time t=1.0. The initial conditions correspond to the solution of the fixed boundary problem for the wall shape given by Eq.(3.4.8) at t=0. N_M=10 Fourier modes and N_T=60 Chebyshev polynomials were used in the computations.*

Variations of the shear stress at the moving wall are displayed in Fig. 3.18 and also follow the expected periodic variations in time. The instantaneous streamlines associated with a standing wave with a more complex form are displayed in Fig. 3.19 in order to illustrate the algorithm's ability to deal with more complex motions.

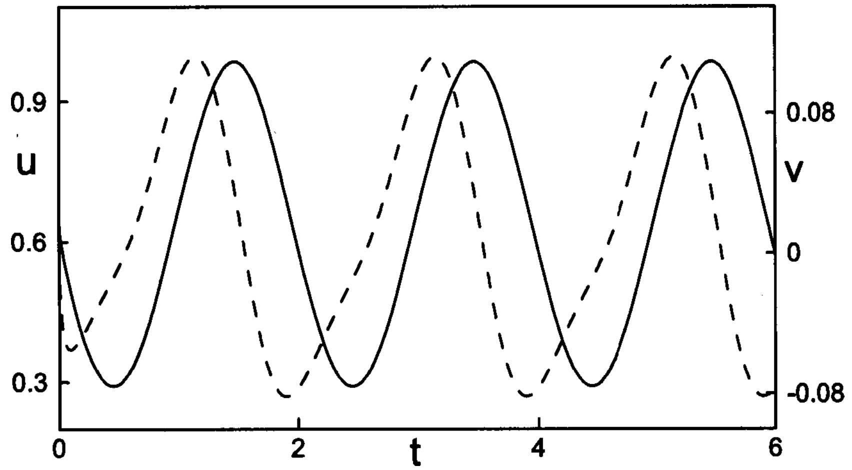

***Figure 3.17.** The evolution of the u- (solid line) and v- (dashed line) velocity components at a test point (x,y)=(λ /4,-0.6) during the first four time periods for the model problem (3.4.8)-(3.4.10) evaluated with N_M=15 Fourier modes. All other conditions are as in Figure 3.13.*

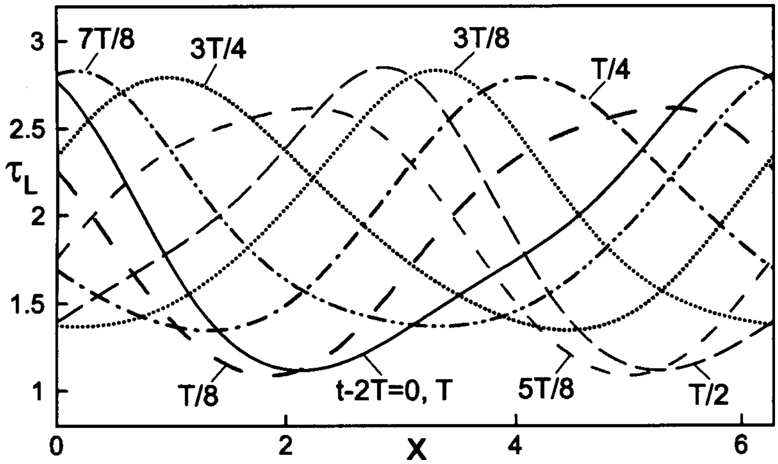

***Figure 3.18.** Distribution of the wall shear stress at different time levels during the third time period. The results shown were determined using N_M=15 Fourier modes. All other conditions are as in Figure 3.13.*

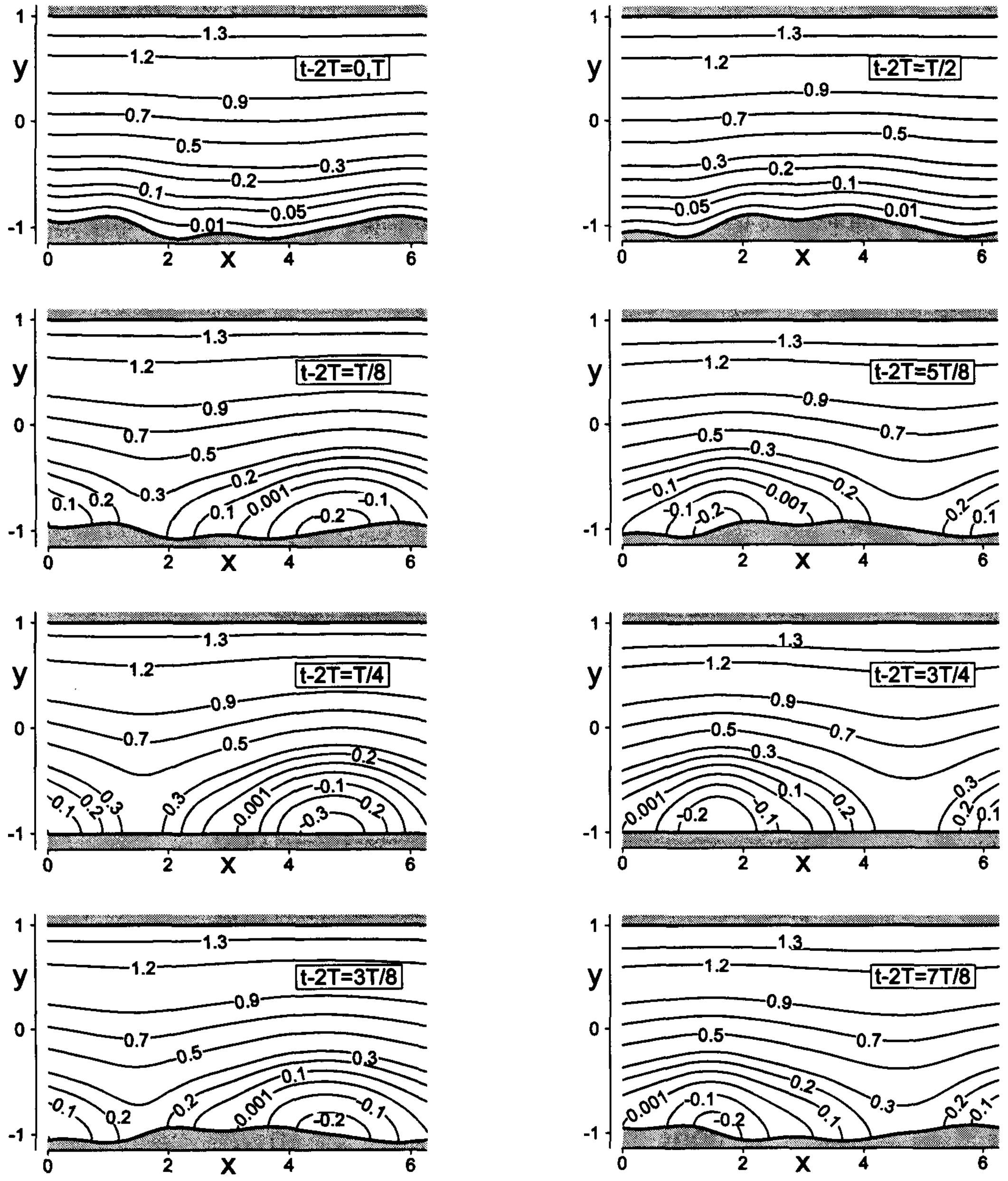

Figure 3.19. *Instantaneous streamlines in a channel bounded by $y_L(x,t)=-1+(0.05ie^{ix}-0.0167ie^{3ix}+0.0125ie^{4ix}+CC)\cos(\omega t)$ and $y_U(x,t)=1$, for $\omega=\pi$ using $N_M=25$ and $N_T=80$ evaluated after two time periods. Results are shown at times t-2T=0, T/8, T/4, 3T/8, T/2, 5T/8, 3T/4, 7T/8 and T, where T stands for one time period. The initial conditions used correspond to shape of the walls at time t=0 i.e. $y_L(x,0)=-1+(0.05ie^{ix}-0.0167ie^{3ix}+0.0125ie^{4ix}+CC)$ and $y_U(x,0)=1$, and zero flow modifications.*

3.4.3. Efficiency of the algorithm

The proposed algorithm requires solution of a system of linear algebraic equations resulting from the discretization of the field equations and boundary conditions at each time step. The resulting matrix structure is displayed in Fig. 3.20 and underscores the fact that algebraic equations resulting from discretization of each modal equation of type (3.3.7a) are uncoupled, i.e., the corresponding coefficients form blocks in the upper triangular form. The only coupling between Fourier modes is provided through the boundary conditions, i.e., the corresponding entries form horizontal lines in the matrix (four lines per block).

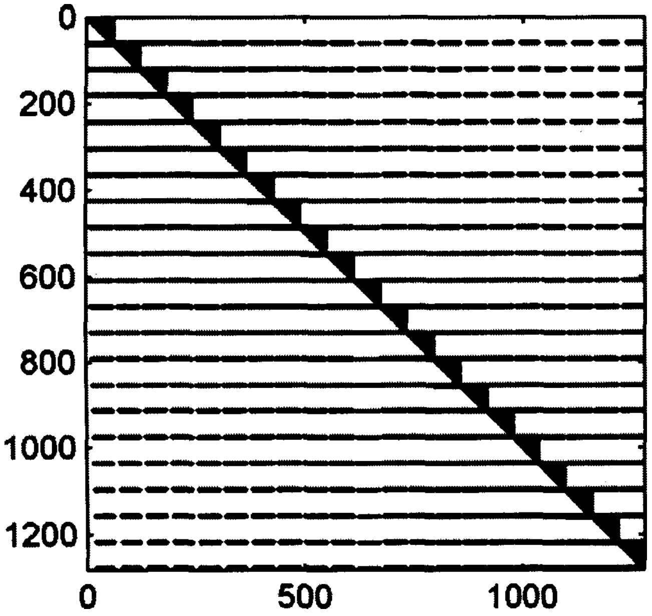

Figure 3.20. Structure of the coefficient matrix for the test problem (3.4.8)-(3.4.10) obtained with N_M=10 and N_T=60. Non-zero entries are marked in black.

Direct solution of the matrix equation leads to a solution method that we shall refer to as the ‘direct algorithm’. The efficiency of this algorithm is very good as the only matrix entries that have to be recomputed at each time step correspond to the boundary conditions. In addition, the shape of the moving wall can be easily adjusted by changing the magnitude of the relevant Fourier coefficients. In this sense, the proposed algorithm is superior with respects to algorithms based on dynamic grid adjustments and/or mapping methods as the cost of re-gridding and matrix construction have been eliminated, and comparable to algorithms based on various forms of interface tracking while delivering much higher accuracy.

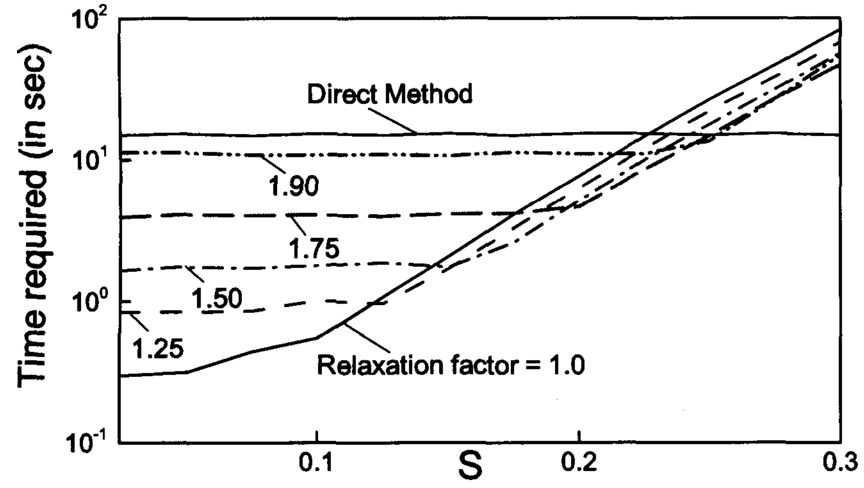

Figure 3.21. Performance of the first version of the decoupled algorithm with different values of the over-relaxation factor for the model problem (3.4.3)-(3.4.4) as a function of the amplitude S of the traveling wave with the wave number $\alpha=1.0$ and the phase speed $c=\pi$. Time required by the direct method is given for reference. All calculations have been carried out with $N_M=15$ Fourier modes and $N_T=60$ Chebyshev polynomials.

The matrix of coefficients can be very large when a large number of Fourier modes are required and this motivates the search for a method of solution that avoids construction as well as inversion of the complete matrix. Structure of the matrix (see Fig. 3.20) suggests the use of an iterative solution algorithm based on the decoupling of Fourier modes. We have tested four versions of such algorithms which we shall refer to as the 'decoupled algorithms'.

In the first version, the unknowns corresponding to a Fourier mode of interest in equation (3.3.18) and (3.3.37) at the current time step are expressed in terms of the remaining

Fourier modes using their values from the previous time step (or from the previous iteration). The solution process begins with mode 0, proceeds to the next mode using the most recent information available and continues until the last mode N_M is reached, and then it is repeated until a convergence criterion is satisfied. In this way, the inversion of the complete matrix of size $(N_T+1)*(2N_M+1)$ is replaced by a repetitive solution of system of (N_T+1) equations for each Fourier mode.

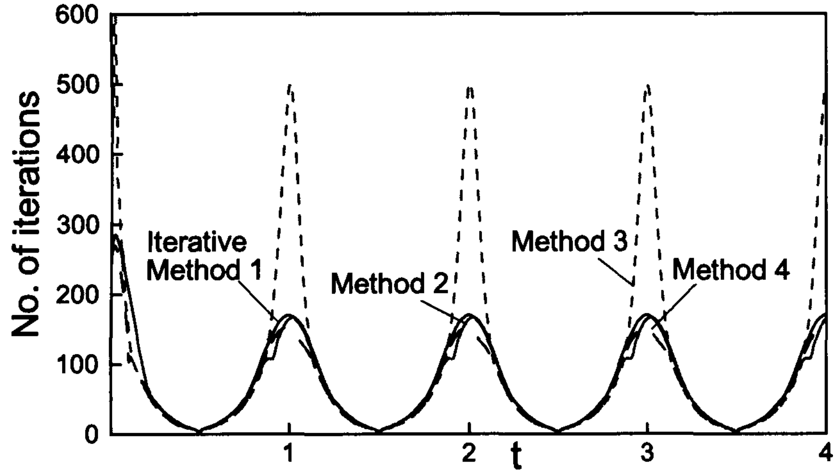

Figure 3.22. Number of iterations required by different versions of the decoupled algorithm as a function of the simulation time (and thus position of the wall). Simulations have been carried out over two periods of motion of the standing wave described in Section 3.4.2 with the wave amplitude $S=0.15$, the wave number $\alpha=1.0$ and the frequency $\omega=\pi$ using zero initial condition, $N_M=15$ Fourier modes and $N_T=60$ Chebyshev polynomials.

Versions 2-4 retain different couplings between the main modes as this might accelerate convergence. In version 2 we solve for each mode simultaneously with mode 0, e.g., we solve a system of equations for modes 0 and 1, then for modes 0 and 2, and then for modes 0 and 3, and so on. In version 3 we solve for each mode simultaneously with mode 1, i.e., mode 0 and 1, then 1 and 2, followed by 1 and 3, and so on. In the forth version, we solve for modes 0, 1 and 2 together and then separately for each of the remaining modes. It is necessary to point out that the decoupled algorithms reduce memory requirements as one needs to work with many small matrices rather then one very large matrix as well as they open possibility for parallelization of the computations. This issue becomes significant in the case of three-dimensional problems and large number of Fourier modes and Chebyshev polynomials.

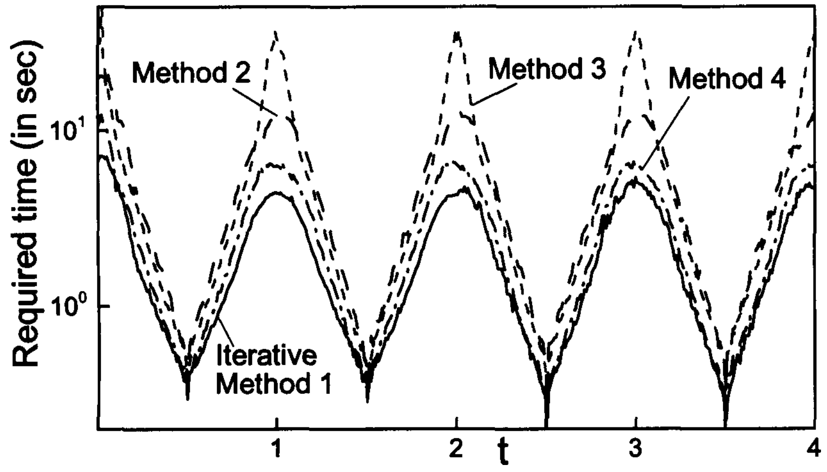

Figure 3.23. Variations of time (in sec) required to achieve convergence using different versions of the decoupled algorithm as a function of the simulation time (and thus position of the wall). All the other conditions as in Fig. 3.22.

The rates of convergence of all versions of the decoupled algorithm are generally very good; they decrease with an increase of the amplitude S and the wave number α characterizing the moving boundary. Their efficiency is illustrated in Fig. 3.21 in the context of the test problem discussed in Section 3.4.1 solved in the moving reference frame. It can be seen that the iterative method (version 1) requires less time than the direct method as long as the amplitude S is less than ~0.23. Over-relaxation decreases the efficiency of the method for S<~0.23 but improves efficiency for higher amplitudes S. The relative efficiency of different versions is illustrated in Figs 3.22 and 3.23 in the context of the test problem discussed in Section 3.4.2. Figure 3.21 displays variations in the number of iterations required for convergence as a function of simulation time. The maxima in the number of iterations correspond to instants of time when the channel opening passes through the maximum and minima correspond to times when the channel becomes flat. Figure 3.23 displays analogous information but expressed in terms of the computing time required for convergence. The local maxima correspond to instants of time when the channel opening passes through the maximum and minima correspond to times when the channel becomes flat. It can be seen that version 1 of the decoupled algorithm is most efficient as inclusion of additional coupling between Fourier modes increase number of iterations and time required for convergence.

3.5. Conclusions

A gridless algorithm for unsteady flow problems described by the biharmonic operator (Stokes flow) has been presented and tested. The algorithm uses a fixed computational domain with the flow domain completely immersed inside the computational domain. The flow boundary conditions are imposed using the concept of immersed boundary conditions. Two versions of boundary condition had been presented, i.e., corresponding to the fixed mass flux constraint and to the fixed pressure gradient constraint. The algorithm is suitable for the flow domains that have form of a channel whose geometry is periodic in the stream-wise direction. The opening of the channel may change as a function of time in an arbitrary manner but resulting in an instantaneous geometry that is Fourier transformable. The algorithm uses Fourier expansions for the spatial discretization in the flow direction, Chebyshev expansions for the discretization in the transverse direction and the first- and second-order implicit temporal discretizations. Various tests confirm the spectral accuracy of the spatial discretization and the theoretically predicted accuracy of the temporal discretization. The algorithm is very efficient as the part of the coefficient matrix corresponding to the field equations needs to be computed only once and the only changes required at each time step are limited to entries corresponding to the boundary conditions. In addition, the algorithm is very flexible as far as adaptation to different geometries is concerned as the only changes required are limited to changes in the Fourier coefficients describing motions of the walls. The numerical error associated with treatment of flow boundary conditions is well controlled during the simulation process. No numerical instabilities have been observed. Direct and decoupled versions of the algorithm had been explored. It had been found that while the direct algorithm is more efficient in situations when large-amplitude motions of the boundaries are of interest, a simple mode-decoupled algorithm is significantly faster when the interest is limited to small amplitude motions.

3.6. References

[1] Floryan, J.M. and Rasmussen, H., Numerical analysis of viscous flows with free surfaces, *Appl. Mech. Rev.*, vol. 42, pp. 323-341 (1989).

[2] Scardovelli, R. and Zaleski, S., Direct numerical simulation of free surface and interfacial flow, *Annu Rev. Fluid Mech.*, vol. 31, pp. 567-603 (1999).

[3] Inculet, I., Floryan, J.M. and Haywood, R., Dynamics of water droplets break-up in electric fields, *IEEE Transactions on Industry Applications*, vol. 28, pp. 1203-1209 (1992).

[4] Hamed, M. and Floryan, J.M., Numerical simulation of unsteady nonisothermal capillary interfaces, *J. Comp. Phys.* vol. 145, pp. 110-140 (1998).

[5] Hyman, J.M., Numerical methods for tracking of interfaces, *Physica,* vol. 12D, pp. 396-407 (1984).

[6] Glimm, J., Grove, J.W., Li, X.L., Shyue, K.M., Zeng, Y. and Zhang, Q., Three-dimensional front tracking, *SIAM J. Sci. Computing,* vol. 19, pp. 703-727 (1998).

[7] Harlow, F.H. and Welch, J.E., Numerical study of large amplitude free surface motions, *Phys. Fluids*, vol. 9, pp. 842-851 (1966).

[8] Hirt, C.W. and Nichols, B.D., Volume of fluid (VOF) method for the dynamics of free boundaries, *J. Comp. Phys.*, vol. 39, pp. 201-225 (1981).

[9] Osher, S.J. and Sethian, J.A., Fronts propagating with curvature dependent speed: Algorithms based on hamilton-jacobi formulations, *J. Comp .Phys.*, vol. 79, pp. 12-49 (1988).

[10] Sethian, J.A. and Smereka, P., Level set methods for fluid interfaces, Annu. *Rev. Fluid Mech.*, vol. 35, pp. 341-372 (2003).

[11] Szumbarski, J. and Floryan, J.M., A direct spectral method for determination of flows over corrugated boundaries, *J. Comp. Phys.*, vol. 153, pp. 378-402 (1999).

[12] Peskin, C.S., The fluid dynamics of heart valves: experimental, theoretical and computational methods, *Annu. Rev. Fluid Mech.,* vol. 14 pp. 235-59 (1982).

[13] Mittal, R. and Iaccarino, G., Immersed boundary methods, *Annu. Rev. Fluid Mech.,* vol. 37 pp. 239-261 (2005).

[14] Floryan, J.M., Centrifugal instability of Couette flow over a wavy wall, *Phys. Fluids*, vol. 14, pp. 312-322 (2002).

[15] Floryan, J.M., Three-dimensional instabilities of laminar flow in a rough channel and the concept of hydraulically smooth wall, *Eur. J. Mech. B/Fluids*, vol. 26, pp. 305-329 (2007).

[16] Husain, S.Z. and Floryan, J.M., Immersed boundary conditions method for unsteady flow problems described by the Laplace operator, *Int. J. Num. Meth. Fluids*, vol. 56, pp. 1765-1786 (2007).

[17] Husain, S.Z. and Floryan, J.M., Implicit spectrally-accurate method for moving boundary problems using immersed boundary conditions concept, *J. Comp. Phys.*, vol. 227, pp. 4459-4477 (2008).

[18] Floryan, J.M., Stability of wall-bounded shear layers in the presence of simulated distributed roughness, *J. Fluid Mech.*, vol. 335, pp. 29-55 (1997).

CHAPTER 4

Over-determined formulation of the IBC method[1]

4.1. Introduction

'Immersed boundary' (IB) methods refer to a class of methods where the computational domain extends beyond the physical domain resulting in edges of the physical domain immersed inside the computational domain. The name has been coined by Peskin [1] in the context of cardiac mechanics problems. The concept is very attractive as one can work with a fixed, regular computational domain regardless of the shape of the physical domain, i.e., the cost of generating boundary conforming grid has been completely eliminated. Field equations can be discretized using a simple reference coordinate system and are never changed regardless of the geometry of the physical domain. The main challenge associated with this method is the development of procedures that result in the enforcement of physical boundary conditions along the physical boundaries located inside of the computational domain. There are no conditions to be imposed along the edges of the computational domain (unless the edges of the physical and computational domains coincide) and thus the problem formulation needs to be closed by a set of constraints rather then by the classical boundary values. The IB method has been developed primarily in the context of fluid flow problems. The prevailing procedure for imposition of constraints replacing physical boundary conditions involves introduction of additional forcing that makes the fluid to move along the physical boundary. This methodology has roots in the physics of the problem, requires good understanding of the

[1] A version of this chapter has been accepted for publication as –

Husain, S.Z., Floryan, J.M. and Szumbarski, J., Over-Determined Formulation of the Immersed Boundary Conditions Method, *Computer Methods in Applied Mechanics and Engineering*, doi: 10.1016/j.cma.2009.09.022 (2009).

problem, and algorithm calibration involves elements of trial and error. Details of procedures based on the so-called continuous and discrete forcing are reviewed in [2, 3].

Fictitious domain methods [4, 5] offer an alternative approach for handling boundary irregularities where problems formulated on a complicated domain are solved on a simpler domain that contains the complicated domain. Use of simple domain enables efficient computational grid generation. The fictitious domain method is very suitable for moving boundary problems as it does not require regeneration of grid to account for the changing boundary geometries [5].

A separate group of methods has its roots in the methodology developed for handling the moving boundary problems and has been reviewed in [6]. Here one should focus on the fixed grid methods where the motion of the interface is tracked through a reference fixed grid. The most popular methods are based on the fluid fluxes and are known as the volume of the fluid (VOF) method. More recent methods rely on the concept of level set [7,8]. All these methods are of low-order in terms of spatial accuracy as they are based on the low-order finite-difference and/or finite-volume discretizations, and the interface tracking procedures result in smearing of the interface.

An alternative direction for handling boundary irregularities has been proposed by Szumbarski and Floryan [9] and is referred to as the immersed boundary conditions (IBC) method in the present work. The IBC method is conceptually similar to the IB methods as the physical field of interest is immersed inside the computational domain. However, unlike the IB method, the IBC method does not use additional forcing to impose the physical boundary conditions rather transforms the original boundary value problem into an internal value problem. The concept behind the IBC method is also different from the fictitious domain method as it does not simplify the geometry of the problem to enforce the boundary conditions [4]. The IBC method leads to a formal construction of boundary constraints that provide the required closing relations. Spatial discretization relies on the spectral expansions and thus provides ability to reach machine level accuracy. The boundary constraints rely on the representation of physical boundary in the spectral space and nullifying the relevant Fourier modes. Such implementation is limited to geometries that can be represented by Fourier expansions but results in a gridless algorithm as all possible variations of boundary geometries are described in terms of the Fourier coefficients only. The programming effort associated with modeling of changes of geometry has been essentially removed as the only information required for specifying the new geometry is reduced to a set of Fourier coefficients provided as input to the code. The additional attractiveness of this concept is associated with the precise mathematical formalism, high accuracy and sharp identification of the location of physical boundaries. This method has been successfully extended to unsteady problems [10] as well as moving boundary problems [11, 12] where the boundary geometries are time-dependent. The computational advantage of this approach over conventional mapping-based spectral algorithm is more evident for the moving boundary problems [11, 12], because only the entries in the coefficient matrix corresponding to the discretized boundary conditions are required to be computed at each time step while part of the coefficient matrix corresponding to the discretized field equations needs to be constructed only once. The special structure of the coefficient matrices resulting from the algorithm also provides opportunities for devising more efficient iterative solution methods [10-12]. While the IBC method has been successfully employed for various classes of problems, it has limitations in terms of severity of boundary geometry that can be handled accurately. Various tests have shown that if either the wave number of the physical boundary corrugation or the amplitude of this corrugation is too large, the method fails to provide an acceptable accuracy [9-12].

This chapter addresses the limitations of the IBC method discussed above. The IBC method relies on the Galerkin projection for the construction of discretized analog of the field equations. Some of the projection equations are eliminated to provide "space" for the boundary conditions, which are imposed in the Tau-like manner. The boundary conditions are "discretized' using the IBC concept resulting in a number of boundary constraints that is far in excess of that required to formulate a closed system of algebraic equations. In the "classical" formulation of the IBC method [9], only the number of boundary constraints required to form a closed system is retained and boundary constraints corresponding to the lowest (dominant) Fourier modes are used for this purpose. Use of additional available constraints could lead to an increase in the accuracy of the IBC method and could extend its applicability to more extreme geometries, but leads to an over-determined formulation of the problem. Since we have chosen to work with the over-determined formulation, we can also explore whether the use of all available projection equations offers any computational advantage.

The possible gains associated with the over-determined formulation of the IBC method could be problem dependent. In order to provide a definite answer, we have tested this formulation on three model problems involving most commonly found operators, i.e., the Laplace operator, the biharmonic operator and the Navier-Stokes equations. In each case, we have used the same class of geometries for testing purposes so that the reader can identify issues associated with the progressively more complicated operators. Section 4.2 discusses model geometry. Section 4.3 provides description of the method for the Laplace equation. Section 4.4 is devoted to the solution of a model problem that leads to a biharmonic operator. Section 4.5 provides discussion of the solution of the Navier-Stokes equations. Section 4.6 provides a short summary of the main conclusions. In order to provide reliable testing of the accuracy of the over-determined formulation, we have determined reference solutions by solving all three model problems using the mapping method that leads to the classical treatment of boundary conditions. A brief outline of the relevant algorithms is given in Appendices E, F, G for the Laplace, biharmonic and Navier-Stokes problems, respectively.

4.2. Model geometry

We select model geometry in the form of a two-dimensional slot extending to ±∞ in the x-direction and periodic with the wavelength $\lambda=2\pi/\alpha$ (see Fig.1). The slot is bounded by walls whose geometry is expressed in terms of Fourier expansions in the form

$$y_L(x) = -1 + \sum_{n=-N_A}^{n=+N_A} H_L^{(n)} e^{in\alpha x}\,, \qquad y_U(x) = 1 + \sum_{n=-N_A}^{n=+N_A} H_U^{(n)} e^{in\alpha x}\,, \qquad (4.2.1a,b)$$

where $H_L^{(n)} = \left(H_L^{(-n)}\right)^*$, $H_U^{(n)} = \left(H_U^{(-n)}\right)^*$ and the asterisk denotes complex conjugate. Such geometries are of interest in simulations of various physical phenomena where surface roughness plays important role, e.g., electrical micro-capacitors, micro-heat exchangers, laminar-turbulent transition, electrostatic filters, etc. We have selected three types of field equations that the reader might encounter in such applications, i.e., the Laplace equation (discussed in Section 4.3), the biharmonic equation (discussed in Section 4.4) and the Navier-Stokes equations (discussed in Section 4.5). These equations are linear second-order, linear fourth-order and nonlinear fourth-order, respectively, and thus provide ample opportunity for illustration of the performance of the algorithm.

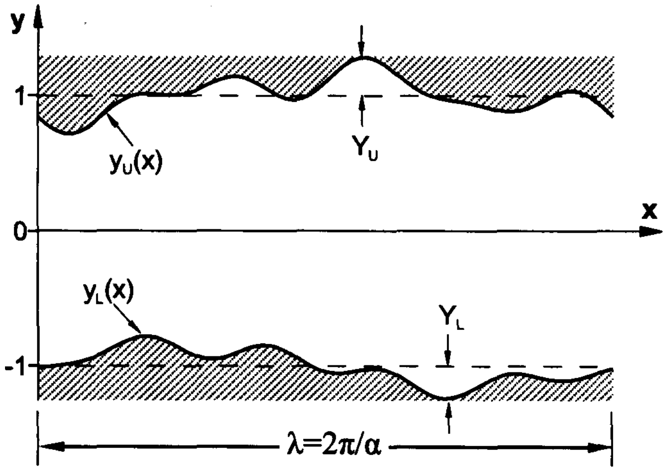

Figure 4.1. Sketch of the domain of interest in the physical plane.

4.3. Problems described by the Laplace equation

The Laplace equation governs different types of practical flow problems, e.g. conductive heat flow, ground-water hydrology, potential flow, etc. In our case we shall consider the

Laplace equation to be describing the conductive heat flow in a corrugated slot whose geometry has been defined in Section 4.2.

4.3.1. Problem formulation

The dimensionless field equation describing heat flow at steady state has the form

$$\nabla^2\theta = 0, \tag{4.3.1}$$

where $\nabla^2 = \partial_{xx} + \partial_{yy}$ is the Laplacian and the symbol ∂ denotes partial differentiation with subscripts x and y denoting the arguments of partial differentiations. Equation (4.3.1) needs to be supplemented by suitable boundary conditions. For convenience we select isothermal boundary conditions on both walls in the form

$$\theta(x, y_L(x)) = C_L = \text{const}, \qquad \theta(x, y_U(x)) = C_U = \text{const}, \tag{4.3.2a,b}$$

and the remaining boundary conditions follow from the assumption of periodicity of geometry. We shall now briefly describe the discretization process. The irregular wall geometry poses the main difficulty in solving problem (4.3.1)-(4.3.2). In order to determine solution with spectral accuracy, we use Fourier and Chebyshev expansions in the x- and y-directions, respectively. The physical domain is confined between ($1+Y_U$) and ($-1-Y_L$) which denote locations of extremities of the domain of interest (see Fig. 4.1). The first step in the solution process involves a mapping from the physical (x,y) coordinates to the computational $(x, \hat{y})$ coordinates in the form

$$\hat{y} = 2[y-(1+Y_U)]/[1+Y_U-(-1-Y_L)]+1, \tag{4.3.3}$$

which limits computational domain to $\hat{y} \in \langle -1,1 \rangle$ and permits the use of the standard definition of Chebyshev polynomials. The governing equation in the transformed coordinates takes the form

$$\partial_{xx}\theta + \Gamma^2 \partial_{\hat{y}\hat{y}}\theta = 0\,, \tag{4.3.4}$$

where $\Gamma = 2/(2 + Y_U + Y_L)$. The boundaries in the $(x, \hat{y})$ plane become

$$\hat{y}_L(x) = \sum_{n=-N_A}^{n=+N_A} A_L^{(n)} e^{in\alpha x}\,, \qquad \hat{y}_U(x) = \sum_{n=-N_A}^{n=+N_A} A_U^{(n)} e^{in\alpha x}\,, \tag{4.3.5a,b}$$

where $A_L^{(0)} = 1 + \Gamma\left[-2 - Y_U + H_L^{(0)}\right]$, $A_L^{(n)} = \Gamma H_L^{(n)}$ for $n \neq 0$, $A_U^{(0)} = 1 + \Gamma\left[-Y_U + H_U^{(0)}\right]$, $A_U^{(n)} = \Gamma H_U^{(n)}$ for $n \neq 0$. The corresponding boundary conditions are

$$\theta(x, \hat{y}_L(x)) = C_L\,, \qquad \theta(x, \hat{y}_U(x)) = C_U\,. \tag{4.3.6}$$

The solution can be represented in the form of Fourier expansion

$$\theta(x, \hat{y}) = \sum_{n=-\infty}^{n=+\infty} \Theta^{(n)}(\hat{y}) e^{in\alpha x} \approx \sum_{n=-N_M}^{n=+N_M} \Theta^{(n)}(\hat{y}) e^{in\alpha x}\,, \tag{4.3.7a}$$

where $\Theta^{(n)}(\hat{y}) = \left(\Theta^{(-n)}(\hat{y})\right)^*$ and $\Theta^{(n)}$ satisfies the modal equations in the form

$$\Gamma^2 D^2 \Theta^{(n)} - n^2 \alpha^2 \Theta^{(n)} = 0 \tag{4.3.7b}$$

where $D^2 = d^2/d\hat{y}^2$, n=0,….,N_M. A minimum of two boundary conditions have to be extracted from (4.3.6) for each equation of type (4.3.7b) resulting in a total 2*(N_M+1) conditions required to close the system. These conditions take an explicit form for each modal equation in the case of smooth boundaries but all modes become coupled in the case of irregular geometry as will be shown later.

The unknown modal functions $\Theta^{(n)}(\hat{y})$ can be represented in terms of expansions based on Chebyshev polynomials in the form

$$\Theta^{(n)}(\hat{y}) = \sum_{k=0}^{k=\infty} Z_k^{(n)} T_k(\hat{y}) \approx \sideset{}{'}\sum_{k=0}^{k=N_T} Z_k^{(n)} T_k(\hat{y}) \tag{4.3.8}$$

where T_k denotes the Chebyshev polynomial of k^{th} order and $Z_k^{(n)}$ are the unknown expansion coefficients. Substituting (4.3.8) into Eq.(4.3.7b) and applying the Galerkin projection technique, i.e., multiplying both sides of the resulting equations by $T_j(\hat{y})$ and integrating with the weight function $\hat{\omega} = 1/\sqrt{1-\hat{y}^2}$, we obtain

$$\sideset{}{'}\sum_{k=0}^{k=N_T} \left[\left\langle T_j, D^2 T_k \right\rangle - \left(n^2\alpha^2\right)\left\langle T_j, T_k \right\rangle\right] Z_k^{(n)} = 0 , \qquad j = 0,\ldots,N_T . \tag{4.3.9}$$

The inner products in Eq.(4.3.9) are defined as $\left\langle f_j(\hat{y}), g_k(\hat{y}) \right\rangle = \int_{-1}^{1} f_j(\hat{y}) g_k(\hat{y}) \hat{\omega}(\hat{y}) d\hat{y}$ and are evaluated using the well known orthogonality properties of Chebyshev polynomials. The reader may note that one can construct a maximum of $(N_T+1)*(N_M+1)$ equations of the type (4.3.9).

4.3.2. Enforcement of boundary conditions

The boundary conditions are to be enforced along the lines $\hat{y}_L(x)$ and $\hat{y}_U(x)$ while the solution domain remains fixed at $\hat{y} \in \langle -1,1 \rangle$. A computationally suitable form of boundary conditions will be constructed using the concept of Immersed Boundary Conditions (IBC). We start with explaining the process of evaluating the unknown temperature $\theta_l(x) \equiv \theta(x,f(x))$ along an arbitrary line, l:={(x,y): y=f(x)}, such that f is a periodic function with period $\lambda=2\pi/\alpha$ and $|f(x)|\leq 1$ which can be expressed as

$$f(x) = \sum_{n=-N_A}^{n=+N_A} P^{(n)} e^{in\alpha x} . \tag{4.3.10}$$

where all $P^{(n)}$'s are known. $\theta_f(x)$ is periodic with the same period λ and thus can be expressed in terms of Fourier series as

$$\theta_f(x) \equiv \theta(x, f(x)) = \sum_{n=-N_\theta}^{n=+N_\theta} \varphi^{(n)} e^{in\alpha x} \tag{4.3.11}$$

where the value of N_θ will be established later. Expressions for the expansion coefficients $\varphi^{(n)}$ can be determined by inserting the discretized form of solution into (4.3.11) resulting in

$$\theta_f(x) = \sum_{n=-N_M}^{n=+N_M} \Theta^{(n)}(f(x)) e^{in\alpha x} = \sum_{n=-N_M}^{n=+N_M} \sum_{k=0}^{k=N_T} Z_k^{(n)} T_k(f(x)) e^{in\alpha x} . \tag{4.3.12}$$

Since $T_k(f(x))$ is periodic in x, it can be expressed in terms of Fourier expansion as follows

$$T_k(f(x)) = \sum_{m=-N_S}^{m=N_S} w_k^{(m)} e^{im\alpha x} \tag{4.3.13}$$

where $\max(N_S)=N_T*N_A$. The expansion coefficients in (4.3.13) can be evaluated with the help of the recurrence relation for Chebyshev polynomials resulting in

$w_0^{(0)}=1$, $w_0^{(m)}=0$ for $|m| \geq 1$, $w_1^{(m)}=P^{(m)}$ for $|m| \geq 0$, and $w_{k+1}^{(m)} = 2\sum_{n=-\infty}^{\infty} P^{(n)} w_k^{(m-n)} - w_{k-1}^{(m)}$.

Substitution of (4.3.13) into (4.3.12) gives

$$\theta_f(x) = \sum_{n=-N_M}^{n=+N_M} \sum_{k=0}^{k=N_T} \sum_{m=-N_S}^{m=+N_S} Z_k^{(n)} w_k^{(m)} e^{i(n+m)\alpha x} = \sum_{h=-N_\theta}^{h=+N_\theta} \sum_{n=-N_M}^{n=+N_M} \sum_{k=0}^{k=N_T} Z_k^{(n)} w_k^{(h-n)} e^{ih\alpha x} \tag{4.3.14}$$